MANUFACTURE OF METAMATERIALS USING LASER PROCESSING TECHNIQUES

Aos Al-Waidh

A thesis submitted in partial fulfilment of the requirements of Liverpool John Moores University for the degree of Doctor of Philosophy

December 2015

Abstract

Metamaterials have raised a considerable interest in the scientific community because of their highly unusual electromagnetic properties and because of their potential for applications that will be beneficial to society. The essential property of this material is the possibility of exploiting negative refraction behaviour which requires both a negative permittivity and a negative permeability.

Metamaterials are periodic or quasi-periodic, sub-wavelength conductive structures. The electro-magnetic material properties are derived from its structure rather than inheriting them directly from its material composition. This term is particularly used when the resulting material has properties that are not found in naturally formed substances as indicated by the prefix "meta".

The aim of the research is to fabricate metamaterials active in the microwave frequency 3-9 GHz. The smallest conductive structures comprising this metamaterial have a size in the millimetre range (3-9 mm). Laser processing techniques are an ideal candidate for the fabrication of this size of metallic structures.

A new method is proven for directly micromachining standard rigid PCB without the need for any chemical or masks to be constructed to create the required patterns. The number of processing steps and hence time is reduced compared to conventional PCB processing with 35μm copper tracks achieved. The process is proven with an Infra-Red fibre laser with nanosecond pulse width.

A novel technique used in processing a flexible PCB without the need of photo-sensitive resin and eliminating the use of masks. A Q-switched DPSS UV laser was employed to write the designed pattern on to the flexible PCB followed by chemical etching.

At the time of writhing up this thesis, there was no evidence that these technique explored in industry or research.

The possibility to machine part of a 3D left-handed (LHM) metamaterial had been demonstrated for the first time with the electromagnetic properties are similar to the original bulk.

Left-handed properties for both bulk metamaterial and machined wedges had been validated by measuring the refraction angle and employing Snell's law to prove the negativity of index of refraction. The index of refraction found to be -1.1 for slab shaped metamaterial, -1.36 for constructed wedge shape and -1.24 for the engineered wedge.

There are just handful of papers that claim to demonstrate metamaterials behaviour at microwave frequency. It was intended that the research conducted during this PhD project would lead to the availability of more examples by understanding how laser technology can be used to manufacture them.

Researchers have developed theoretical techniques to achieve metamaterials active at higher frequencies ultimately aiming to reach the domain of optical metamaterials. However, only limited research has been conducted into fabrication techniques, and few attempts to employ this new material for real applications. This project aims to redress this by examining laser processing as a fabrication technique for microwave metamaterials.

A replica to the Pendry / Shurig microwave cloak has been constructed and tested with a vector network analyser. Transmission with and without the cloak is compared that proves feasibility and repeatability of laser manufacture for this type of cloak.

Keywords

Laser micromachining, PCB Processing, Metamaterials, Left-Handed Metamaterial (LHM), Split Ring Resonator, Negative Permittivity, Negative Permeability, Double Negative Metamaterial (DNG), Negative Refraction, Left-handed metamaterial, Negative refraction

Co-Authorship

Some of the results in Chapter 2 have been published in "Optics and Lasers in Engineering" Journal published by Elsevier. Other figures and diagrams are created by the author unless otherwise cited.

Acknowledgments

Once I have reached this part, I perceive great indebtedness to colleagues, family and friends who have contributed in one way or another to ensure the success and accomplishment of this work. I can only express my deepest appreciation and gratefulness to each and every one of them.

To begin with, I would like to express my gratitude to PIE group; Dr Martin Sharp, Dr Paul French and my lab colleague George Goh. I feel really lucky to have worked with such a great team who turned to be great memorable friends.

A special thanks to all GERI staff and students, it was the most restful and enjoyable years of my life. It is only fair to say that this work is part of each and every one of you

I deeply appreciate the support from Prof David Burton and Dr Francis Lilley for the guidance and support over these years…Thank you very, very much.

My sincere thanks also go to Helen Pottle for her exceptional management and sorting out orders and paperwork proficiently.

I would like to express my sincere thanks again to my supervisor Dr Martin Sharp who gave me the opportunity to join this group and introduce me into the exciting area of left-handed materials. I appreciate your consistent support on my research; without you, this work would have not been the same. Also thanks for your kindness and great characteristics that influence my whole life.

A quote from my laboratory friend, George, In Chinese saying, "Every successful man has a dedicated woman behind him". Well I believe this saying exists in all nationalities, unless someone has the courage to say otherwise! To me it was more than one; my wife, three daughters, two sisters and a mother.

To Samira my wife, and our daughters, Dena, Ronza and Leah, thank you for your patience and love. Without your selfless support, I wouldn't be able to accomplish this work. Finally, I would like to dedicate this thesis to my daughters.

Contents

List of publications

1. Alwaidh A., Sharp M., & French P. (2014). Laser processing of rigid and flexible PCBs. Optics and Lasers in Engineering, 58, 109-113.
2. Adraider Y., Hodgson S., Sharp M., Zhang Z., Nabhani F., Al-Waidh A., & Pang Y. (2012). Structure characterisation and mechanical properties of crystalline alumina coatings on stainless steel fabricated via sol–gel technology and fibre laser processing. Journal of the European Ceramic Society, 32(16), 4229-4240.
3. Adraider Y., Pang Y., Nabhani F., Hodgson, S., Sharp, M., & Al-Waidh A. (2013). Deposition of alumina coatings on stainless steel by a combined laser/sol–gel technique. *Materials Letters*, *91*, 88-91.
4. Adraider Y., Pang Y., Nabhani F., Hodgson, S., Sharp, M., & Al-Waidh A. (2013) Fabrication of titania coatings on stainless steel via laser-induced deposition of colloidal titanium oxide from sol-gel suspension. *Materials Chemistry and Physics*, *138*(1), 245-252.
5. Adraider Y., Pang, Y., Nabhani F., Hodgson S., Sharp M., & Al-Waidh A. (2013). Fabrication of zirconium oxide coatings on stainless steel by a combined laser/sol–gel technique. *Ceramics International*, *39*(8), 9665-9670.
6. Adraider Y., Pang, Y., Nabhani F., Hodgson S., Sharp M., & Al-Waidh A. (2014). Photocatalytic activity of titania coatings synthesised by a combined laser/sol–gel technique. *Materials Research Bulletin*, *54*, 54-60.
7. Adraider Y., Pang, Y., Nabhani F., Hodgson S., Sharp M., & Al-Waidh A. (2014). Laser-induced deposition of alumina ceramic coating on stainless steel from dry thin films for surface modification. *Ceramics International*, *40*(4), 6151-6156.
8. Similar and Dissimilar Joints of Aluminium and Copper by Pulsed Laser Welding (submitted).

Conference paper

1. Aos AlWaidh, Ian Baker, Nick Hay and Young Key Kwon, High Throughput Cutting And Drilling Of Carbon Fibre Reinforced Polymer With Nanosecond Pulsed Solid State Lasers, P180, ICALEO 2014.
2. Manufacture of Metamaterials using laser technology, GARS 2010,ISSN:1757-6717.
3. Laser processing of fixed and flexible PCB boards to construct microwave metamaterials GARS 2012.

Note: the sol gel papers are from collaborative research with Teesside University. Our part was laser processing the variety of sol gel, while they were supplying these materials and analysing the experimental outcome.

It was intended at the beginning of this research to employ sol gel transparent conductive tracks to construct metamaterial but there wasn't enough evidence to proceed in to this route.

List of Figures

List of Tables

List of symbols

E	Dielectric permittivity
M	Magnetic permeability or absorption coefficient
L	Attenuation length
I	Light intensity

A	Absorptivity
R	Material reflectivity
N	Refractive index
K	Extinction coefficient
M^2	Laser beam quality
W	Focussed laser spot radius confining 86.5% (1-e2) of the distributed intensity.
F	Lens focal length
λ	Laser wavelength
R	Laser beam radius at the lens (scanner entrance aperture)
δ	Thermal penetration depth or ablation depth
α	Thermal diffusivity of the material
τ	Laser pulse duration or the thermal relaxation time
P_p	Peak power
E	Laser pulse energy or photon energy
P_{av}	Average power
υ	Laser pulse frequency (repetition rate)
H	Planck's constant
C	Speed of light
F	Laser fluence
W	Watt
S11	Scattering parameter/ reflection
S21	Scattering parameter/ transmission
(t)	Split cut width
(d)	Gap between rings
(w)	Ring width

(r)	Radius of the inner ring
A	Area of the capacitor plate
C	Capacitance
L	Inductance and
f	Frequency
E	Electric field
H	Magnetic field
(a)	Unit cell dimension / lattice spacing
K	Wave propagation direction
S	Poynting vector
ω	Resonance frequency
ω_p	Plasma frequency
F	Filling factor
Z	Impedance
ℓ	Outer length of rectangular SRR

List of abbreviations

LHM	Left-handed metamaterials
PCB	Printed circuit board
DPSS	Diode-pumped solid-state laser
SRR	Split Ring Resonator
CST	Computer Simulation Technology
SEM	Scanning electron microscopy

EM	Electromagnetic
Nd:YAG	Neodymium-doped yttrium aluminium garnet
Cu:Vap	Copper Vapour Lasers
THG	Third harmonic generation
UV	Ultra violet
IR	Infrared
BPP	Beam parameter product
CW	Continuous wave
HAZ	Heat Affected Zone
FR4	Glass fibre reinforced epoxy laminate
PTFE	Poly tetra fluoro ethylene
CNC	Computer Numerical Control
DXF	Drawing Exchange Format
SCAPS	Scanner application software
EDX	Energy-dispersive X-ray spectroscopy
VNA	Vector network analyser
FIT	Finite integration technique
LC	Inductor-capacitor circuit
DNG	Double Negative Materials
DPS	Double-Positive medium
ENG	Epsilon-negative
MNG	Mu-Negative Medium
SNG	Single negative materials
μ_{eff}	Effective permeability
ε_{eff}	Effective permittivity

RTP	Reflective projection technology
TEM	Transverse electromagnetic modes: neither electric nor magnetic field in the direction of propagation
TE	Transverse electric modes: no electric field in the direction of propagation. only a magnetic field exist along the direction of propagation
TM	Transverse magnetic modes: no magnetic field in the direction of propagation. Only an electric field exist along the direction of propagation.
STL	STereoLithography file format
FDM	Fused Deposition Modelling
ABS	Acrylonitrile butadiene styrene
LJMU	Liverpool John Moores University

Chapter One

Introduction

Introduction

This chapter gives a brief introduction to the research field of metamaterials and their fundamental properties. The potential use of laser processing techniques employed in metallic structuring for metamaterials fabrication will also be discussed. This will illustrate the motivation argument behind this research project, along with a brief history to recent theoretical and experimental work performed in the metamaterial research field. An overview of the project's research contribution to the field, in the particular area of manufacturing microwave frequency metamaterials will be presented.

1.1 Background

Electromagnetic metamaterials are manmade periodic sub-wavelength composite metallic structures constructed to obtain special electromagnetic properties unattainable with material found in nature [1]. For this reason the prefix Meta is used before material, which means beyond nature in Greek. The properties of this artificial new class of material mainly depend on the physical geometry of its composite components. In comparison, the classic composite material, like alloys, can be altered by changing the chemical structure properties. The resultant new alloy properties would depends on the chemical components properties and their percentage in the composite.

Generally, metamaterials are active in a very narrow frequency band and act as normal material outside of this band [1]. Metamaterial component structures are smaller than their operational electromagnetic wavelength with minimum structure dimension equal to at most one tenth of the relevant wavelength [Appendix 3.1]. A simplified design of a basic metamaterial unit cell structure is demonstrated in Appendix 3.1 to investigate the relationship between this unit cell size and the operational wavelength. This research focused on microwave frequencies of around 3.5 GHz for unit cells employed on bulk

metamaterial and around 8.5 GHz used on cloaking experiment. The corresponding wavelengths for these frequencies are 85 mm and 35 mm respectively. The expected unit cell for the bulk metamaterial is around 8.5 mm while unit cells for the cloak would be around 3.5 mm.

The periodic structures forming the metamaterial act as artificial atoms that interact with the electromagnetic wave leading to exceptional properties such as a negative index of refraction.

Maxwell's equations are the obvious route to study and investigate electromagnetic wave propagation and scattering. Electromagnetic waves consist of electric and magnetic fields that interact with the surrounding media and propagate according to Maxwell's equations.

Based on Maxwell's equations, a homogeneous medium is described by a certain set of constitutive macroscopic electromagnetic parameters. Therefore the response of such a medium to an electromagnetic wave is determined by their dielectric permittivity (ε) and magnetic permeability (μ). This solution is only valid for a homogeneous medium comprising of particles, or structures, much smaller than the wavelength of interest [2].

The aim of the research is to fabricate metamaterials active in the microwave frequency region that corresponds to centimetre wavelengths. Therefore the smallest conductive structures comprising this metamaterial have a size in the millimetre range. Laser processing techniques are an ideal candidate for the fabrication of this size of metallic structures.

The potential for a double negative nature of metamaterials was originally investigated by Veselago, way back in 1968 [3]. He put forth the theory that electromagnetic waves can follow the left hand rule in a medium that exhibits negative permittivity (ε) and

permeability (μ) simultaneously. Under these conditions, the direction of the Poynting vector of a monochromatic wave passing through such a system exhibited a direction opposite to the wave vector (phase velocity). In other words, the phase velocity of this EM wave would be opposite to that of the energy flow. For this reason the wave is said to have a backward propagation He suggested that in such materials the magnetic field (*H*), the electric filed (*E*) and the wave vector (*K*) form a left handed set of vectors. In this case, the so called right-hand rule is substituted with a left-handed rule and the medium is termed to be a Left Handed Metamaterial (LHM). In this context, as both permeability (μ) and permittivity (ε) are negative, such media are often referred to as Double Negative Materials (DNG). Other terminology for these materials can be found in Appendix 4.1.

Experimental investigations of laser effects on materials began to appear soon after the advent of the first ruby laser in 1960. The very first lasers developed were too weak and too unstable for any industrial use. The field of lasers and photonics has expanded rapidly such that modern lasers are capable of processing a wide range of applications for a variety of materials with remarkable precision. As higher powers, better beam qualities and an expanded number of wavelengths have become available; more applications are being invented and brought into practical use [4].

Laser material processing has achieved a high level of development and acceptance for many applications such as cutting, drilling, marking, welding, engraving, forming and other forms of material surface treatment in a wide range of industries including automotive, aerospace, microelectronics and medical industries among others.

A dominant factor for a successful laser application is the material absorptivity to the wavelength of the laser light. Fundamentally, a suitable absorption in the material is

required to create localised heating of the material surface. At short wavelengths (e.g. ultraviolet wavelengths) the laser light can interact by directly breaking molecular bonds. The mechanism can be different for ultrafast lasers with short pulses (measured in pico- and femto- seconds) where the wavelength dependence of absorption can be overcome by multiple photon non-linear absorption.

1.2 Motivation

The proposed metamaterial structures in this research are around 3 mm width and minimum metallic track size of 200 μm. This size of metamaterial unit cell is expected to operate in the microwave region of electromagnetic spectrum.

The first attempts at fabricating structures that leads to what is today called "metamaterials" occurred in the early 21st century [5]. Such new metamaterials were active at the microwave frequencies for ease of test and fabrication. From this beginning, researchers have tried to develop their techniques to achieve metamaterials active at higher frequencies ultimately aiming to reach the domain optical metamaterials. This race led to a rapid theoretical development of metamaterial science but with limited research into fabrication techniques, and few attempts to employ this new material for real applications. This project aims to redress this by examining laser processing as a fabrication technique for microwave metamaterials, allowing engineers to explore the practical applications of these new materials and for metamaterials to become available to integrate into a wide range of industrial possibilities.

This motivation to investigate metamaterials active in microwave frequency is timely in that there are a large number of applications that depends on microwave signals. Microwaves now play a key role in our daily life since they are essential for many applications including communications and sensing. The current trend in these areas is

towards minimising the size of electronic devices size to meet the growing demand for more compact designs. While the development in semiconductor and PCB manufacturing facilitates reduced compact electronics sizes, the handling of microwave signals, antennae and wireless device still needs significant improvement. In the past two decades, academia and industry have put enormous effort into reducing the size of microwave antennae and micro-strip waveguides [6]. However, it remains a matter of concern as micro-strip size reduction has reached its limits.

Microwave metamaterials are the next approach to improve microwave devices and reduce their spatial dimensions. So called double negative, or left-handed, metamaterials (LHM) (Chapter 4) are a class of metamaterials that exhibit both negative permittivity and permeability. This type of metamaterial has a negative index of refraction that leads to a broad range of potential applications such as perfect lenses and cloaking devices to name a few. While these headline applications are now often reported, there appears to be insufficient investigation of metamaterials application in antenna systems.

The objective of this research can be summarised as follows:

- Develop laser processing of flexible and rigid PCB.
- Use laser processing to manufacture split ring resonator (SRR) on rigid PCB.
- Manufacturing left handed metamaterial (LHM) from the manufactured SRR.
- Use laser processing of flexible PCB to manufacture a microwave cloak and demonstrate its cloaking behaviour.

1.3 History

Most current literature on metamaterials refers to the late 60´s publication by Veselago introducing the first theoretical speculation of metamaterials concept. In his paper he

termed a media in which both permittivity and permeability are negative as a Left-Handed material (LHM) [3]. The "*left*" term arises as the component of electromagnetic wave set of vectors; the electric and magnetic fields and the wave vector form a Left-Handed set of vectors instead of the conventional Right-Hand set. Veselago, for the first time, indicated that this wave vector can point towards the opposite direction of the Poynting vector, which determines the direction in which energy travels [3].

This concept leads to a number of exceptional media properties such as negative-index refraction and the reversal of the following phenomena: Cherenkov radiation, Doppler shift, and also of Snell's law. This leads to potential applications such as invisibility cloaking devices and perfect lenses [7].

Figure (1.1): Roman Lycurgus cup made of ruby glass and nano scale gold particles, green opaque (left) in dark room and transparent red under light [9].

However it can be argued that metamaterials have a very long history, indeed back to 4th century AD (Late Roman). The evident for this is the Lycurgus Cup held in the British Museum. It is made of Ruby glass injected with gold particles of about 60 nm size [8].

It was not recognised as metamaterials but related to myth as the name indicated. The cup has a damped green colour under low lighting and turns to transparent shiny red when enough light passes through it (Figure 1.1).

The nano-scale gold particles act as metamaterial, creating an optical resonance frequency that allows transmission at this red wavelength, changing the cup's appearance from opaque to transparent [8].

The negative phase velocity concept and its important outcomes have been demonstrated by Sir Arthur Schuster in 1904 [10]. In 1944 the negative refraction of media with opposite phase and group velocities is discussed in a paper by Mandel'shtam [11].

Other interesting work on metamaterial technology prior to the term coming into use is the work on waveguide metallic structuring for microwave lenses in 1948 [12].

In a 1957 publication, Dimitriy, theoretically proves that the direction of the phase velocity is opposite to that of flux energy in a left-handed metamaterial but again it is still not called a metamaterial [13].

Returning to named metamaterials research, D.R.Smith's group at the University of California fabricated the first left-handed metamaterial in May 2000 [5]. This was after Pendry's group at Imperial College, London, successfully modelled a left-handed metamaterial active at a microwave frequency [1]. Together these works proved both theoretically and experimentally the concept of left-handed media with negative electric permittivity and negative magnetic permeability simultaneously [1, 5].

This work was created a firm interest in the metamaterials field that is growing year on year as evidenced by an increasing number of academic publications, leading to the introduction of a new journal called Metamaterials from the publishers Elsevier in 2007.

Most recently an EPSRC Centre for Doctoral Training in Metamaterials has been established at the University of Exeter to start in September 2014.

Pendry's modelling is based on a fabrication of two interleaved structures that comprise a left-handed metamaterial: Split Ring Resonators (SRR) that induce negative permeability and thin wire structures that give rise to negative permittivity. These SRRs and thin wires are aligned periodically to attain the double negative properties of left-handed metamaterials (LHM) [1].

The dream of optical metamaterials cannot be achieved with the conventional methods proposed by Pendry, because of the high losses associated with the copper structures that comprise the metamaterials [14]. This disadvantage increases proportionally with frequency particularly at optical frequencies as metallic conductivity is reduced. The feasibility of producing optical metamaterials is too low with this metallic model for most applications [15].

With the advances in nanotechnology and the exceptional capability to control nano-structuring, last year, a tuneable optical metamaterial has been achieved with nickel nano-rod arrays [16]. Also some of apparent restrictions in metamaterials, such as high losses, have been overcome with dielectric alumina [17].

1.4 Contribution from this research project

There are just handful of papers that claim to demonstrate metamaterials behaviour at microwave frequency. It was intended that the research conducted during this PhD project would lead to the availability of more examples by understanding how laser technology can be used to manufacture them.

1 Rigid PCB laser processing: A new method is proposed and proven for directly micromachining standard rigid PCB without the need for any chemical or masks to be constructed to create the required patterns. This method provides high control and accuracy to ablate the copper cladding area leaving the required tracks. This method could be in hard to reach areas on PCB or even inside-device PCB repairing. The processing time is much less than conventional PCB processing technique with 35µm minimum copper tracks possible. The process is proven with an Infra-Red fibre laser with nanosecond pulse width that is employed for this processing technique.

2 Flexible PCB laser processing: A novel technique used in processing a flexible PCB without the need of photo-sensitive resin and eliminating the use of masks. To the best of the author's knowledge, the technique used in processing the flexible PCB (demonstrated in chapter 2 and Figure 2.23) is unreported in the literature (including patents). This technique is expected to offer a significant contribution to knowledge and industry as it reduces the costs and saves time by reducing the number of processing steps. A Q-switched DPSS YVO_4 laser, frequency tripled to 355nm, was employed to write the designed pattern on to the flexible PCB.

3 Metamaterial design and Construction: The base unit cell of metamaterials used to construct 2D and 3D left-handed media in this project is a Split Ring Resonator (SRR). The design of these SRRs is based on Pendry's model [1]. However, the design is modified for ease of fabrication and calculations; the enhancement of a single SRR is done with CST microwave studio simulation software that can calculate the expected resonance frequency.

4 3D engineered left-handed me amaterials: one of the important outcomes of this research is the possibility to machine part of a 3D left-handed (LHM) metamaterial and to demonstrate, for the first time, that its electromagnetic properties are almost preserved. Usually 3D LHM media are constructed as fabrication of spaced 2D layers that forms a 3D LHM. In this research this gap is filled with dielectric material to make a rigid cube that can be cut, e.g. into two wedges with an electric saw. The resultant wedges have properties similar to the original cube. This demonstrates the potential for an end user to buy a "lump" of metamaterial and cut it or shape it as required.

5 Left-handed property validation: The negative index of refraction has been proven with wedge shaped and slab shaped metamaterials by measuring the refraction angle and employing Snell's law.

6 Cloak fabrication: a replica to the Pendry / Shurig microwave cloak [18] has been constructed and tested with a vector network analyser and with a simplified technique to prove feasibility and repeatability of this type of cloak.

7 Laser processing: The use of lasers as a "rapid prototyping" tool for microwave metamaterial fabrication and associated composite structures are novel.

1.5 Thesis Outline

This thesis is devoted to study the potential of using laser radiation to fabricate metamaterials active in the microwave frequency range, and to confirm their consequent metamaterial behaviour. This research work is described in six chapters as described below.

- Firstly, chapter one (this chapter) gives an introduction starting with a basic background on metamaterials and the potential for laser processing followed by a description of the motivation for this research. A brief history on metamaterial birth and development up to the current date is presented in the history section of this chapter.

  Novelty and contributions to knowledge are the most important part of any research; therefore it has been stated clearly in contributions section in this chapter. This section describes finding novel laser-PCB processing techniques and creating a new class of engineered metamaterial that can be of practical benefit to broad range of industries and researchers.

- Chapter two of this thesis describes the laser material interaction and the development of PCB processing techniques. The importance of laser radiation absorption by materials is described in this chapter and the conditions affecting this absorption are discussed.

  Furthermore, material classification and how does each type of these materials influence the laser wavelength choice is debated. This links to the section on laser source characteristics that covers laser properties such as laser wavelength, laser spot size and laser pulse duration. Laser and materials specifications are important in understanding the subsequent section on laser material removal.

  Laser material removal is expressed in terms of laser ablation and which is described using four parameters: hot ablation, cold ablation, ablation threshold and ablation rate.

  The chapter continues with the laser processing of PCB and its comparison with conventional techniques. Experiments on flexible and rigid PCB are demonstrated in this chapter with details of novelty involved in these techniques. The results achieved in processing both rigid and flexible PCBs together with the scaling down in size of the resultant structures are illustrated.

Finally, the last section of chapter two reports on tests of the physical structure and scanning electron microscopy of the laser machined PCBs. This gives an insight into the novelty of these processes.

- The purpose of chapter three is to understand the fundamental electromagnetic resonance mechanisms of Split Ring Resonators (SRR) and to investigate the relationship of the physical shape of a SRR on its electromagnetic resonance frequency. The single unit cells (SRR) described in this chapter will form the base to build metamaterial blocks presented in chapter four.

  The investigation of the SRRs shape and geometrical dimensions on magnetic resonance frequency include the following parameters; split cut width, gap between rings, ring width, base dielectric permittivity and base thickness.

  The study covers both numerical modelling and actual testing for each of these parameters. CST Microwave Studio® software is employed for the numerical simulations to determine the resonance frequency for each case. These results are used to estimate the resonance frequency for the experimental measurements to narrow the actual measurement time and frequency sweep band. Also, where possible, each numerical simulation is compared to an experimental test.

  Additionally, SRRs with different number of cut sections and the effect of electromagnetic field polarisation on the SRRs electromagnetic resonance are also investigated in this chapter.

- Chapter four proceeds with the outcome of chapter three by taking the design of the single unit cell SRR and structure them on PCB boards using techniques in chapter two. Then the 2D PCBs are used to construct 3D wedges and slab shaped metamaterials. This chapter starts with a detailed introduction on left-handed metamaterials and classification

of materials according to their permeability and permittivity. Within the context of this chapter, the left-handed materials (LHM) term is defined and how to realise them is briefly explained. The main concern in this chapter is to investigate the microwave transmission in these LHM metamaterials to determine their permittivity and permeability, in particular, to identify the negative values allowing metamaterial behaviour to be proven.

The double negativity of permeability and permittivity is also demonstrated in this chapter for both slab and wedge shaped structures employing refraction measurements and Snell's law for verification.

Consequently the proposal of cutting slab shaped LHM metamaterial into a wedge shaped is also addressed and the continued metamaterial behaviour is verified. It is anticipated as identifying and introducing a new class of metamaterials that can open an unprecedented research path.

- The theory of Optical transformation and cloaking are presented in chapter five. This chapter begins with a brief introduction into optical transformations and conformal mapping principles. In addition, other existing alternative to electromagnetic cloaking are discussed in "Transformation Devices" such as camouflage and Stealth technology.

  The core of this chapter presents the fabrication and verification of a replica of Shurig's cloak fabrication [18] and its construction from flexible PCB processed as explained in chapter two of this research. This is followed by experimental demonstrations to verify cloaking in microwave frequency region.

- Lastly, chapter six offers conclusions of this thesis including future work. It summarises the main points of previous chapters to remind the reader of the key outcomes of this research and give some recommendation for potential future works.

Chapter Two

Laser Processing

2.1 Introduction

Laser processing involves the interaction of electromagnetic radiation and materials. Understanding the relation between well-known phenomena such as reflection, refraction, etc. and the radiation properties which cause them requires the knowledge of the physical processes that occurs during the laser-material interaction.

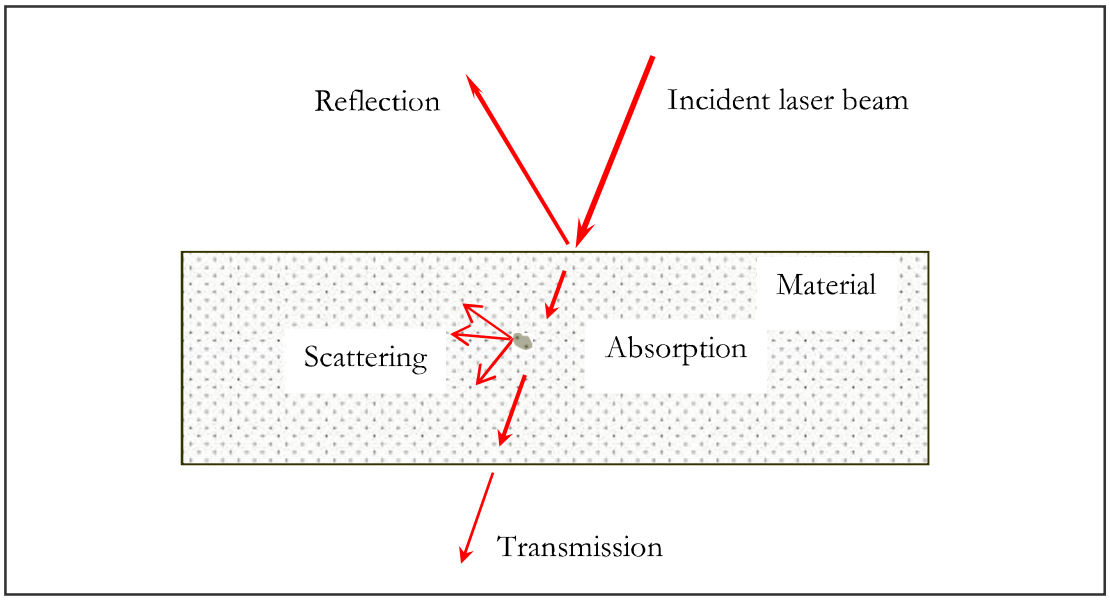

Figure (2.1): Interactions of laser radiation with material.

Although lasers are continuously opening up new opportunities for wide range of optical phenomena, related to both photons and waves, it remains a challenge to map the relations between laser radiation and these phenomena. Such mapping gives comprehension to the capabilities and limitations of laser machining [19, 20].

Various phenomena including reflection, refraction, absorption, scattering, and transmission occurs when the electromagnetic radiation is incident on the surface of a material (Figure 2.1).

Absorption is the most desirable and important phenomenon in the laser processing of materials as it initiates several effects such as heating, melting, vaporization, plasma formation, etc. These effects are the basis of various laser processing techniques which primarily depends on the material properties and the laser parameters [21].

The materials properties include absorptivity, density, thermal conductivity, specific heat, latent heats, etc. and the laser parameters include intensity, wavelength, pulse duration, angle of incidence, polarization, etc. This section briefly explains the important laser–material interactions and their effects that are relevant in the laser machining and fabrication of materials.

2.2 Absorption of Laser Radiation

Laser radiation is formed of monochromatic electromagnetic waves, which are characterised by electric field (E) and magnetic field (H) vectors. Electromagnetic radiation that is absorbed by material interacts only with the outer electrons (either free or bound). Since electric and magnetic fields only interact with charged matter, the influence of atomic nuclei is often neglected [22].

The absorbed laser radiation in the material can be expressed in terms of the Beer-Lambert law as:

$$I(z) = I_0 e^{-\mu z} \text{----------} (2.1)$$

Where (I_0) is the incident intensity, I(z) is the intensity at depth (z), and (μ) is the absorption coefficient. Thus, the intensity of the laser radiation is reduced exponentially inside the material. This means that the laser intensity is significantly reduced at a depth equal to:

$$L = \frac{1}{\mu} \text{----------} (2.2)$$

Where L here is defined as the attenuation length [23].

The absorbed intensity, as can be seen in the above equation, depends on the absorption coefficient and hence the absorptivity of the material is considered as one of the important parameters influencing the effects of laser–material interactions.

The absorptivity *(A)* can be defined as the fraction of incident radiation that is absorbed at normal incidence:

$$A = 1 - R \text{---------} (2.3)$$

Where R is the material reflectivity which can be expressed as:

$$R = \frac{(n-1)^2 + k^2}{(n+1)^2 + k^2} \text{----------} (2.4)$$

Where (n) and (k) are the refractive index and extinction coefficient respectively and both can be determined from the complex refractive index (n_c) as:

$$n_c = n - ik \text{----------} (2.5)$$

These parameters (*n* and *k*) are dependent on the incident wavelength and material temperature. The reflectivity of the material will also depend on these factors and it will also depend on the angle of incidence of the radiation and the material surface roughness [24].

Figure 2.2 below shows the relationship between the reflectivity of some common metallic materials with the wavelength of some common YAG lasers and CO2 laser.

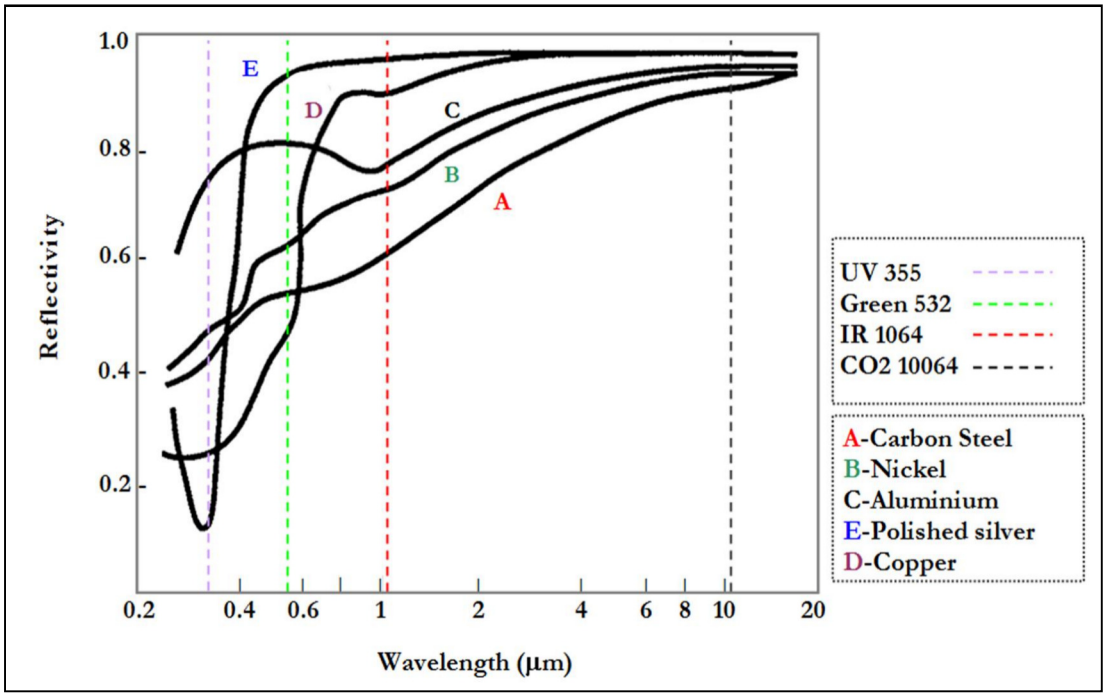

Figure (2.2): Variation of reflectivity with wavelength of two important lasers (Nd:YAG and CO_2) for several metallic materials [24,26].

As can be seen in the figure, the metallic materials are more reflective at longer wavelengths. Thus for a given material, the radiation from the IR YAG laser (wavelength = 1064 nm) is less reflected than the CO2 laser (wavelength = 10.6 µm). However, there are several other factors which may strongly influence the absorptivity such as material temperature (Figure 2.3).

The material temperature rises as energy is transferred from photons to the metal and both the electrons and the lattice atoms gain kinetic energy that influences the collision frequency. Thus as the temperature is significantly elevated, the amount of absorbed radiation may increase which in turn decreases the reflectivity of a material. A material which is strongly reflective at a low temperature may become strongly absorbent at a high temperature [24].

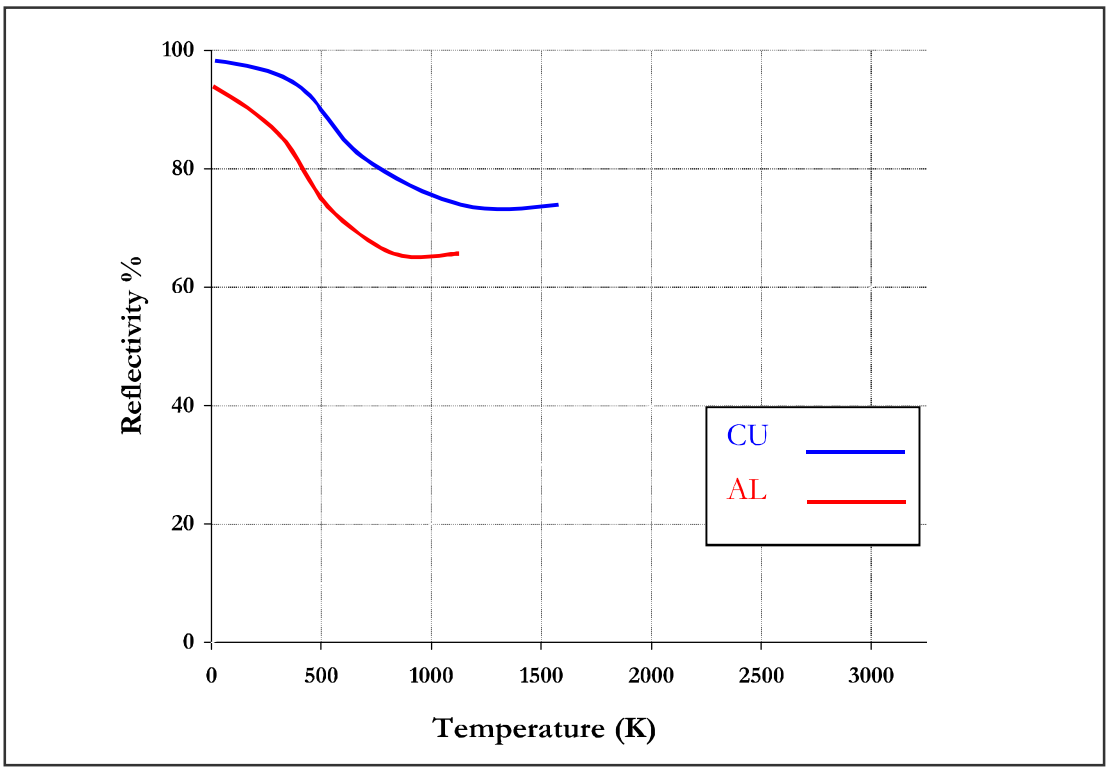

Figure (2.3): Reflectivity versus material temperature of some metallic material when radiated with Nd:YAG [21].

Metals, as mentioned before, are highly reflective at longer wavelengths due to their free electrons. However non-conductors and semi-conductors exhibit complex absorption profiles due to their different intermolecular vibration states which require higher photon energy for bond state energy transitions to happen. Figure 2.4 compares reflectivity of some metals with a non-metal for a range of laser wavelengths ranging from infrared to ultraviolet [24, 25].

The reflection percentage is rather complex for composite material such as alloy brass or steel but in general the primary material in the composite dominates the amount of absorbed radiation. However, regardless of the composition, electromagnetic waves always interact with the electrons inside the metal or alloy.

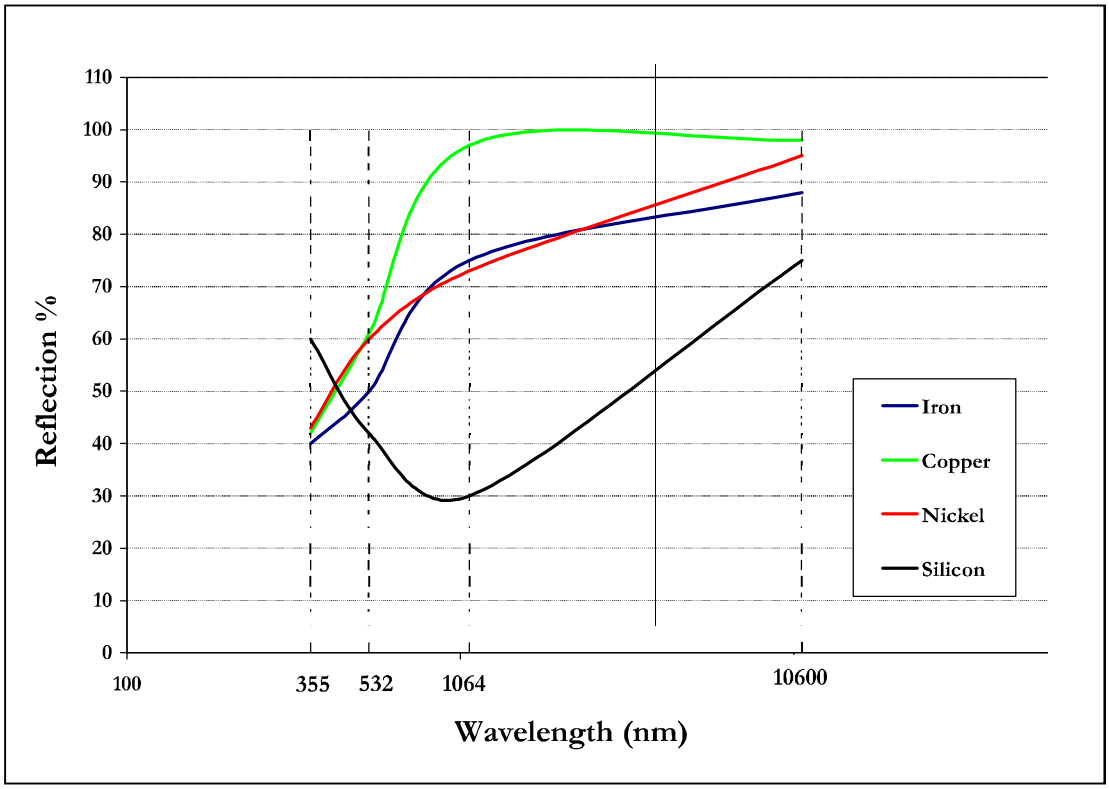

Figure (2.4): Material reflectivity for a range of laser wavelengths [24].

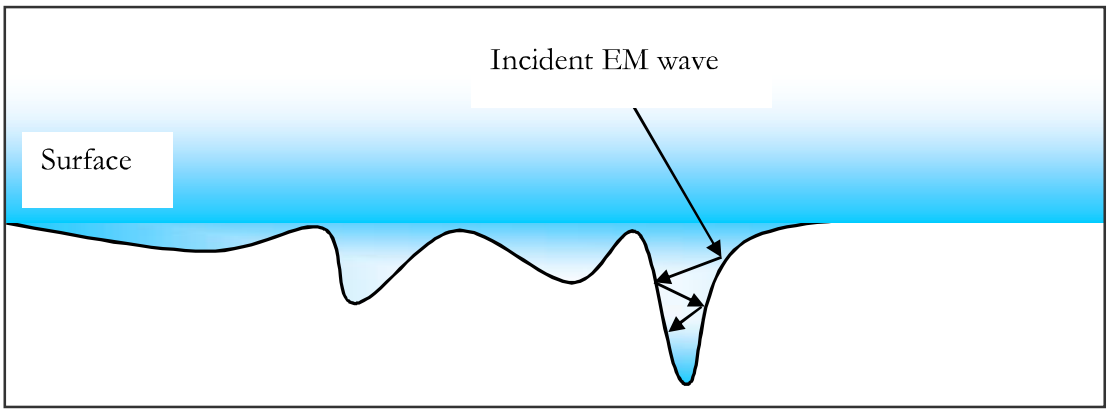

Figure (2.5): Electromagnetic wave trapped by the surface.

Reflection is also dependent upon the material surface properties. Most surfaces are considered imperfectly flat and have certain degrees of roughness or texture to them, which will influence their electromagnetic behaviour. The electromagnetic waves may, for instance, be trapped by the surface texture leading to multi-reflections inside the texture enhancing the absorption as illustrated in Figure-2.5.

2.3 Material classification

Materials can be categorised into four groups: metals, ceramics, polymers, and composite materials. The physical property and tolerance of the processed material (product) is the primary factor of a manufacturing process selection.

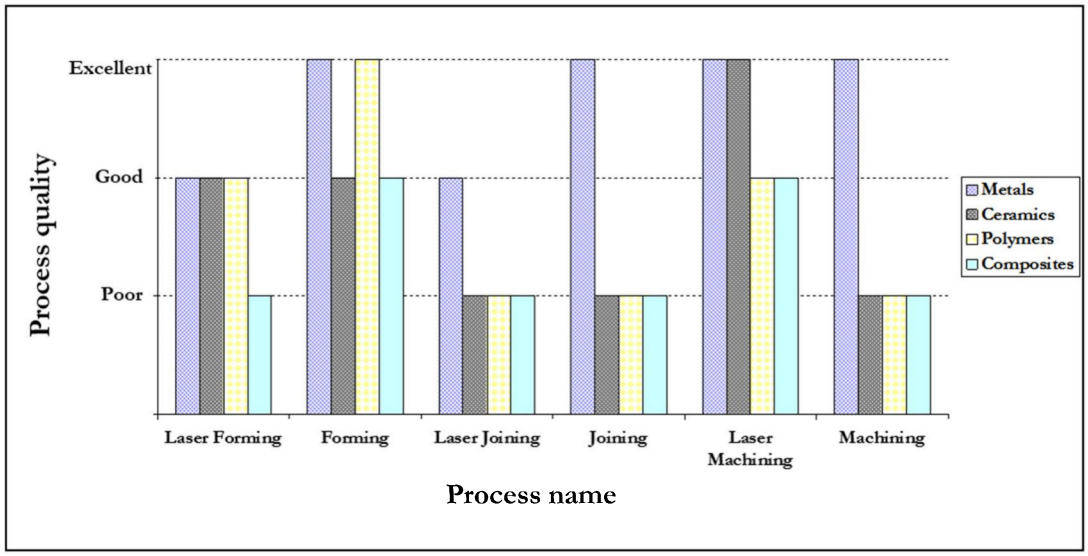

Figure (2.6): Suitability of conventional and laser processes to four types of materials [26].

Individual laser process cannot manufacture different materials types with equal ease and quality [26].

Figure 2.6 shows a comparison between laser and conventional manufacturing processes for the four type's materials. The suitability of laser processing mainly depends on the processed materials properties, such as vaporising temperature, ductility and brittleness; also it depends on the material absorption to the selected laser wavelength.

2.4 Laser Source Characteristics

There are broad ranges of laser sources on the market that are capable of processing various types of materials for versatile applications. Each particular application and corresponding material determines which type of laser and what wavelength of laser is most appropriate. The most important factors in laser selection are wavelength that can range from far infrared to deep ultra violet, pulse duration from continuous wave to femtoseconds, laser beam quality (M^2) and average power. These parameters determine a good laser processing application, though often with trade-offs in parameters selection to be considered.

2.4.1 Laser Wavelength

A wide spectrum of high and low power lasers of different wavelengths are employed for various material processing applications, starting from the common CO_2 laser in the mid-IR region and the Nd:YAG operating in the near IR. Also, Ti:Sapphire lasers can operate in the IR region with femtosecond pulse width, and in this case, the wavelength selection can become less important.

Second harmonic Nd:YAG green lasers (532nm) and Copper Vapour Lasers (Cu:Vap) are examples of lasers that operate in the visible range. Lastly, a broad range of UV wavelength operation can be achieved with Excimer lasers. Whilst fourth harmonic 266 nm and third harmonic generation (THG), also known as frequency tripling 355 nm, Nd:YAG lasers offer deep and near UV wavelengths respectively.

Generally, lasers with shorter wavelengths have less average power available (Table 2.1) with the exception of Excimer lasers that offer relatively high outputs in the UV.

However, excimer lasers are classified as hazardous lasers - they use Halide gases that introduce serious safety and lifetime concerns form corrosive material such as F_2.

Consequently, laser industries are taking steps towards improving fourth and third harmonic generation, converting solid-state lasers wavelengths to the UV or visible range [27]. Also lasers with shorter wavelength are less efficient, for instance, typical efficiency for 4th Harmonic Nd:YAG is 3% compared to up to 30% efficiency for CO_2 lasers [4].

Table (2.1): Typical laser characteristic reported in 1997 [4].

	Laser Name	Wavelength (nm)	Gain Medium	Pulse Duration	Average Power (W)
IR	CO2	10600	Gas	CW and ms	100 - 8000
IR	Nd:YAG	1064	Solid state	CW 0.1-1 ms 5-200 ns	100-4000 200-600 10-450
IR	Ti:Sapphire	780	Solid state	100 fs	2
Visible	Cu:Vap	578 or 511	Metal Vapour	15-60 ns	20-100
Visible	Frequency double Nd:YAG	532	Solid State	5-100 ns	3-90
UV	Frequency triple Nd:YAG	355	Solid State	<50 ns	2-7
UV	XeCl (Excimer)	308	Gas	15-30 ns	200
UV	4th Harmonic Nd:YAG	266	Solid State	<25 ns	2
UV	KrF (Excimer)	248	Gas	15-30 ns	180
UV	F2 (Excimer)	157	Gas	15-30 ns	20

Therefore it is clear that lasers with longer wavelengths are more efficient with higher power. However, for many applications shorter wavelength operation is a requirement to achieve the required process results.

Enormous effort has been made towards increasing the output laser average power especially with solid state YAG lasers. An example of current DPSS laser average powers is given by the current Powerlase Photonics Ltd. product line summarised in table 2.2 below.

Table (2.2): Current reported typical laser characteristic [27].

	Laser Name	Wavelength (nm)	Gain Medium	Pulse Duration	Average Power (W)
IR	Nd:YAG	1064	Solid state	10 ps 30-60 ns	100-200 400-1500
V	Frequency double Nd:YAG	532	Solid State	75-90 ns	150-350
UV	Frequency triple Nd:YAG	355	Solid State	<50 ns	40-80

2.4.2 Laser spot Size

The laser spot size is one of the important laser parameters that determine the minimum feature size that can be machined. Therefore the laser spot size needs to be small enough compared to the desired feature size.

The main interest of this project is the micromachining of Split Ring Resonators on fixed and flexible PCB boards. Therefore a TEM00 (Gaussian) mode beam is considered in this discussion. The Gaussian beam case that is the desired ideal beam emerging from a laser cavity and it forms the basis to understand other more complex modes of laser

beam shape. These modes are the result of the geometry of the laser gain medium, and other factors, such as changes in the index of refraction of the laser rod for Nd:YAG lasers. This is accompanied by a higher M^2 value, which is lower beam quality. Figure 2.7 below illustrates the variation of intensity according to the Gaussian beam shape with intensity (I) and cross sectional radius (r).

The cross section of the Gaussian beam has the same form as that of the well-known statistical distribution function of the same name.

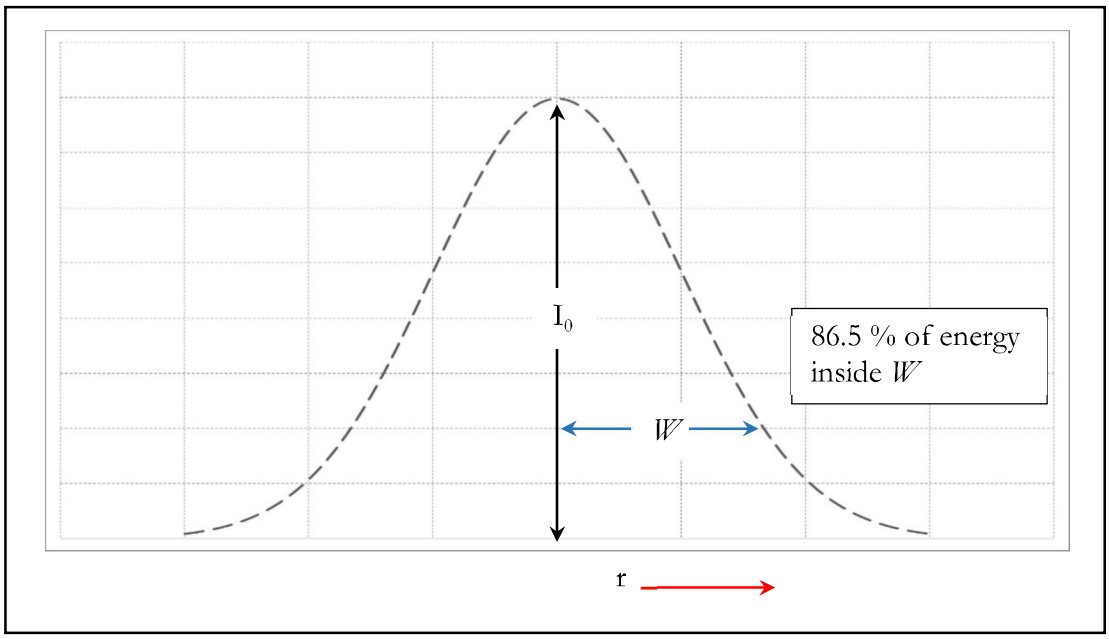

Figure (2.7): Radial intensity distribution of Gaussian beam.

The beam radius *(W)*, in this case, is defined by the area containing most of the distributed beam power. Therefore 86.5% (1-e^2) of the total power is contained within this radius.

Theoretically, the smallest beam radius or spot size *(W)* for a focussed Gaussian laser beam can be calculated from the widely reported equation 2.6 below [21].

$$W = M^2 \frac{\lambda f}{\pi r} \text{----------} (2.6)$$

Where W is the focussed spot radius, M^2 is the beam quality, f is the lens focal length, λ is the laser wavelength and r is the radius of laser beam at the lens (scanner entrance aperture).

M^2 is the beam quality that is equal to one for ideal case of a Gaussian beam and it is greater than 1 for all real laser beams. The M^2 factor can also be related to two parameters conveniently associated with the laser beam, the angle of beam divergence and minimum beam waist size that also reflect the quality of the real beam in question. These two parts known as the beam parameter product (BPP) that is equal to λ / π for a diffraction-limited Gaussian beam case. Equation 2.6 reveals that smaller possible spot radii are achieved with the larger radius of the beam as it is delivered to the focusing lens, or if the focal length of the focusing lens is smaller. Practically, beam expanders (telescopes) are often used to expand the beam spot size before entering the focusing lens in order to increase (r) and hence reduce (W).

As discussed above, from equation (2.6) the spot size can be reduced when choosing a focusing lens with a short focal length. However this advantage is diminished by the shorter room available between the lens and the focused beam spot (work piece). Therefore, the laser beam encounters more debris, spatter and fumes from the workpiece reducing laser process efficiency and it may also damage the focusing lens. In addition, with a laser focusing lens, usually attached to a beam steering scanner, being close to a workpiece makes introducing an inert gas delivery system or a processing nozzle difficult.

As a result, there is a compromise in the selection of the lens focal length between getting a small spot size and retaining a sufficient working distance.

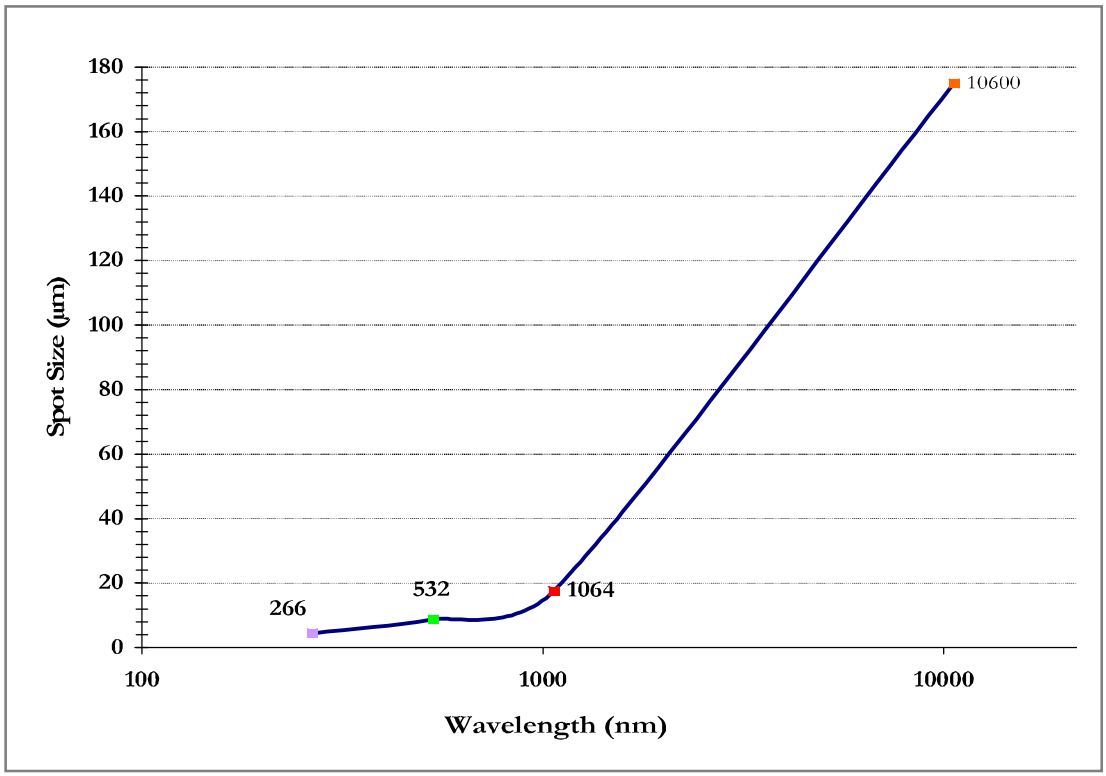

Figure (2.8): Focal spot diameter against wavelength with common laser wavelengths.

Furthermore, equation (2.6) shows that spot size is proportional to the wavelength. Therefore the shorter the wavelength, the smaller possible diameter spot size as illustrated in figure (2.8).

Therefore lasers with short wavelengths such as Excimer lasers (λ= 254 nm or 340 nm) or even Nd:YAG (λ = 1064 nm) can have smaller spot size than carbon dioxide lasers (λ= 10600 nm) and are adequate to process fine structures. However, carbon dioxide lasers usually have high beam quality and low $M^2 \approx 1$ compared to Nd:YAG lasers, therefore this must be taken into account in determining the potential minimum spot size.

The spot size diameters plotted in figure 2.8 above are calculated with equation 2.6 for comparison of some common lasers based on lasers with M^2=1.3 with 10 mm diameter collimated beam at a focusing lens of 100 mm focal length.

2.4.3 Pulse Duration

The laser beam that emerges from the laser is either continuous wave (CW) mode with constant amplitude, or pulsed beam mode. The output laser energy is constant in continuous mode operation while in pulsed mode the energy is stored then rapidly discharged into short pulse duration of high peak power.

Pulse duration or pulse width is defined as the time required for a pulse to transmit its energy. Pulsing can be achieved with several mechanisms such as normal pulsing, mode locking and Q-switching [28]. Pulse duration is an important factor to control the laser–material interaction and to obtain high peak power. Great efforts have been made to move towards shorter pulse durations starting from nanosecond through picosecond and currently the shortest pulse duration is in the femtosecond range. The femtosecond is the SI unit of time equal to 10^{-15} of a second. However, there are trade-offs to be considered when reducing pulse duration; usually it achieved at the expense of average power and laser system complexity. Table (2.1) shows some common industrial lasers available with pulse durations from (0.1 s) to fs (10^{-15} s) and corresponding average power available.

The thermal energy transferred to the workpiece can be lowered by reducing the laser interaction time; which will decrease the Heat Affected Zone (HAZ). Reducing HAZ is very important particularly in processing electronics or heat sensitive components. The relationship governs the pulse duration with respect to thermal penetration can be expressed as following:

$$\tau = \frac{\delta^2}{4\alpha} \text{----------} (2.7)$$

Where δ = thermal penetration depth, α = thermal diffusivity of the material, and τ = pulse duration or the thermal relaxation time [29-30].

From this equation, as pulses duration shorten the thermal penetration depth will reduced by a square factor and hence minimising thermal damage. Meanwhile, the thermal penetration depth can also be related to the incident wavelength as flowing:

$$\delta = \frac{\lambda}{4\pi k} \text{----------} (2.8)$$

Where k = extinction coefficient [31].

Based on the above equation, the thermal penetration depth will decrease with shorter wavelength and hence minimising bulk thermal transfer. In addition as pulse duration shortens the peak power for each pulse will rise according to the following simple equation:

$$P_p = \frac{E}{\tau} \quad or \quad P_p = \frac{P_{av}}{\tau \nu} \text{----------} (2.9)$$

Where: (P_p) is the peak power, (E) is pulse energy, (P_{av}) is the average power, and (υ) is the pulse frequency (repetition rate).

From this equation as pulses duration shorten the peak power will rise and hence improving the vaporisation to melt ratio. In addition as higher peak power induces a more rapid phase change, the thermal damage is reduced (see Figure 2.9).

Equation (2.7) hold true for pulse durations up to 10s of picoseconds [29]. For shorter pulses, where laser intensity is so high, a non-linear material removal mechanism takes place. The high intensity pulses cause material ionisation and free electrons. Further ionisation occurs as these electrons moves within the material leading to plasma formation. This plasma rapidly ejected away from the material surface by ion repulsive force and plasma repercussion pressure. Plasma expulsion reduces the amount of heat inside the material. Therefore as this mechanism much faster (several orders) than thermal conduction, thermal effects or the heat affected zone can be minimised [29, 32].

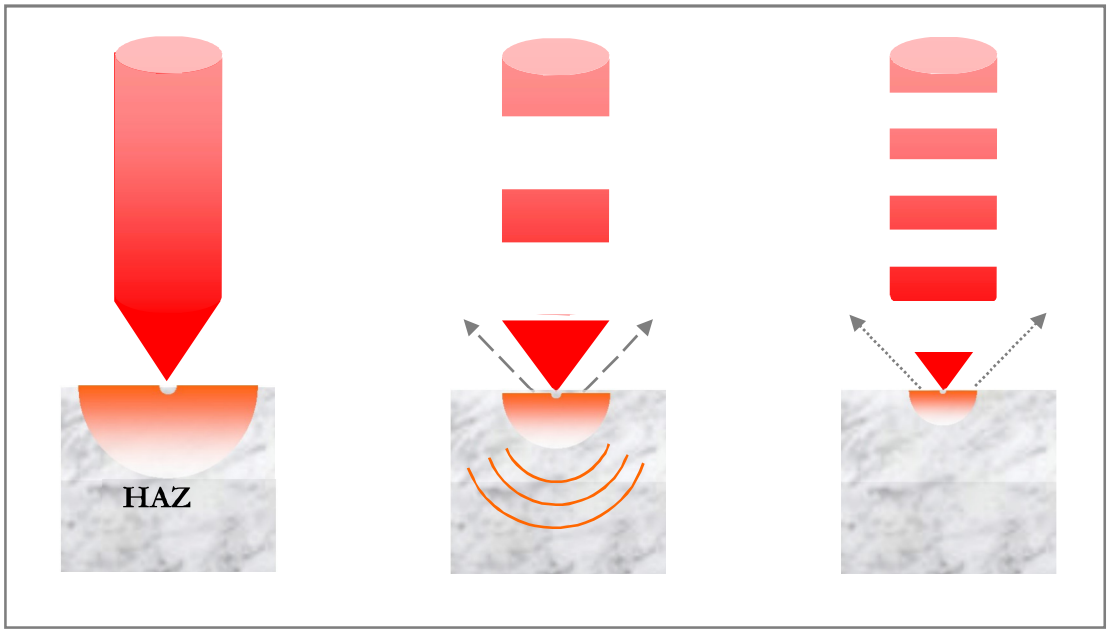

Figure (2.9): Heat-affected zones (HAZ) in material subjected to different lasers with different pulse width.

Femtosecond and even Picosecond laser pulses width generate very local energy that introduce a very small HAZ on the processed material compared to long pulse or continues mode lasers (Figure 2.9). Minimum heat damage and superior quality are often required with high precision electronics or medical manufacturing [33].

2.5 Laser material removal (Laser Ablation)

Several laser types with different processing mechanism can be employed for material removal with micron and submicron precision. This research focused on laser ablation technique that is suitable for micromachining PCBs with acknowledge of other important techniques such as laser-assisted chemical etching and other hybrid processing. This section briefly explains the important aspects of material removal mechanisms that are summarised in figure 2.10 below.

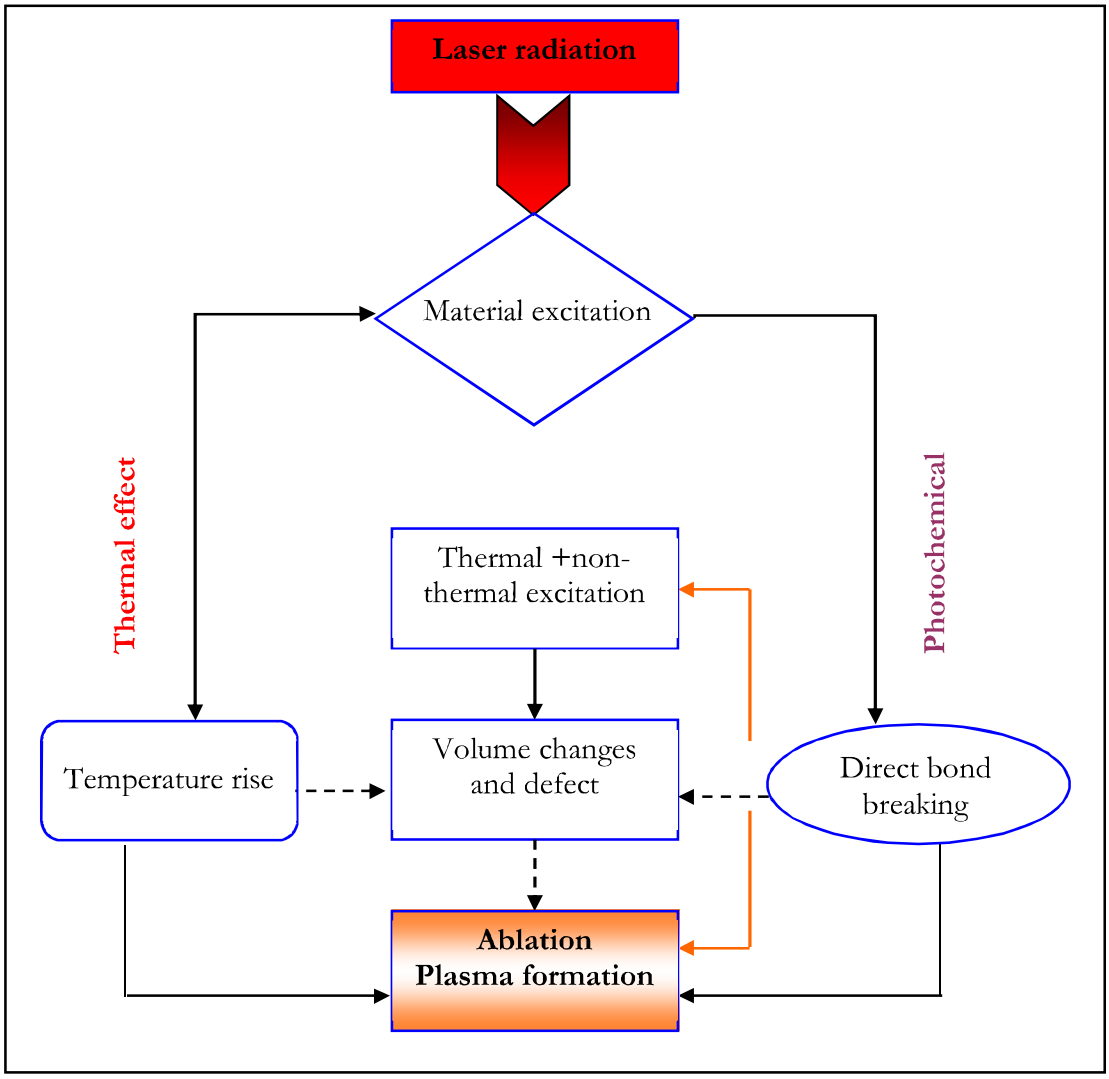

Figure (2.10): Various mechanisms of laser ablation [34].

Laser ablation processes have been broadly categorized into two physical domains namely, Cold Ablation and Hot Ablation. These categories can be distinguished by the corresponding time scales of their activation (Figure 2.9).

Pulsed laser ablation is extensively employed in materials processing including micromachining, marking, grooving, cutting, and drilling. Meanwhile, pulsed laser ablation widely used in medical applications such as ablation of human corneal tissues which obviously required careful and precise removal [30].

In general, material removal processes by photo-thermal or photo-chemical (non-thermal) interactions can be designated as ablation. The mechanism of photo-thermal or hot-ablation is associated with vibrational heating. While photo-chemical can be designated as cold ablation and characterised by material molecular bond breaking.

The laser–material ablation is rather a complex mechanism as different phenomena may take place simultaneously in different spatial regions and time. As a result the whole process often described as photo-physical processes such that thermal and non-thermal processes interfered.

It can be difficult to differentiate the different phenomena to the overall action of the laser radiation. However, the number of physical phenomena that contribute can be limited by controlling the fundamental laser parameters settings: photon energy, laser intensity, pulse duration, and beam radius; Figure (2.10) above shows laser-material interaction with various possible mechanisms of laser ablation [34].

2.5.1 Hot Ablation

Hot ablation is a mechanism of absorbing laser energy that is rapidly converted into intermolecular vibration. This induced kinetic energy translates thermally to heat, bringing the surface of the material to a melting and vaporization state.

The melted liquid and gaseous phases are separated by a thin vapour layer where the material phase is between liquid and vapour. This means, on molecular level, it is difficult to distinguish between the states of matter. Therefore, the liquid and gaseous phases do not reach a common equilibrium state.

Hot ablation is the dominant process in continuous wave and long pulse lasers that induce surface expansion and expulsion (due to thermal stresses) of the desired target material [35]. This often achieved by heating of the target material through the liquid to the vapour phase.

This type of lasers is usually associated with a heat affected zone (HAZ) determined by the rate of energy absorption to the energy loss through thermal conduction in the material [35]. The HAZ is often considered as limiting factor especially when high precision is required or when it may present a hazard, e.g. laser surgery.

Going back to the dissipation of heat during thermal ablation its effect can be understood by looking at the thermal penetration time or relaxation time, τ, (Equation 2.7)

Equation 2.7 reveals that small value of thermal diffusivity generally provides higher ablation efficiency of a material. In addition, when pulse duration is longer than thermal relaxation time, the absorbed energy will be dissipated in the surrounding material by thermal conduction.

Thermal ablation mechanisms are often employed for micromachining metallic material and ceramics, while cold ablation mechanisms are used in processing polymers. However, some of the polymers can also be effectively ablated by hot ablation mechanism. Cold ablation is discussed in next section where large material ablation rates and high efficiency can be achieved with short pulse width lasers.

2.5.2 Cold Ablation

Cold ablation mechanisms are dominated by ultra-short pulse lasers with pulse durations less than 20 picosecond, or by UV laser processing. The peak power introduced by ultra-short pulse lasers is very high with intensities of more than 10^{15} W/cm^2. With this ultra-short pulse duration the energy is delivered before thermal diffusion occurs which resulting minimum thermal damage giving high quality and precision processing outcomes [34].

For UV lasers the energy induced by the incident photon causes direct bond breaking of the molecular chains in the organic materials. The material then removed by molecular shattering without significant thermal damage [19, 34]. The previous statement is simply based on Planck's Equation:

$$E = h\frac{c}{\lambda} \text{----------} (2.10)$$

Where h is Planck's constant, c is the speed of light, λ is the wavelength, and E is the photon energy.

This suggests that to initiate the cold ablation process, the photon energy (equation 2.10) must be greater than the bond energy. For instance, the breaking energies of many molecular bonds (Figure 2.11) is in the range of (3.0–6.4 eV) while the UV laser

produces radiation with wavelengths in the range 193–355 nm which gives photon energies in the range (6.4–3.5 eV). However, this is not the case for visible laser radiation where the output energy is less than the separation energy of molecular bond. Despite this, the cold ablation mechanism often dominates the process with ultrashort pulse lasers. This is related to multi-photon absorption mechanism where the bond breaking is achieved by simultaneous absorption of two or more photons. Thus two photons energies combined together to break the molecular bond [19].

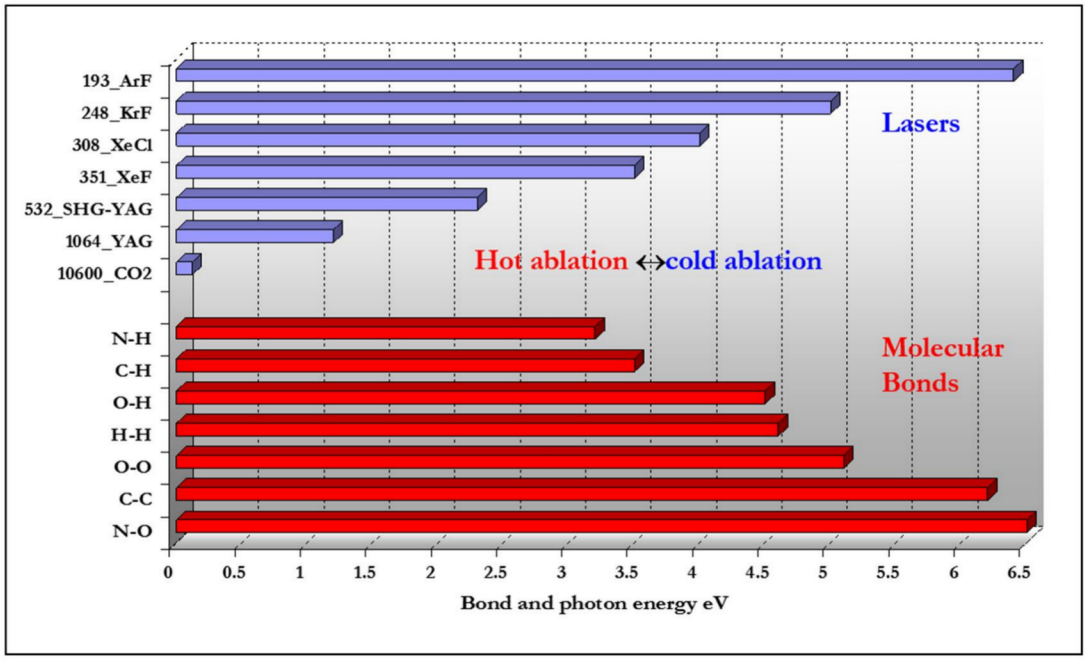

Figure (2.11): Common molecular bonds breaking energies and photon energies of some common lasers [36].

Figure (2.11) illustrates a comparison between various lasers radiation energies and the breaking bonds energies of various molecular bonds. As indicated in the figure, the radiated energies of Excimer and UV lasers exceed the molecular braking energies of many materials bonds resulting in effective cold ablation.

On the other hand, long wavelength lasers (in the IR region) such as Nd:YAG 1064 nm and CO2 10600 nm lasers, the photon energies are significantly less than the bond

breaking energies of these materials [36]. For these lasers, even with the previously mentioned multi-photon mechanism, ablation is often associated with undesirable heat effects of surrounding material [36].

2.6 Ablation Threshold

The Ablation Threshold can be defined as the minimum laser energy for material ablation to take place. Based on "blow-off" model the ablation threshold is the minimum laser energy required to remove the material by ablation

Below the ablation threshold energy the laser-material interaction is characterised by thermal effects [26].

Meanwhile, above the ablation threshold the process can be explained by bond breaking (cold-ablation) [34].

According to this theoretical model, the ablation rate curve can be determined giving that the material is immediately removed by ablation [37]. When the laser fluence exceeds a critical energy (threshold energy), the estimation of the ablation rate and threshold can be expressed as:

$$\delta = \frac{1}{\mu_a} \ln\left(\frac{E_0}{E_{th}}\right) \text{---------} (2.11)$$

Where: E_0 = incident laser energy, E_{th} threshold energy, δ = ablation depth, and μ_a= absorption coefficient.

2.7 Ablation Rate

The precise control of material removal is often of practical importance, therefore ablation rates need to be understood. The ablation rates primarily depend on the laser fluence, pulse duration, number of pulses, and pulse repetition rates. Typically, ablation behaviour for fluences above the ablation threshold can be presented in the following Figure (2.12).

The ablation starts above the minimum fluence F_{th} (ablation threshold) after which the ablation rate significantly increases up to the saturation fluence Fs. For influence above Fs, the process efficiency is reduced due to ionisation and plasma formation. Furthermore, in this saturation region, the incident radiation tends to alter the material absorption coefficient, thus the actual ablation depth deviates from the "blow-off" model assumption [37].

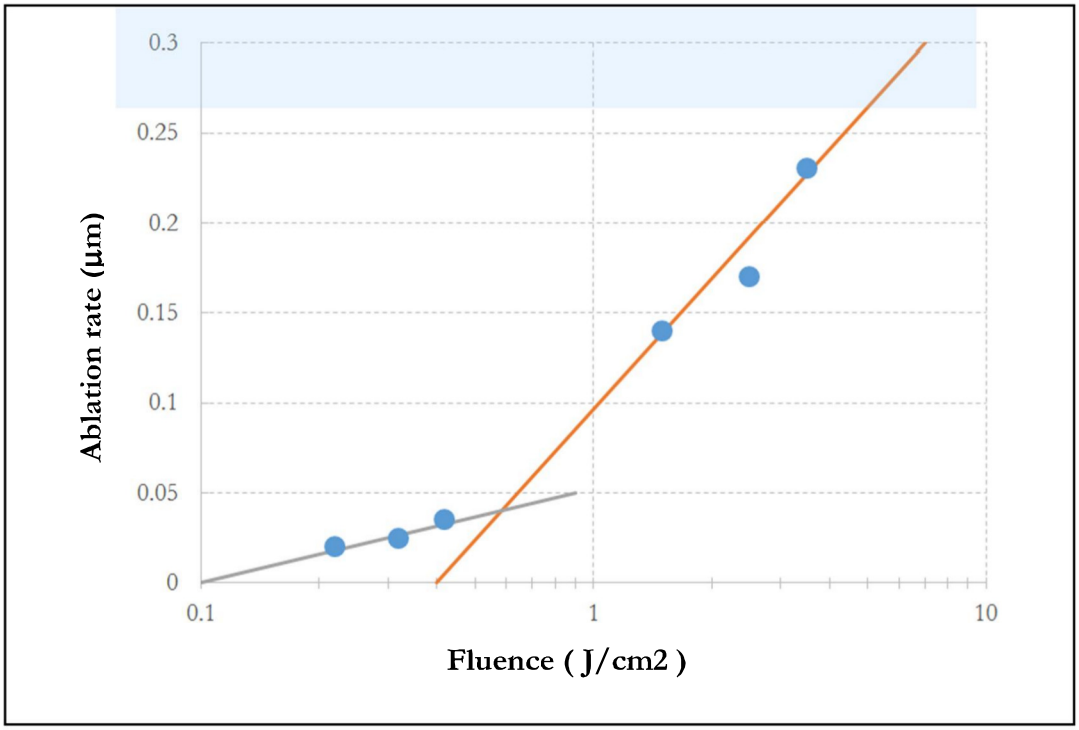

Figure (2.12): Silver ablation rate vs. laser fluence showing two regimes [26]

At the intermediate fluence F_m, the most efficient process is achieved and the maximum rate in a pure vaporisation system is equal to the penetration depth δ.

Ablation threshold is determined from the relationship between ablation rate and laser fluence. Ablation rate can be defined as ablation depth δ per pulse and the ablation rate (L) for the two regimes (Figure 2.12) can be described by the logarithmic laws based on a two-temperature model [38]:

$$L = \delta \ln\left(\frac{F_0}{F_{th}}\right) \qquad \text{For low laser fluence} \qquad (2.12)$$

And

$$L = \alpha \ln\left(\frac{F_0}{F_{th}}\right) \qquad \text{For high laser fluence} \qquad (2.13)$$

Where: α = thermal diffusion length, δ = the penetration depth, F_{th} = ablation threshold.

The two-temperature model describes two regimes namely high and low fluence radiation: at higher laser fluence, the ablation rate is dominated by the thermal diffusion length while at lower laser fluence the process can be characterized by the absorption depth.

2.8 Laser Micromachining Techniques

As explained in the previous section, ablation is the primary mechanisms of material removal for precision micromachining of materials. Another important aspect of micromachining is the generation of shape. As the material is ablated it is necessary to create the 2D shape that will form the final object. This can be performed in various

manners. In this project the shape is generated as a Vector Motion of the tightly focussed laser beam across the surface.

The laser vector motion technique is widely used for many micromachining applications as it offers significant advantages such as simple and inexpensive optics, and ease of interfacing with CAD files. Early micromachining was performed with Excimer lasers and a mask projection technique. The advent of DPSS and fibre lasers focussed to a single point necessitated the development of the vector motion technique.

The laser vector motion technique is characterised by a number of parameters namely: the spot size; the working distance of the focussing optic; and the depth of focus. The smaller the spot size the smaller the feature size that can be created. The spot size can be reduced, for instance, by choosing focussing optics (F-Theta lens) with a shorter focal length.

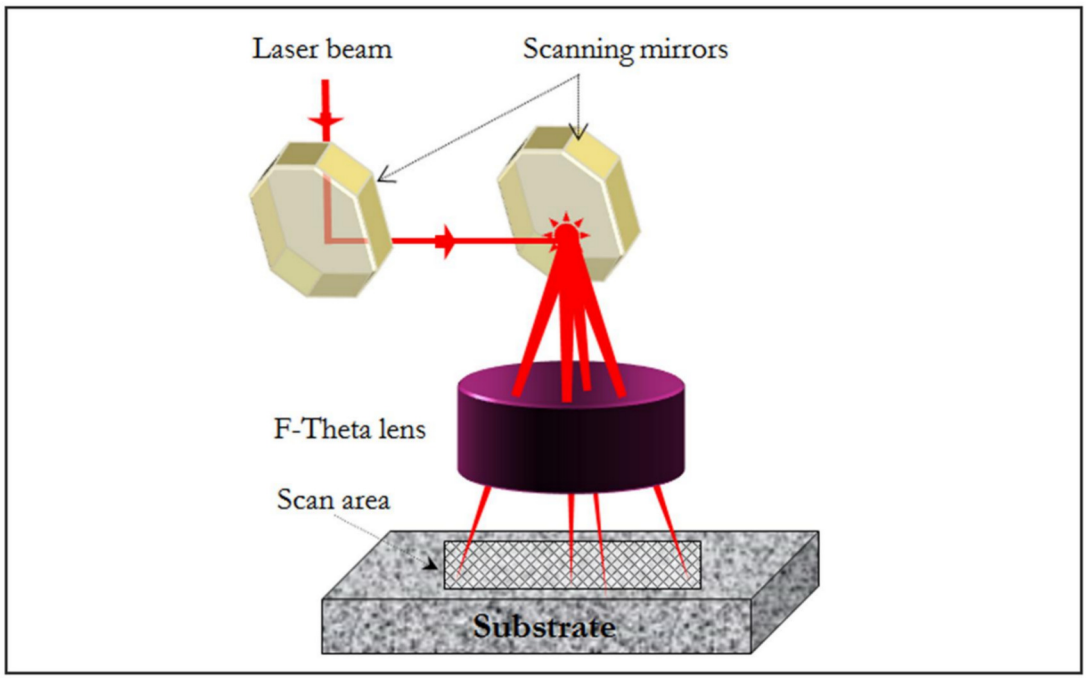

Figure (2.13): Laser direct writing with scanning mirrors.

In the laser vector motion technique, micromachining of the desired pattern is performed by focusing the laser beam on the object surface. The beam is then scanned over the substrate to create the required pattern.

Galvanometer-controlled scanning mirrors (Figure 2.13) can be employed to direct the laser beam to the required positions and are programmed with the integrated software. A flat-field lens (F-Theta lens) is used as a focusing lens with the scanning mirrors to maintain the focal conditions at various angles of beam deflection [39].

Another approach for micromachining with a vector motion is by moving the substrate with respect to the fixed laser beam. This is achieved using programmable positioning stages (Figure 2.14).

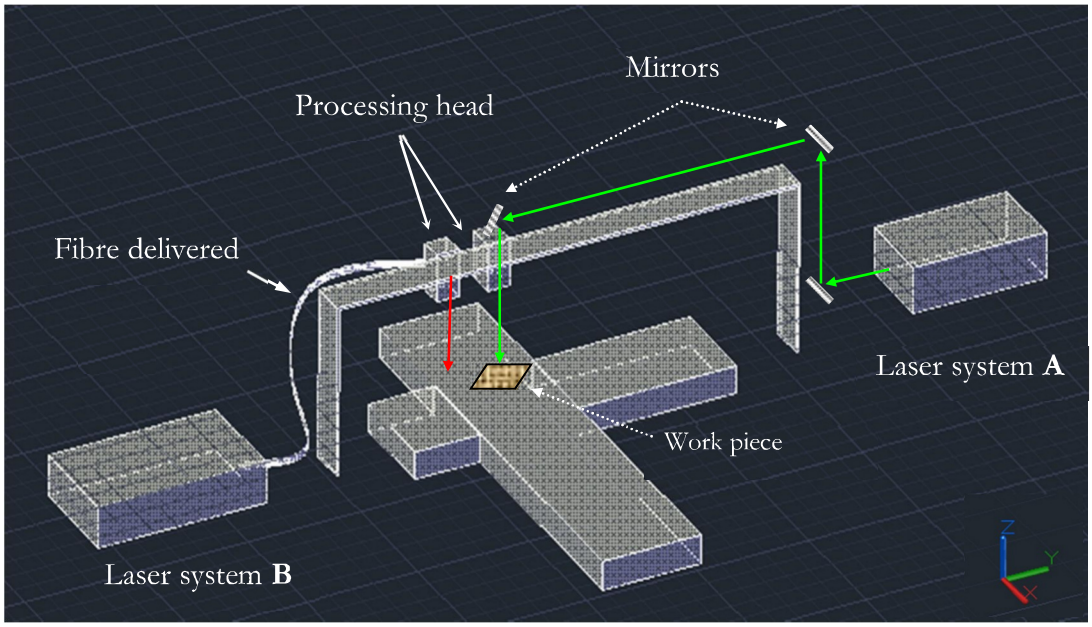

Figure (2.14): Laser beam delivery, (A) Free-space and (B) Fibre optic.

Laser beam delivery is carried out either by fixed mirror systems (Figure 2.14 A) or by optical fibres (Figure 2.14 B). Fixed mirrors are often used to preserve beam quality or to handle higher powers than fibres. Fibre delivery is used to provide flexibility and to reduce the system size to allow higher acceleration.

2.9 Printed Circuit Board (PCB) processing

Currently PCBs are manufactured with metals such as copper, silver or gold as a conducting layer on a dielectric substrate or base layer such as FR4 (glass fibre reinforced epoxy laminate), PTFE (Teflon®) or another dielectric. An outer photoresist layer is present for photolithographic processing. Each of these three layers can have many different physical and mechanical properties depending on the materials used for the selected manufacturing techniques.

A mask-based lithography technique, followed by chemical etching, is commonly employed throughout the electronics industry for flexible and rigid PCB manufacturing to create the desired conductive tracks [40]. This technique may suffer from unwanted shapes or uneven tracks in the generated PCBs caused by any defects in the mask or any gap between the substrate and the mask. Therefore, current PCB production manufacturing is aiming to develop a maskless technique for possible higher resolution, higher throughput and lower cost [41].

Lasers with high beam quality (low M^2) can be employed in the PCB's manufacture by directly writing the desired tracks on the rigid PCBs. They can also be used to write patterns on to the photoresist layer followed by chemical etching to prevent mask usage [40]. Pulsed laser micromachining is extensively used to ablate metallic materials in many applications including marking, engraving, cutting, and drilling [42].

2.9.1 Conventional PCB processing

A traditional PCB consists of a conducting pattern manufactured by selectively removing the copper (or other conductor) from the board to leave the necessary conductive tracks and areas. The desired tracks or pattern are replicated in a "photomask" that is attached

firmly on top of the photoresist layer of the PCB board. This mask is illuminated with a UV light that projects the mask image on to the photoresist top layer. Poor quality or thinner tracks can occur if there is a gap between the mask and the substrate, this leading to UV light illuminating unwanted parts of the photoresist.

The positive photoresist that is exposed to the UV light becomes soluble to an alkaline developer such as sodium hydroxide or metasilicate, and is washed away. This step is followed by the chemical etching process with chloride based solutions such as iron chloride, cupric chloride or alkaline ammonia to etch away the undesired copper material and leave the conducting tracks. The PCB is finished with cleaning step with isopropanol to remove any unwanted remaining photoresist on top of the copper tracks.

Another way to engineer conductive track on PCB boards is to employ mechanical router designed for this purpose. The process done by milling the copper layer, leaving the required tracks. In general CNC machines accuracy could be in microns but as it is a contact technique it will depend on the machined parts (copper). The minimum recommended tracks width for this technique is 0.75 mm. Also the vibration from the process may affect other nearby tracks, separation of the copper layer or create tracks with rough edges [45].

2.9.2 Laser processing of Printed Circuit Boards

Laser micromachining has been investigated extensively in the last decade, however only a few reports can be found in the literature that describe lasers being used to create copper tracks of less than 100 μm width in the PCB fabrication process.

At the time this research was performed there were no clear evidence of employing laser processing techniques for micro machining copper tracks on standard PCB or the method used to process flexible PCB described in 2.10.2 and reference 40.

In contrast to many conventional PCB structuring techniques, the laser processing approach may generate much higher resolution patterns without any special laboratory conditions and toxic chemicals.

2.10 Performed Experiments

The following sections report on two processing experiments. These experiments were performed to create conducting tracks on standard rigid, and flexible, PCB substrates. The first experiment's aim is to laser micromachine a rigid PCB with a 20W average power nanosecond pulsed fibre laser. The laser emits infrared radiation at a wavelength of 1064nm and can be operated in continuous wave (CW) mode, or pulsed mode. The generated pulse frequency can range from 1 to 500 kHz with corresponding pulse widths of 9 to 200 ns. The second experiment is performed to process the flexible PCB with pulsed UV (wavelength 355nm) Diode Pumped Solid State (DPSS) Nd: YAG laser. The maximum average power is 2W at a pulse repetition frequency of 20 KHz and pulse width 18ns.

2.10.1 Laser Micromachining of Rigid PCB

This set of experiments was conducted to develop direct removal of the copper cladding from a standard one-sided PCB with a pulsed fibre laser. The one sided standard PCB board consists of a FR4 dielectric base layer and 35µm conducting copper layer.

The aim of the experiment is to measure the material removal rate of the copper layer on standard PCB board and to find the optimum laser parameter for this process.

The experimental outcome will be used to develop parameters to machine the desired open ring resonator (SRR) and other shapes on this standard PCB boards.

The laser beam from a SPI Lasers model G3 SP-20P-HS fibre laser is delivered to a 5x beam expander before entering GSI Lightning galvanometer scanning head.

The laser beam enters the scanner head through a 10 mm diameter aperture. The beam is then focused to nominal spot size of 23μm at the focal point with a 100 mm focal length f-theta lens (manufactured by Linos) (Figure 2.15 and 2.16). Details of the verification of the spot size can be found in appendix 2.2.

To confirm the positioning of the focal point of the system, a heat sensitive film was used that has about a 2W threshold. This means that the film remains unchanged for laser powers less than 2W.

The working stage is then moved close to the expected focal point (F-theta data sheet) then lowered down gradually in 0.1 mm steps in Z direction.

The laser is scanned over a 10 mm^2 square filled with a 30 μm hatch to mark the film at each step to visualise the intensity of the marked area.

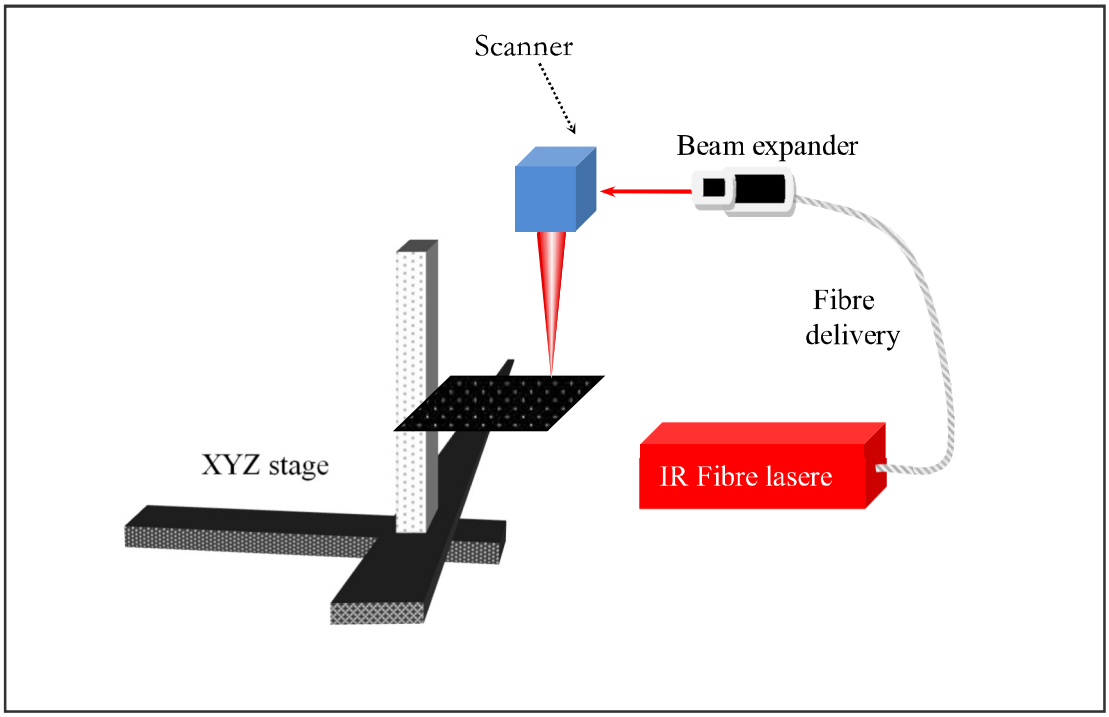

Figure (2.15): Schematic drawing of the IR fiber delivered experiment.

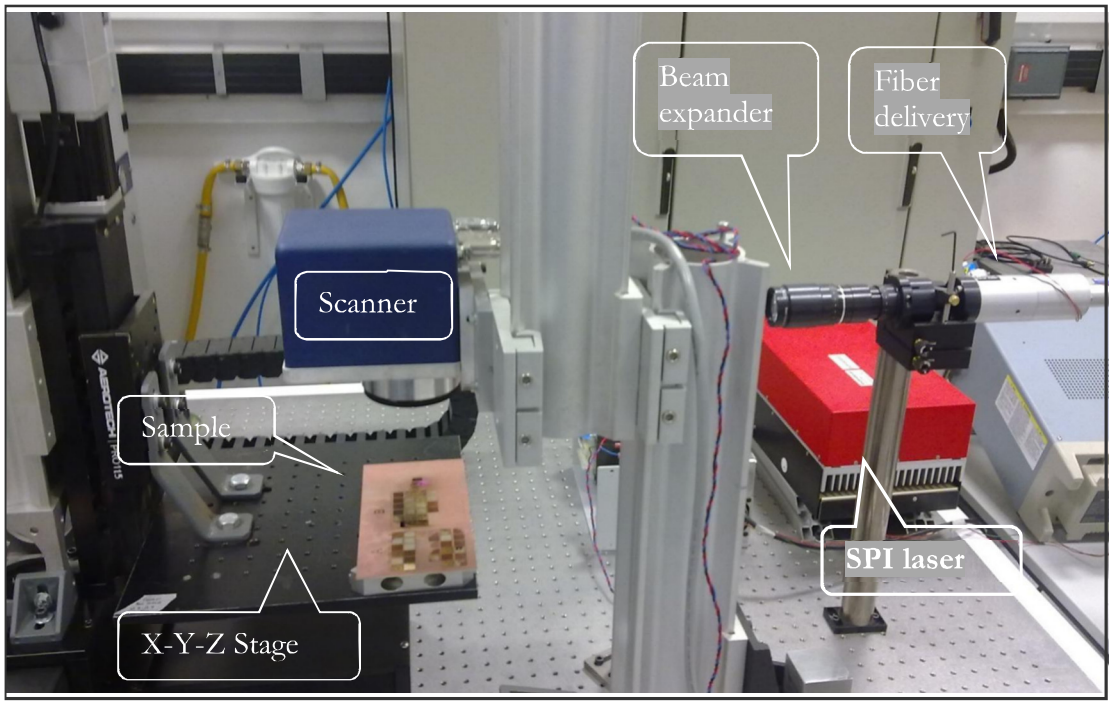

Figure (2.16): Photograph of the IR fiber delivered experiment.

The height at which the mark starts to appear is recorded and then the same procedure is repeated starting from below the focal point and the second height recorded. The exact laser focusing point is midway between these two points (Figure 2.17).

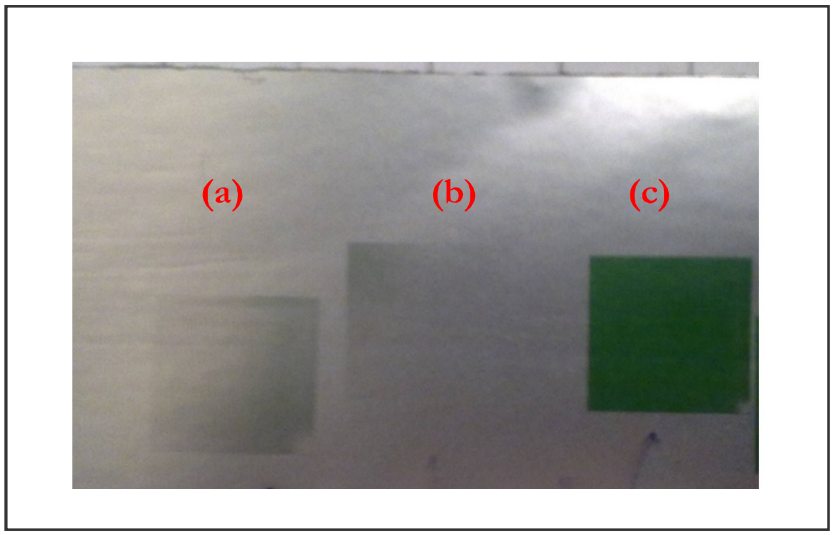

Figure (2.17): Laser mark: (a) above the focal point, (b) below the focal point and (c) at the focal point.

The PCB board substrate is then fixed on to the XYZ CNC stage and positioned at the focal point of the laser beam. A 10 x 10 mm square filled with a 30 µm hatch path in both directions is programmed in the SamLight scanner software (SCAPS). A total of 72 squares were machined, varying the laser parameters and measuring the process time for each square.

The laser parameters considered in this trial are: the scanning speed in the range of 400-1000 mm/s, number of repeated cycles (number of passes) and pulse frequency (25, 125, 250 KHz) correspond to sets of pulse width (200, 100, 30 ns). The processing details showed in appendix 2.1 and resulting machined squares are illustrated in figure 2.18 below.

The most desired result is highlighted in red in figure 2.18. This result achieved without heat damage to the base PCB board or the surrounding copper remains and the entire copper layer removed (square number 24 in figure 2.18).

The laser parameters utilised to achieve this result are: 18 W average laser power, 1000 mm/s scanning speed, 25-KHz frequency with 200-ns pulse width and 4 passes. The white colour seen in square 24 on figure 2.18 is a thin adhesive layer used for the copper layer cladding on top of the FR4 base.

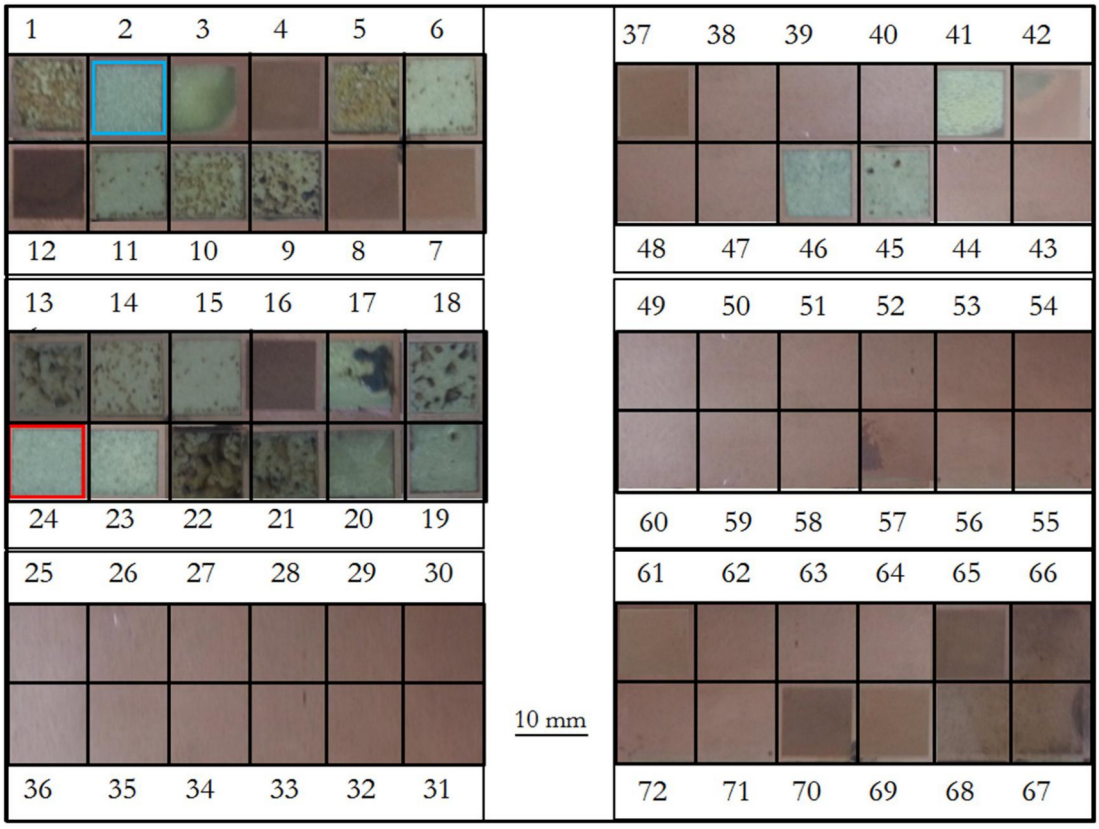

Figure (2.18): Processed sample of rigid PCB.

In some PCB boards brands this adhesive cladding layer replaced with epoxy adhesive layer (Figure 2.19).

The square highlighted in blue in figure 2.18 (square 2) is also very good and is achieved with the following parameters: Average laser power 9 W, scanning speed: 500 mm/s, pulse frequency 25 KHz, pulse width 200 ns, and 4 passes.

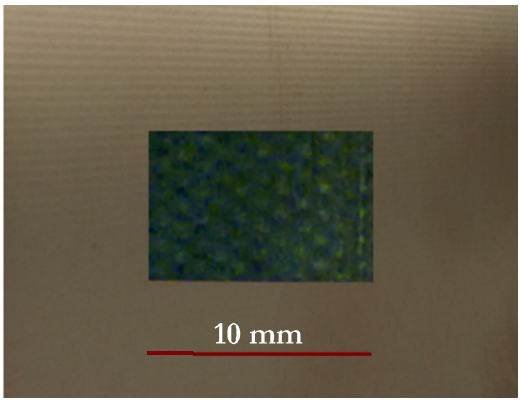

Figure (2.19): Laser machining of alternative PCB.

This set of experiments proves that rigid PCB boards can be processed without the need for a mask and chemical post processing. In addition, small features of the same size of the laser beam spot are possible. With careful beam line and optics design the laser beam can be focused down to less than 20µm with extremely narrow tracks can be structured on the PCB board compared to conventional process.

Complete isolation of the tracks to construct SRR shape (explained below) was achieved around the conductor copper lines in the laser ablated area.

The laser parameters determined in these machining trials were used to fabricate split-ring resonators (SRRs) on rigid PCB board as shown in Figure 2.20.

Figures 2.20 and 2.21 show micromachined patterns composed of double split rings resonator (SRR) and SEM image of the same SRR respectively. The thermal impact is minimized by employing the combination of a small laser spot size and nanosecond pulses that allow highly ablative process with little evidence of thermal damage.

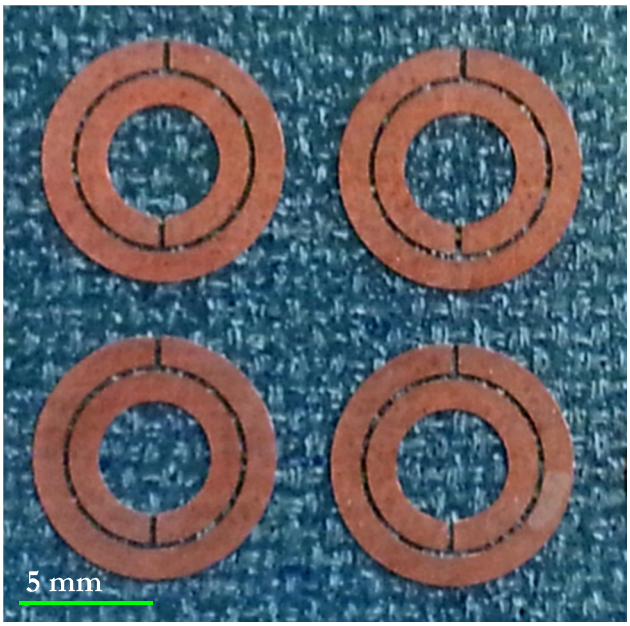

Figure (2.20): Double split ring resonator fabricated on rigid PCB board.

Figure 2.20 proves the above statement and even under scanning electron microscopy (figure 2.21) there is limited thermal effect to the surroundings with no evidence of debris.

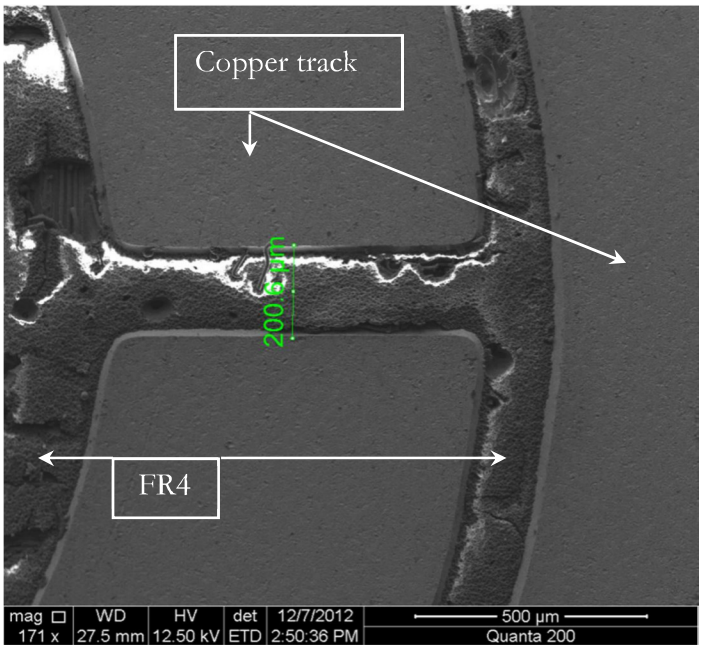

Figure (2.21): SEM Pictures of copper track on rigid PCB

In summary, laser processing of rigid PCBs is a highly controllable single step process with a high precision of material removal. Another novelty of this process is the elimination of the use of masks and the subsequent chemical etching. Therefore, the process does not contaminate the PCB being processed. The process offers a spatial resolution of tens of microns.

2.10.2 Laser processing of flexible PCB

The electronics industry continually works towards size reduction to achieve lighter devices or to convert some electronic systems to become portable with more flexibility. The dominant component of any electronic device is the Printed Circuit Board (PCB). Flexible PCB, in this case, is preferable to reduce the overall device size and can also be employed to make connections between electronics assemblies. Therefore the structuring of flexible PCB, with narrow copper tracks and spacing, would be a welcome alternative to conventional techniques of PCBs processing [40].

Design or production restrictions often require the use of flexible PCBs instead of standard rigid PCBs. The electronics manufacturing industry is producing high-density flexible PCBs in rapidly increasing quantities and the demand will grow for future electronic devices such as roll-up laptops, displays and e-paper [43].

The novelty of the UV laser technique investigated here can be summarised as directly laser structuring the top photo-resist of the untreated PCB. Subsequently, traditional etching of the flexible PCB creates the desired designed tracks.

The flexible PCB employed in this investigation consists of three layers: 40 μm flexible insulator base, 35 μm middle copper layer and 10 μm photo-resist (polymeric) top layer with overall thickness of 85 μm. The polymer photo-resist layer found with standard

flexible PCB may be replaced with other polymers that resist the etching process but do not need to be photoactivated.

Initially, an attempt to process the flexible PCB was made with the 1064nm SPI fibre laser to directly ablate the copper layer and form the necessary structures. The amount of heat generated by this process was found to damage the flexible PCB. The flexible PCB is very thin compared to the rigid PCB; therefore heat cannot be dissipated easily and it is likely that a cold-ablation technique is required to remove the copper to avoid heat damage to the substrate.

Laser material processing is governed by the interaction between laser radiation and materials. Different materials have a different response to different laser wavelengths. The laser type and wavelength selection is also determined by the required spot size and material absorption to the selected laser radiation.

Polymers or a photoresist can absorb UV light very well, thus a UV laser source is an obvious selection for this type of laser processing. This leads to the alternative approach employing a DPPS UV laser to direct structuring of the photoresist followed by conventional chemical etching.

A Quantronix Osprey pulsed (Q-switch) DPSS YAG laser frequency tripled to 355nm was employed to write the designed pattern on to flexible PCB. The laser delivers an average power of up to 2W, with pulse repetition rates up to 75 KHz, a raw beam diameter of 0.75mm and a typical pulse width of 18ns.

The beam from this laser is expanded with a beam expanding telescope (Linos) to a 10 mm spot size and delivered to a General Scanning Lightning Scanning head. The 10 mm

beam expansion diameter is chosen so that it fills the scanning head aperture (10mm diameter).

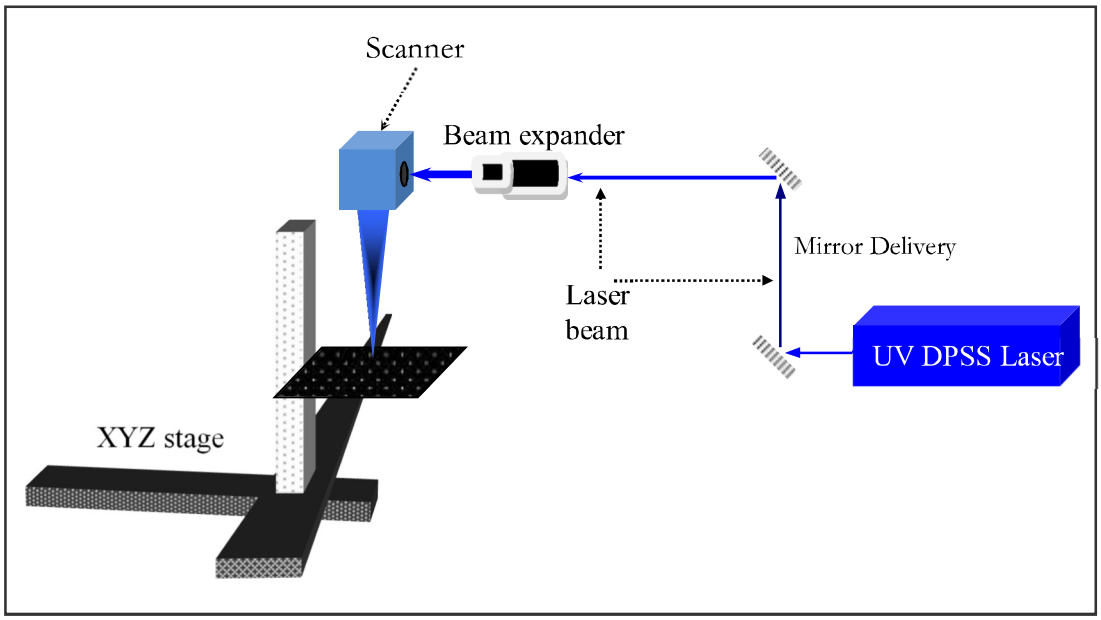

Figure (2.22): Quantronix Osprey UV laser system setup and clamping arrangement.

The laser beam is then focused through a Linos 160 mm focal length f-theta lens yielding a nominal spot size (diameter) of about 10 µm calculated as following:

$$\text{Spot Radius} = \frac{M^2 \times \text{Focal Length} \times \text{Wavelength}}{\pi \times \text{Beam Radius}} \quad ---- \quad (2.14)$$

$$= \frac{1.3 \text{ x } 160\text{x}10^{-3} \text{ x } 355\text{x}10^{-9}}{\pi \times 5\text{x}10^{-3}} x10^{6}\,\mu m = 4.7\,\mu m$$

A schematic of the system set up is shown in Figure 2.22. The structuring pattern, split ring resonators (SRR) in this case, was designed with AutoCAD software in DXF format that can be imported into the scanner software (SCAPS).

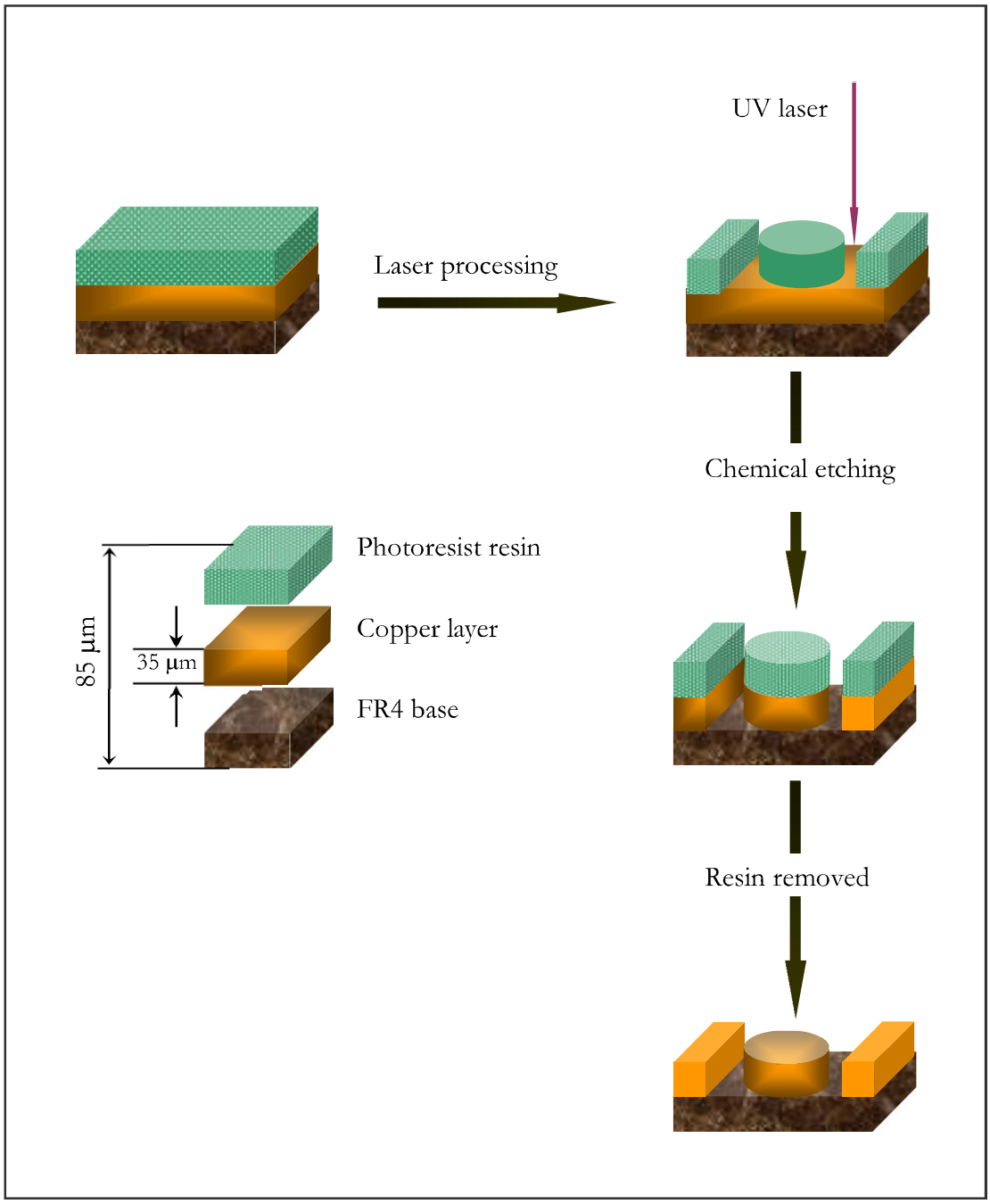

Figure (2.23): Flexible PCB processing steps [40].

The fabrication of these structures was performed using the UV laser as the requirement in this case is only to ablate the polymeric photoresist layer of the flexible PCB. The smaller spot size of the UV laser should also assist in increasing the resolution of the process. Cold ablation is the dominant mechanism in this process where the energy induced by the absorbed UV photons cause direct bond breaking of the polymer

molecular chains. The material is then removed by shattering these molecules without significant thermal damage [19]. The analogy is that UV laser produces radiation with wavelengths 355 nm equivalent to photon energies of 3.5 eV which is greater than the molecular bond breaking energy of polymers (3.0–4.8 eV) [37].

The UV laser radiation is employed to remove the polymeric photoresist area between the required tracks leaving the desired conducting tracks covered with the photoresist. The processed flexible PCB is then chemically processed with Ferric Chloride etchant to selectively remove the copper. Finally, the remaining photoresist is removed by rinsing in alkaline metasilicate, or acetone, leaving the required copper structures as can be seen in figure 2.24. The overall process steps is schematically illustrated in Figure 2.23 above.

2.11 Results

For this project, it is necessary to machine a repeated structure over a large length (>500mm) of flexible PCB. Micromachining such a relatively large area of thin film PCB imposes a substantial challenge in delivering structure accuracy and achieving feature sizes less than 50 μm.

Difficulties would be expected with the traditional photo lithography etching technique. The challenge, in this case, arises in making a precision mask for the required pattern and fixing and positioning this mask directly in proper contact with the flexible PCB board. The reason for the firm mask attachment is to prevent any UV light from illuminating other PCB area under the edge of the mask that can result in uneven structure edges or broken copper tracks and are thinner than designed. Also the minimum copper track size that can be achieved with the conventional techniques is confined to the diffraction limit [44].

With this novel laser micromachining technique, excellent size accuracy of pattern can be achieved with structure sizes of less than 50 µm. Laser processing parameters have been developed to achieve this result without damaging or affecting the base material and surroundings.

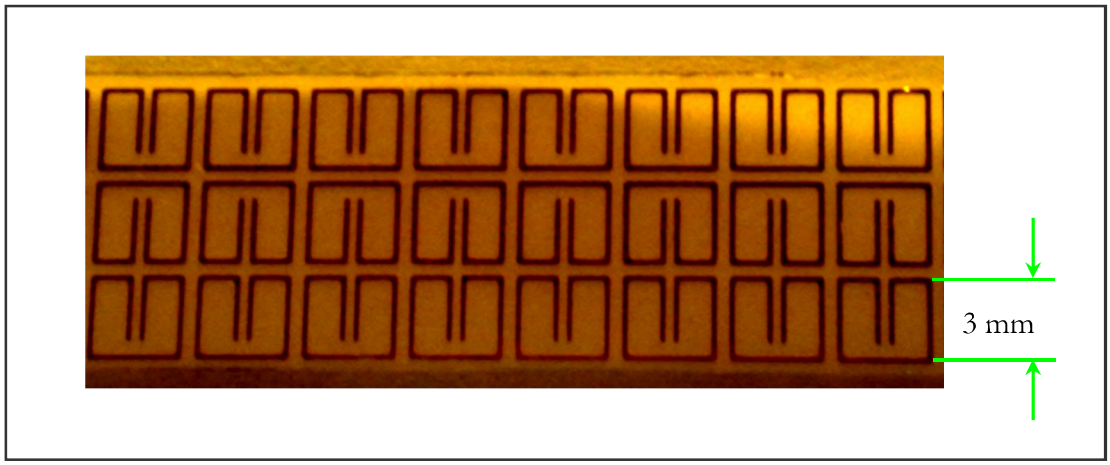

Figure (2.24): Image of SRRs machined on flexible PCB strip of 10 mm height.

The aim of this research is to fabricate Split Ring Resonators (SRR) on flexible PCB materials using laser processing approaches. These SRRs are the unit cells of an electromagnetic metamaterial [1]. Metamaterials are sub-wavelength periodic conductive structures that are separated by insulator. The fabricated SRRs (figure 2.24) will be employed to construct electromagnetic cloak that is explained in details in chapter 5 "Optical Transformation and Cloaking".

2.12 Scale Down SRR And Physical Test

One of the reasons of using laser technique for processing flexible PCB is the possibility of achieving smaller feature size compared to conventional PCB processing techniques. Consequently, the smaller SRRs can result in achieving metamaterials active in shorter wavelengths as will be explained in chapter 3.

The UV laser was used to machine 1.5 mm^2 and 3 mm^2 SRRs (Figure 2.25 (A) and (B)) with track wire widths of 35 µm and 200 µm respectively (Figure 2.25 (C) and (D)). The laser parameters used for this experiment were: Scanning Speed: 400 mm/s, Laser Power 1W, Pulse Frequency 20 KHz, 25 µm hatch spacing, and 3 passes.

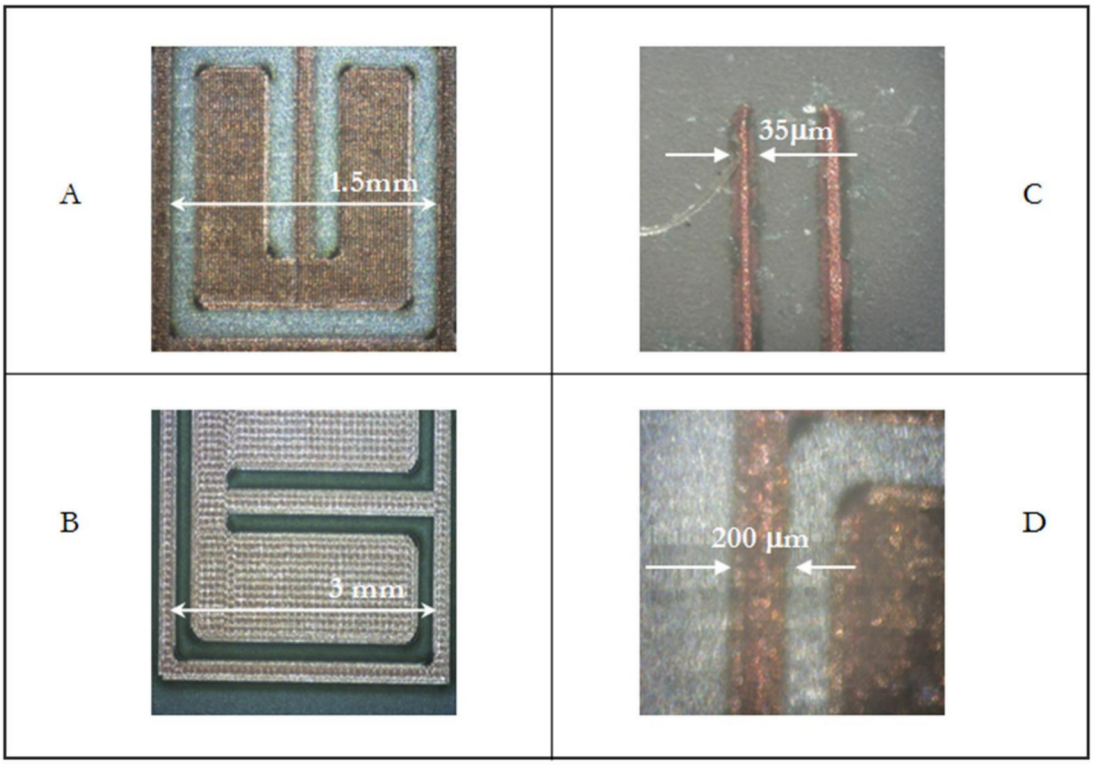

Figure (2.25): SRR scaled down to (a) 50% and (b) 70% compared with SRR 100% in both (c) and (d).

Figure 2.25 (A) and (B) shows optical microscopic images of SRRs structured on flexible PCB after UV laser micromachining of the surface photoresist layer.

While Figure 2.25 (C) and (D) illustrate the final PCB state after chemical etching followed by alkaline cleaning.

The large unit cell with 200 μm track is the one used to construct the microwave cloak explained in chapter 5. While the narrow track of 35 μm is the smallest track width achieved with this experiment configurations.

2.12.1 Scanning Electron Microscopy (SEM)

A (Quanta 200) Scanning Electron Microscope was employed to examine the fabricated SRRs samples that were structured on a flexible PCB (figure 2.26). The flexible PCB strip were cut to 5x5 mm squares that contain single SRR and were mounted on the SEM sample holder using double sided adhesive tape.

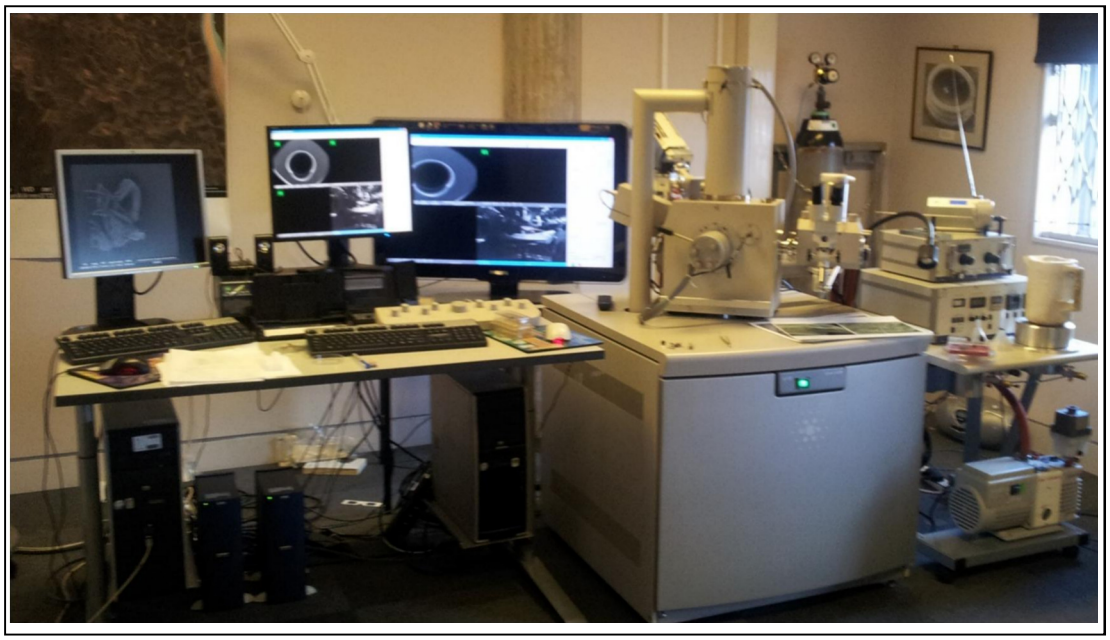

Figure (2.26): Photograph of the Quanta 200 SEM.

SEM imaging was performed on these SRRs to measure the unit cell dimension (Figure 2.27 a) and to investigate machining accuracy (Figure 2.27 b).

The SEM test was also employed to analyse the material composition in the machined area. The Energy-dispersive X-ray spectroscopy (EDX) analysis was conducted on the

5x5 mm^2 flexible PCB to establish that this laser processing technique was fully removing the copper in the desired area and not leaving any copper in the non-conducting region.

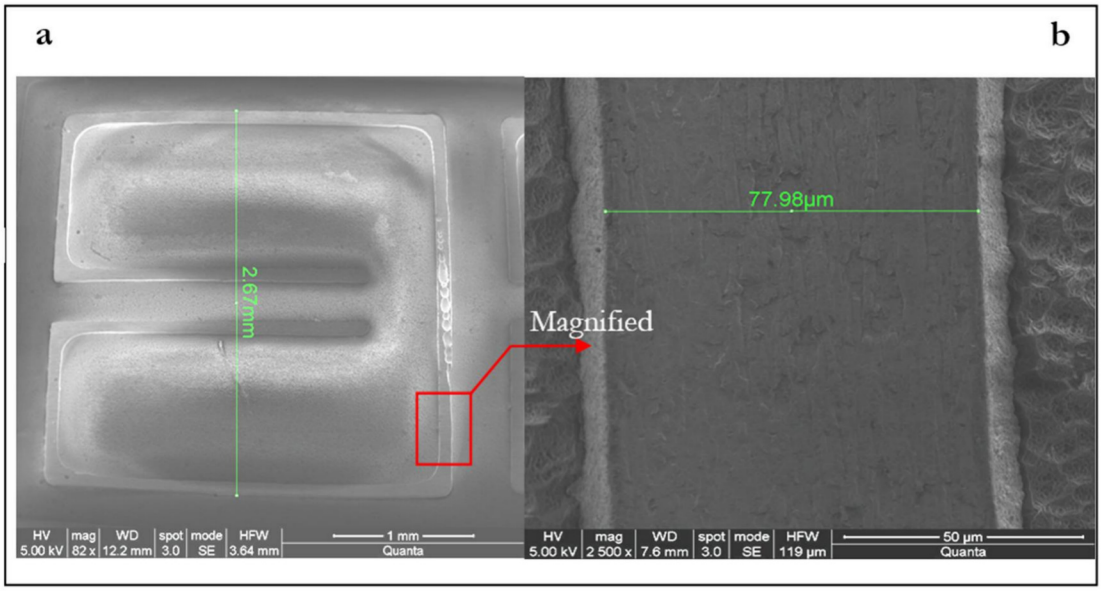

Figure (2.27): SEM image and measurement of: (a) SRR width and (b) wire thickness.

The magenta colour in figure 2.28 indicates that the copper track is well defined, with no evidence of remaining copper in the insulating regions. The results of this EDX scan can be seen in detail in appendix 2.3.

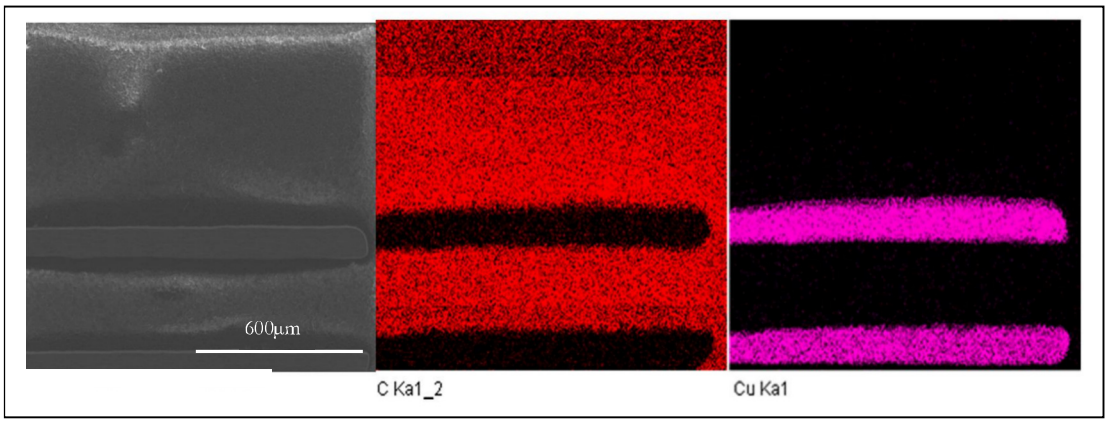

Figure (2.28): EDX analysis of etched copper track.

2.13 Summary

In this chapter, laser material interaction and the development of PCB processing techniques had been demonstrated. The importance of laser radiation absorption by materials is described together with material classification and how does each type of these materials influence the laser wavelength choice is debated.

The use of lasers as a rapid prototyping tool to process rigid PCB with an IR fibre laser has been proven for directly micromachining rigid PCB without the need for any chemical or masks to create the required patterns. A comparison between the proposed laser-PCB processing technique with conventional techniques had been discussed. Experiments on both flexible and rigid PCB have been demonstrated in this chapter with details of results achieved in processing both rigid and flexible PCBs together with the scaling down in size of the resultant structures

A Q-switched DPSS UV laser was employed in processing flexible PCB without the need of a photo-sensitive resist and also eliminating the use of masks. The UV laser was used to directly write the designed pattern on top of the polymeric layer of flexible PCB. This is followed by chemical etching. This technique demonstrated in Figure 2.23 of this chapter is unreported in the literature including patents.

Laser PCB processing is a non-contact technique therefore there is no physical contact between machining tool (laser) and the workpiece. This prevents contamination of the PCB and reduces possible gradual wear of the part. Laser is particularly suited for processing, when required, at an angle with the surface of the workpiece.

Another advantage of laser processing over conventional techniques is the possibility to process a difficult to reach parts or even repair PCB boards without the need to remove the part from the device.

UV Laser processing flexible PCB can be achieved with breaking of chemical bonds of the polymeric layer rather than melting and evaporation, leaving virtually no recast layer and HAZ due to the fact that there is hardly any heat generation.

Compared to conventional lithography technique, the remarkably reduced process steps and processing time together with smaller feature sizes open the door to develop high-performance multilayer flexible electronics

Appendix 2.1: Rigid PCB laser processing log data

No.	Speed mm/s	Power W	Frequency KHz	Pulse width ns	Hatch um	Wave forms	Pass
1	400	9	25	200	30	0	4
2	500	9	25	200	30	0	4
3	600	9	25	200	30	0	4
4	1000	9	25	200	30	0	4
5	400	10	25	200	30	0	4
6	600	10	25	200	30	0	4
7	800	10	25	200	30	0	4
8	1000	10	25	200	30	0	4
9	400	12	25	200	30	0	4
10	600	12	25	200	30	0	4
11	800	12	25	200	30	0	4
12	1000	12	25	200	30	0	4
13	400	14	25	200	30	0	4
14	600	14	25	200	30	0	4
15	800	14	25	200	30	0	4
16	1000	14	25	200	30	0	4
17	400	16	25	200	30	0	4
18	600	16	25	200	30	0	4
19	800	16	25	200	30	0	4
20	1000	16	25	200	30	0	4
21	400	18	25	200	30	0	4
22	600	18	25	200	30	0	4
23	800	18	25	200	30	0	4
24	1000	18	25	200	30	0	4
25	400	9	125	30	30	2	4
26	600	9	125	30	30	2	4
27	800	9	125	30	30	2	4
28	1000	9	125	30	30	2	4
29	400	10	125	30	30	2	4
30	600	10	125	30	30	2	4
31	800	10	125	30	30	2	4
32	1000	10	125	30	30	2	4
33	400	12	125	30	30	2	4
34	600	12	125	30	30	2	4
35	800	12	125	30	30	2	4
36	1000	12	125	30	30	2	4
37	400	14	125	30	30	2	4

38	600	14	125	30	30	2	4
39	800	14	125	30	30	2	4
40	1000	14	125	30	30	2	4
41	400	16	125	30	30	2	4
42	600	16	125	30	30	2	4
43	800	16	125	30	30	2	4
44	1000	16	125	30	30	2	4
45	400	18	125	30	30	2	4
46	600	18	125	30	30	2	4
47	800	18	125	30	30	2	4
48	1000	18	125	30	30	2	4
49	400	9	250	30	30	3	4
50	600	9	250	30	30	3	4
51	800	9	250	30	30	3	4
52	1000	9	250	30	30	3	4
53	400	10	250	30	30	3	4
54	600	10	250	30	30	3	4
55	800	10	250	30	30	3	4
56	1000	10	250	30	30	3	4
57	400	12	250	30	30	3	4
58	600	12	250	30	30	3	4
59	800	12	250	30	30	3	4
60	1000	12	250	30	30	3	4
61	400	14	250	30	30	3	4
62	600	14	250	30	30	3	4
63	800	14	250	30	30	3	4
64	1000	14	250	30	30	3	4
65	400	16	250	30	30	3	4
66	600	16	250	30	30	3	4
67	800	16	250	30	30	3	4
68	1000	16	250	30	30	3	4
69	400	18	250	30	30	3	4
70	600	18	250	30	30	3	4
71	800	18	250	30	30	3	4
72	1000	18	250	30	30	3	4

Appendix 2.2: Measuring laser beam diameter using power meter

Two experiments were performed to calculate the laser beam diameter of a 20 watt SPI G3.0 pulsed fibre laser system which emits infrared radiation of 1064 nm. The laser can be operated in CW or pulse mode with frequency range between 1 to 500 kHz and pulse width of 9-200 ns.

A thin ceramic blade (30x30x0.75 mm) is attached to a high precision linear stage (Aerotech PRO115) as shown in Figure 1 below.

The blade surface was positioned at the focal point using the technique described in section 2.10.1 and a 10mm line in the Y direction programmed in the scanner's software (SamLight). The laser parameters considered in this experiment are: the scanning speed (1000 mm/s), laser power (3 w), pulse frequency (25 kHz), pulse width (200 ns), and number of passes (continuous).

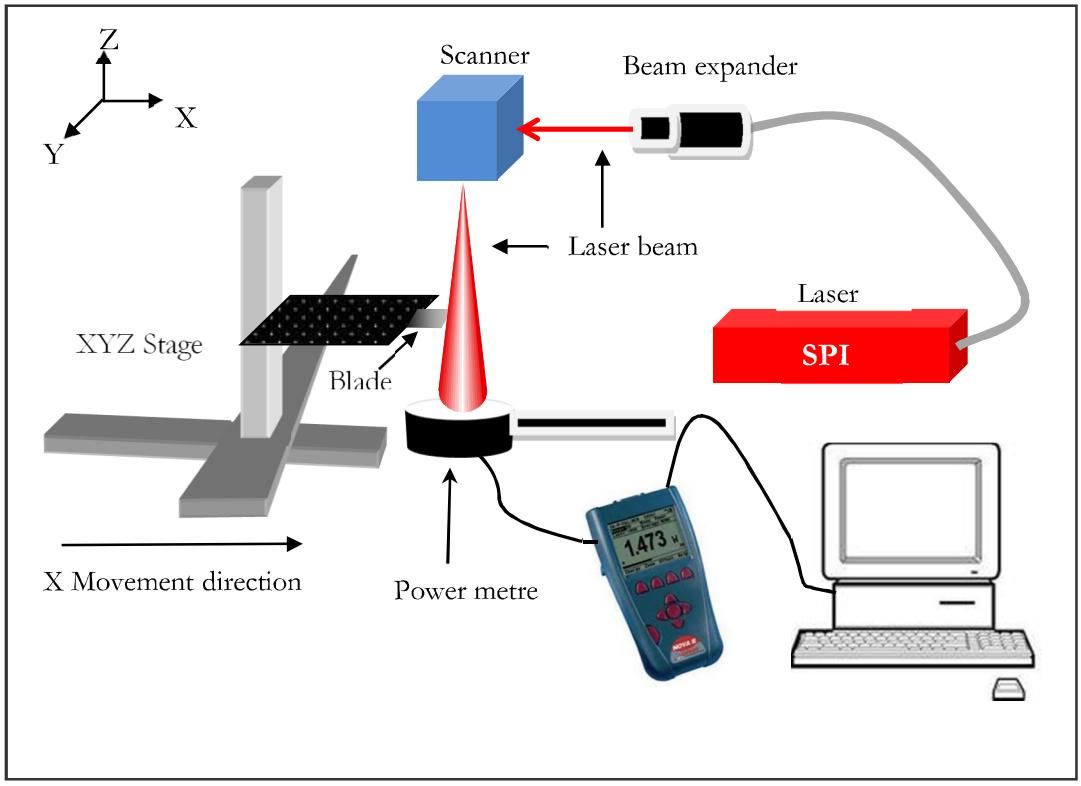

Figure (1): Experimental setup.

The laser power is measured with an OPHIR Nova II - Laser Power Meter & Energy Meter with the meter head fixed below the focal point such that the laser has expanded to a safe diameter but is smaller than the head sensor aperture. The power meter was connected to the computer USB Port to save and visualise data using StarLab 2.11 software.

The linear stage is programmed to move in the X direction starting from just before the laser beam at 0.5 mm/min for 2mm. The control programs have to be started together: SamLight to fire the laser, N-view to move the table, and StarLab to start collecting power measurement data.

StarLab then generates a graph of the power measured vs time (Figure 2). For a more detailed graph, the raw data can be saved as a text file and plotted using MS-Excel (Figure 3).

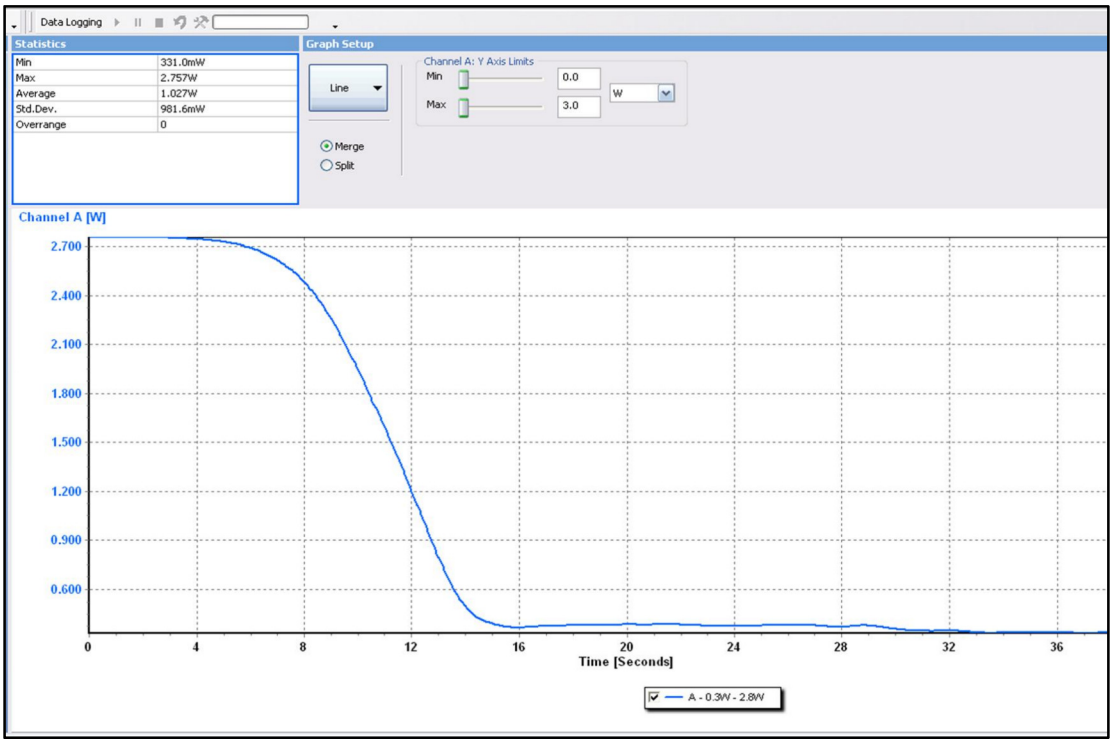

Figure (2): Result from StarLab with the table moving at 0.5mm/min.

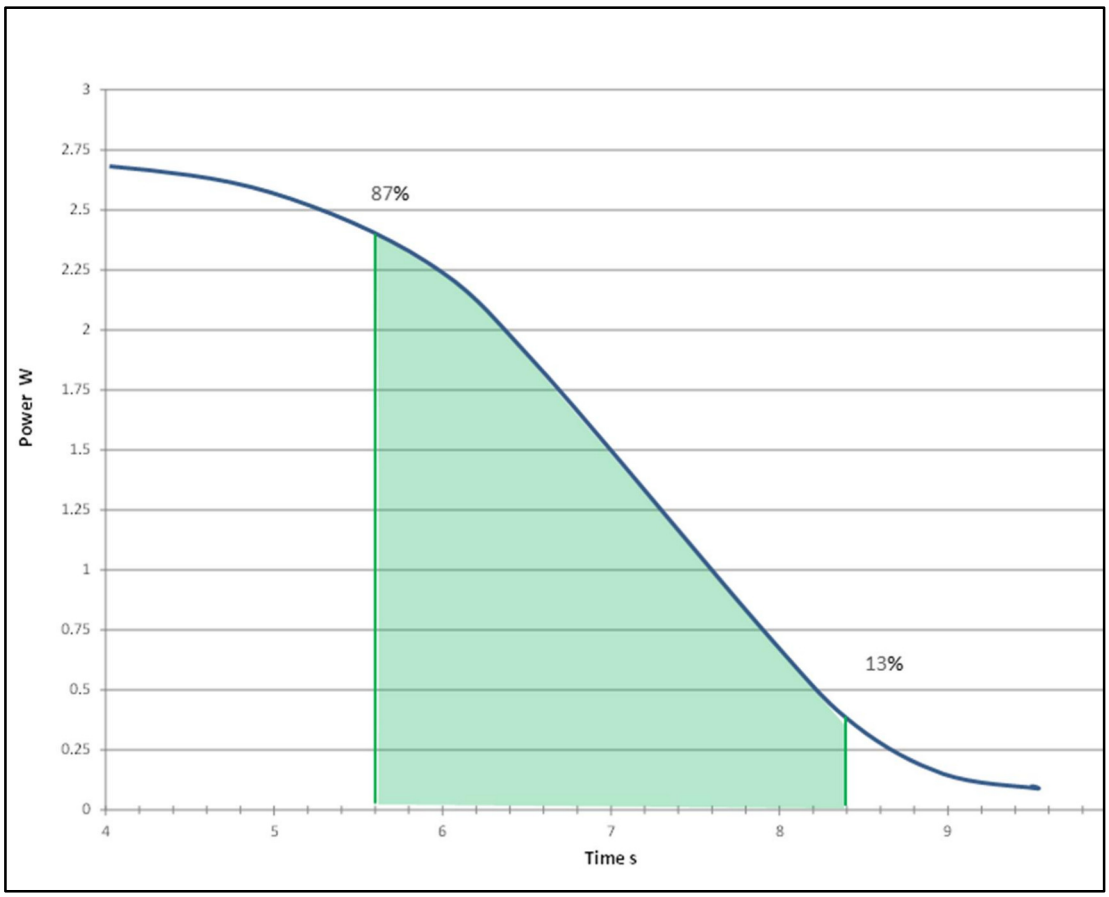

Figure (3): Raw data taken from power meter.

Calculation

Based on Gaussian beams the spot size as measures at the 87% and 13% points of the maximum power, then the time interval between these points can be calculated as following :

87% of 2.7 W = 2.35 W at time 5.6 s and 13% of 2.7 W = 0.35 W at 8.4 s

Time interval between the two point = 8.4-5.6 = 2.8 s = 0.046 min

So spot diameter = 0.5 mm/min * 0.046 min = 0.023 mm = 23 μm

Spot diameter = 0.5 mm/min X 0.043 min = 0.021mm = 21μm

Appendix 2.3: EDX Data for SRR Image

Livetime 50.1 s

Acquisition geometry (degrees):
Tilt = 0.4
Azimuth = 0.0
Elevation = 35.0

Accelerating voltage = 20.01 kV

Total spectrum counts = 55540

Sample data :	Energy (eV)	Resn. (eV)	Area
Strobe :	7.5	50.81	557993
Optimization data : Silicon K series			
	Energy (eV)	Resn. (eV)	Area
Strobe :	-.1	52.61	269617
Optimization element :	1742.6	84.65	469938

Sample is unpolished X-ray corrections may be approximate.
Sample is uncoated
The element used for optimization was Silicon
Thresholding has been selected : All quantitative results below 2 sigma have been set to zero
Detector efficiency : Read from file (x-act 3.efy)
Pulse pile up correction performed.

Spectrum processing :
Peak possibly omitted : 3.700 keV

Processing option : All elements analyzed (Normalised)
Number of iterations = 3

Element	App Conc.	Intensity Corrn.	Weight %	Weight % Sigma	Atomic %
C K	3.34	0.9436	52.07	1.31	60.70
O K	1.54	0.5527	41.82	1.29	36.60
Na K	0.10	0.7709	1.95	0.26	1.19
Si K	0.07	0.8913	1.15	0.12	0.57
P K	0.07	1.2768	0.80	0.12	0.36
Cl K	0.02	0.8124	0.29	0.09	0.12
Fe K	0.08	0.7898	1.51	0.18	0.38
Cu K	0.02	0.7469	0.40	0.15	0.09
Totals			100.00		

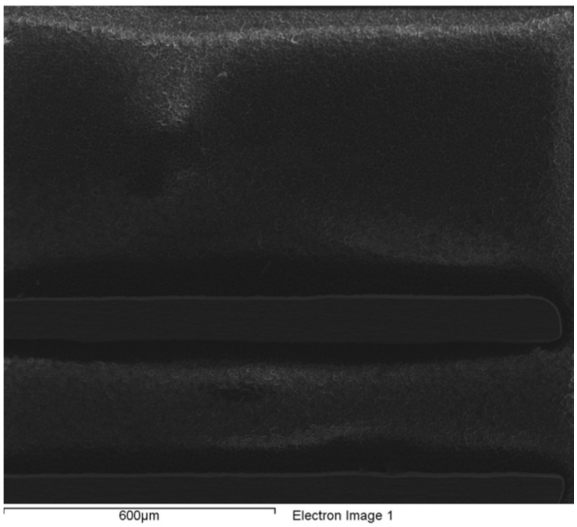

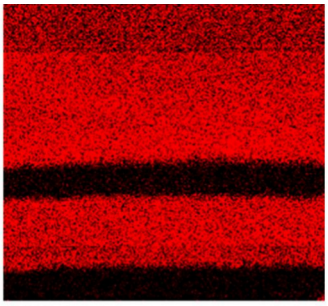

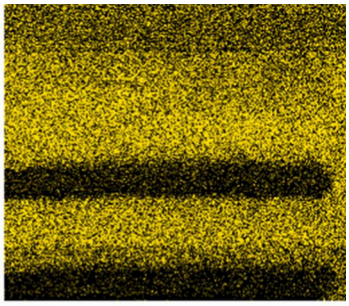

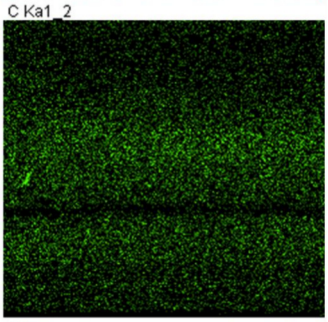

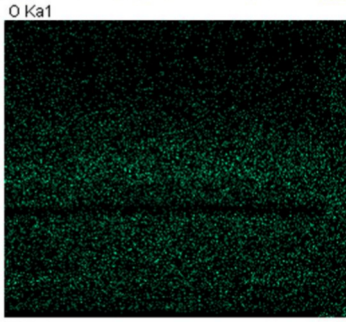

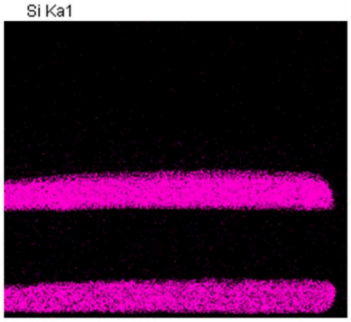

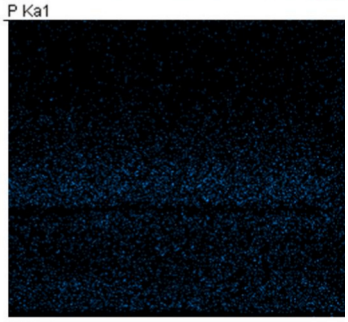

Comment: Element analyses of the area between the copper wires and the wire itself to visualise the presence of copper and investigate other residual materials.

Clearly the magenta colour proves complete removal of the copper element from the desired area.

Quantitative results

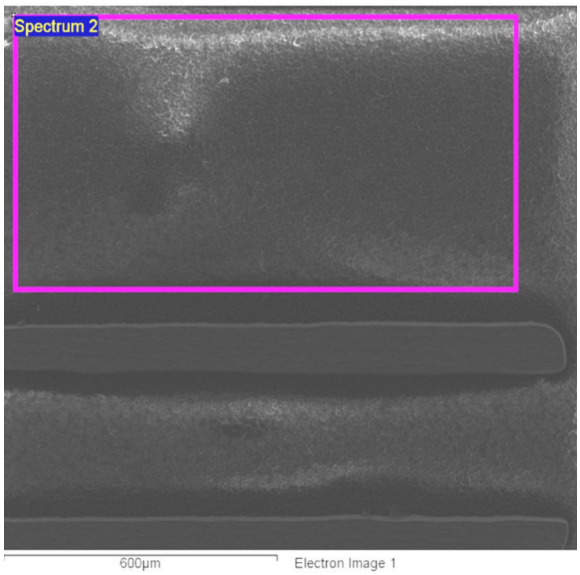

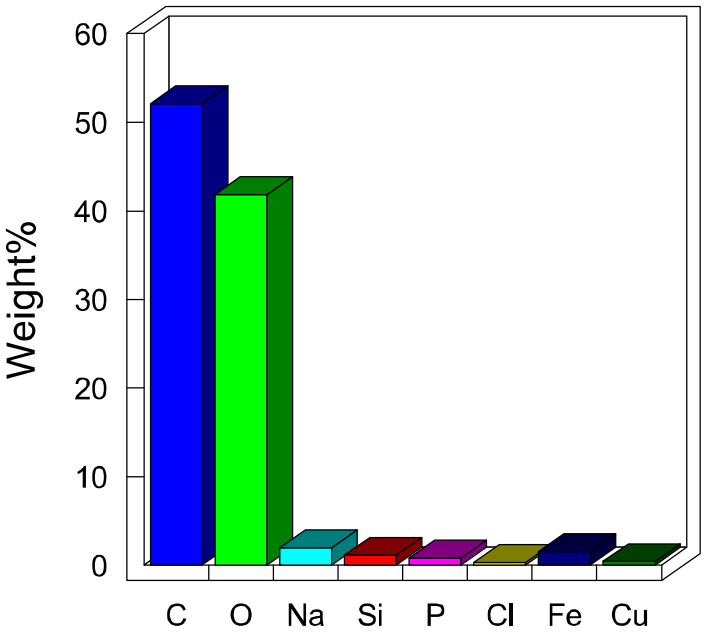

Comment: quantitative analysis of the area between the copper wires that shows copper percentage remaining in this area.

The chart shows 0% of copper and high percentage of carbon and oxygen in the area between the wires.

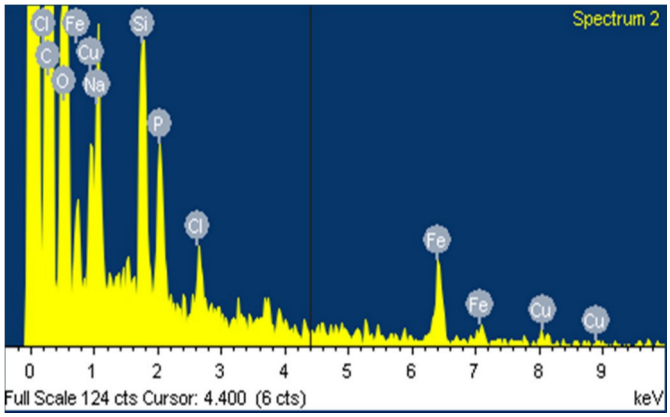

Chapter 3

Split ring resonator structure and electromagnetic resonance mechanism

3.1 Introduction

A Split Ring Resonator (SRR) is a conductor in the shape of a ring that has a break in it, (Figure 3.1). An electromagnetic wave couples to the resonator by inducing an alternating current in the conductor. This current passes back and forth along the ring. When the time taken to pass from one end of the resonator and back is the period of the electromagnetic wave, a resonance occurs. There are many research studies to understand the underlying physics and the mechanism of the SRR's magnetic resonance. This magnetic resonance makes the effective magnetic permeability of the material negative at the resonant frequency. Thus, SRRs play an important role in the construction of left handed metamaterials (LHM) that possess a negative index of refraction [46-53].

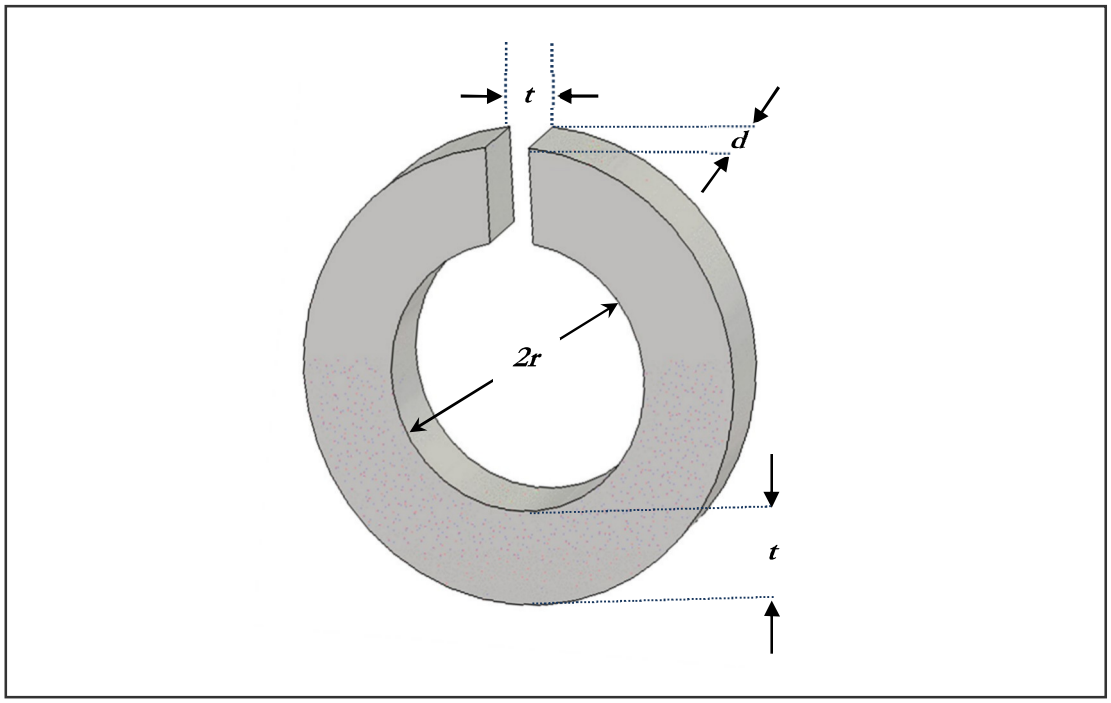

Figure (3.1): A Split Ring Resonator and its characteristic dimensions.

A single split ring resonator can be considered as an LC circuit where the capacitance and the inductance can described by the usual textbook formula [54]. The capacitance is due to the split (*t*) (Figure 3.1) that prevents current flowing around the ring and the ring

itself is considered to be a coil of one turn. An L-C circuit system is one of the analytical models in the literature studying the electromagnetic properties of the SRRs [54]. In this model the unit cell size (open ring) must be around 10^{th} of the required wavelength to have the resonance effect. This is a general rule of thumb for metamaterials to be effectively working at a certain frequency which can be easily proven using a simplified open ring shown in (Appendix 3.1).

A simplified case where the width of the ring metal is equal to the distance between the capacitor plates (t) hence the capacitance (c) would be:

$C = \varepsilon_o \varepsilon_c \, t \, d / t$ where: d is the metal thickness and ε_c is the permittivity of the material in between the plates. Similarly the inductance (L) is:

$L = \mu_o \pi r^2 / d$ where: r is radius of the coil

LC-resonance frequency: $\omega_{LC} = \frac{1}{\sqrt{LC}} = \frac{1}{r\sqrt{\pi}} \frac{c}{\sqrt{\varepsilon_c}}$; and the resonance wavelength:

$$\lambda_{LC} = \frac{2\pi c}{\omega_{LC}} = 2\pi\sqrt{\pi}\sqrt{\varepsilon_c}\; r$$

For FR4 base the permittivity $\varepsilon_c \approx 4$; therefore $\lambda_{LC} \approx 10 \times 2r$.

The most recognised SRR model in the study of metamaterials is the one proposed by Pendry which consist of two concentric open rings [1]. The total capacitance of this SRR unit cell mainly depends on two factors, one arising from the splits in each ring and the other from the gap between the concentric rings. In this design, inductances arise from the gap between the inner and outer rings and the conducting rings [54].

In this chapter the effect of varying certain geometrical parameters of a single SRR on the magnetic resonance frequency will be investigated. Parameters to be considered in

the following sections are: split cut width, gap between the rings, ring width, dielectric constant of the substrate and substrate thickness. Also, in this chapter, split rings resonators with several splits are investigated.

The SRR unit cells under investigation are fabricated in concentric copper rings on a dielectric printed circuit board (PCB). This PCB consists of two layers; copper layer with a thickness of 35 μ and FR4 layer. The overall thickness of the PCB is 1.6 mm and dielectric constant of the FR4 substrate material is 4.0.

Experimental measurements are obtained by positioning these single split rings into a microwave testing system to find their transmission and indication of resonance. The testing system consisted of Anritsu network analyser Model No 37397D VNA coupled to two monopole antennas (Figure 3.2). The two monopole antennas are used to transmit and detect the electromagnetic waves through the single SRR unit cell.

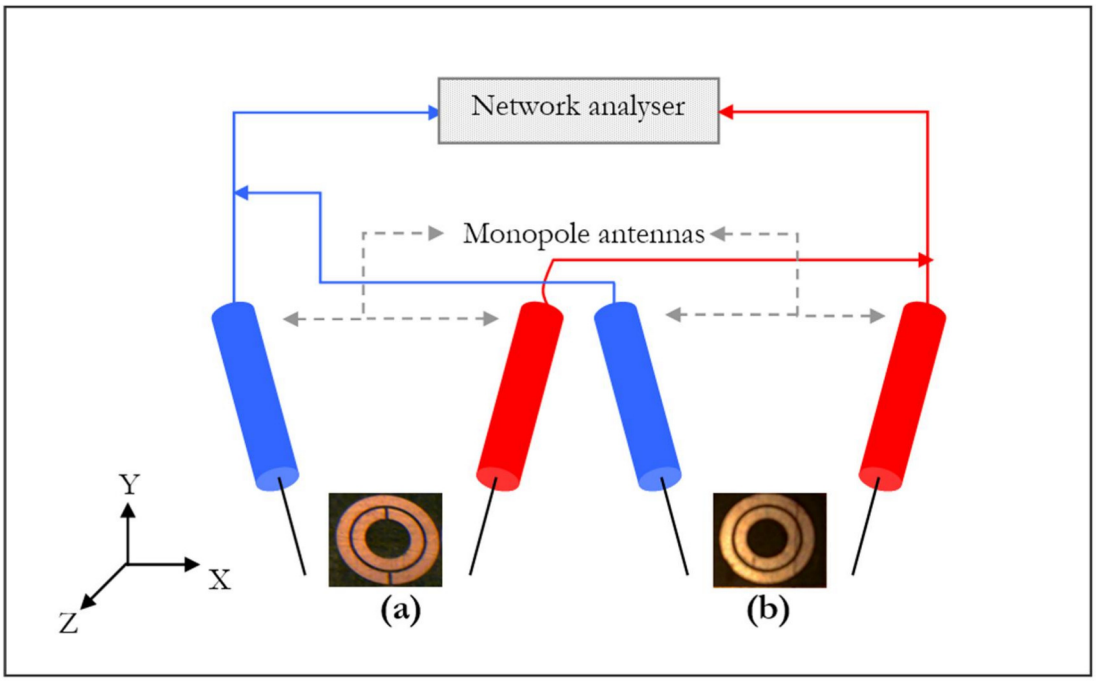

Figure (3.2): Experimental setup for measuring transmission through two monopole antennas of (a) single unit cell of the SRR structure and (b) close-ring structure.

The monopole antenna was constructed by soldering a copper wire on to an N-type connector. The monopole antenna is adjusted to operate at around 3.5 GHz by connecting each antenna individually to the network analyser and performing real-time measurements of the reflection (S11, i.e. the analyser measures the signal that is both sent and received from port 1). Then the length of the wire was reduced gradually up to the length at which the S11 peak reaches 3.5 GHz (Figure 3.3). The final length of the monopole antennas was found to be 41 mm which is of the order of $\lambda/2$. The 3.5 GHz operating frequency is taken from predicted results obtained from simulations commercial software; CST Microwave Studio.

The monopole antennas were aligned to each other and the whole system calibrated in open space to remove the effects of microwave reflections and other noise. The single SRR unit was then inserted between the monopole antennas and the transmission measurements (S21) performed. The distance between the transmitter and receiver monopole antennas is kept fixed for all the following measurements.

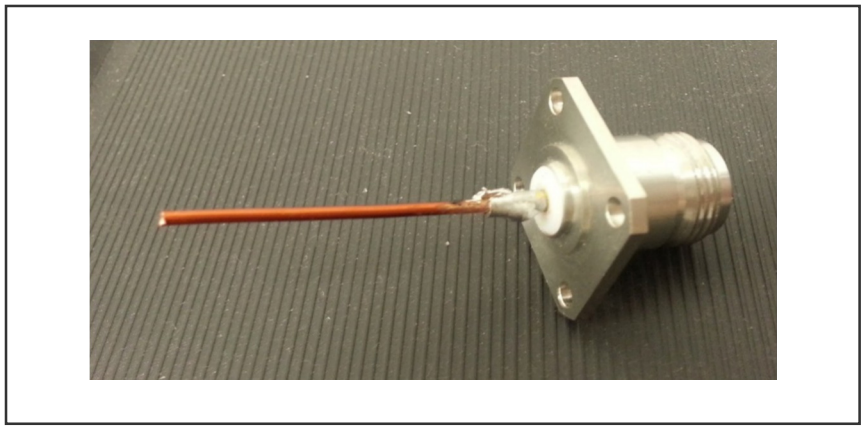

Figure (3.3): Constructed monopole antenna.

In the following sections (3.2), the measured results are compared with simulation results obtained from CST Microwave Studio software. CST Microwave Studio is a 3D full-wave solver, employing the finite integration technique (FIT).

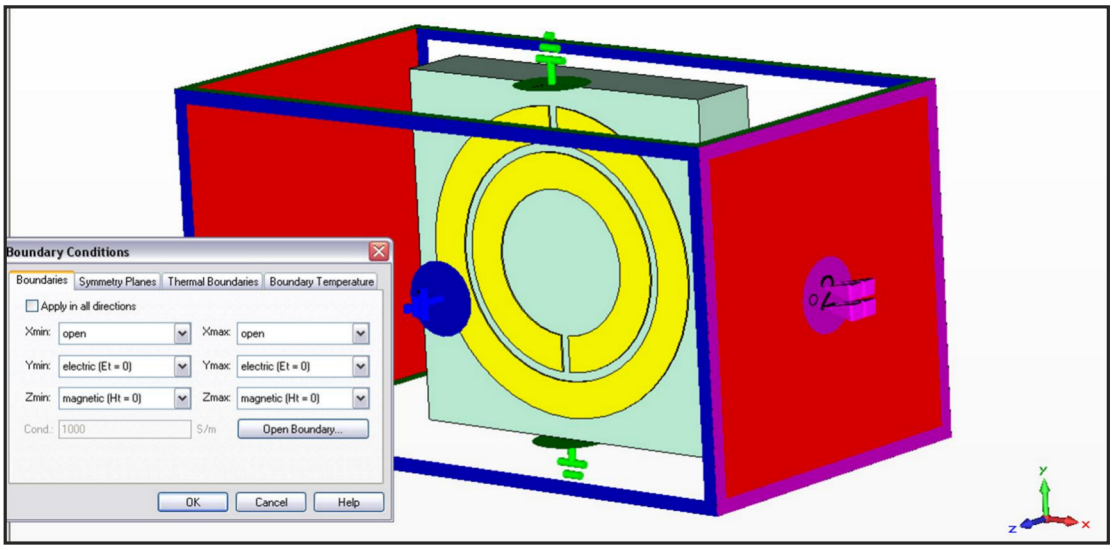

Figure (3.4): Simulation setup for single SRR unit cell.

Each single SRR structure is designed in AutoCAD and then exported as a DXF file to be used in CST software. This imported SRR shape is positioned along the propagation direction of an incident plane wave. Open boundary conditions are employed along the propagation direction (+x and -x). Electric (E_t =0) boundary conditions are used for (–y and +y) direction and magnetic (H_t =0) boundary conditions are used for (–z and +z) direction (Figure 3.4).

The calculated transmission spectrum (S21) is plotted against the frequency and compared with measured results for all individual SRRs.

3.2 Effect of SRRs shape and geometrical dimensions on magnetic resonance frequency

It is anticipated that understanding the effect of these parameters will help to realise the geometry of SRR metamaterial structures with magnetic resonance in the desired frequency regime, and thus how to proceed to manufacture these. The following sections will show that changing the physical shape of the single SRR will change the

capacitance or the inductance or both, which leads to a change in the resonance frequency. Also, the effect of the physical and chemical properties of the material surrounding the SRR will be explored in terms of its resonance frequency.

3.2.1 Effect of the split cut width on resonance frequency

In this section, the effect of varying the split cut width (*t*) on the resonance frequency of individual SRR's is investigated. The schematic drawing of the individual SRR is given in Figure 3.5 which is based on Pendry's model with geometrical modifications to make the fabrication process easier and to operate at a desired frequency range.

Initially the parameters were set to the following values:

Split cut width (*t*) =0.2 mm, gap between rings (*d*) = 0.2mm, ring width (*w*) = 0.8mm and radius of the inner ring (*r*) = 1.6mm.

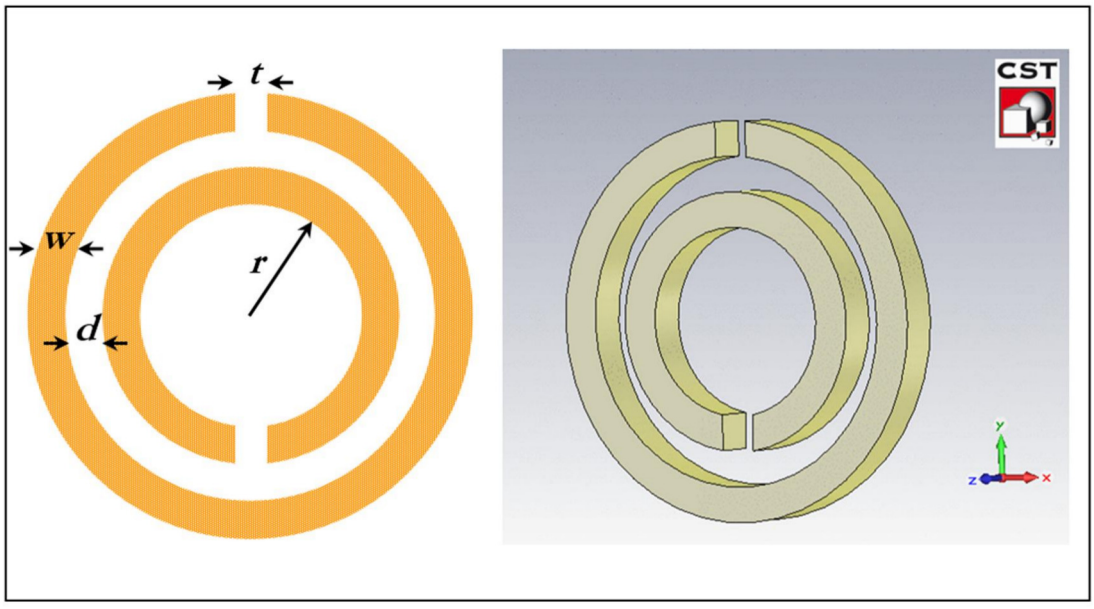

Figure (3.5): Geometry of a Split Ring Resonator as used by Pendry [1].

Only the split cut width (t) is changed from 0.0 mm to 0.6mm increasing in 0.1 mm steps with all other parameters being kept constant.

The dielectric constant of substrate = 4.0, copper thickness= 35 μm and substrate thickness = 1.6 mm

Split ring resonators were fabricated on rigid PCB using laser machining as described in Chapter 2 and reference 11 with an example shown in Figure 3.6.

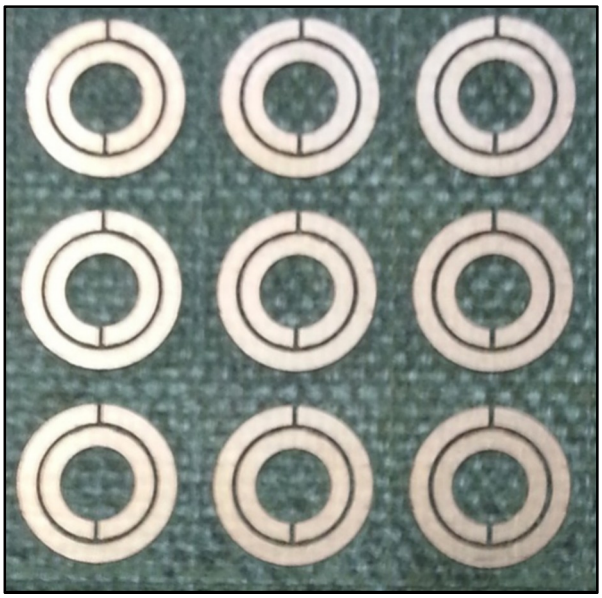

Figure (3.6): A laser machined split ring resonator.

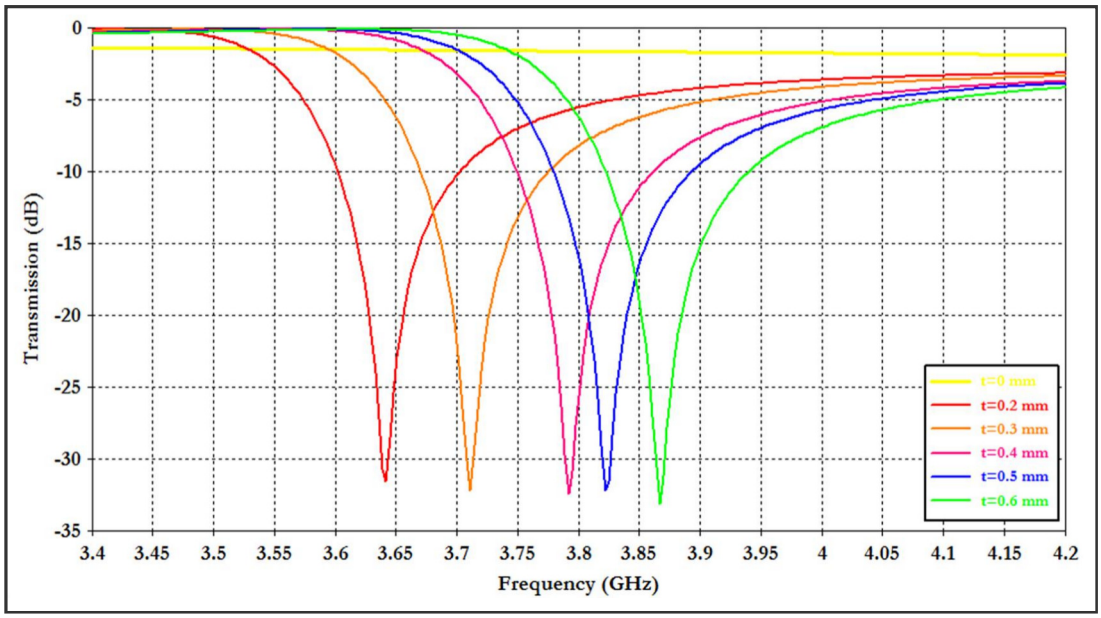

Figure (3.7): Simulation of the microwave transmission through SRR's.

The VNA sweeps the microwave frequencies from 3 GHz to 6 GHz and plots the transmission of the microwave beam through the split ring resonator.

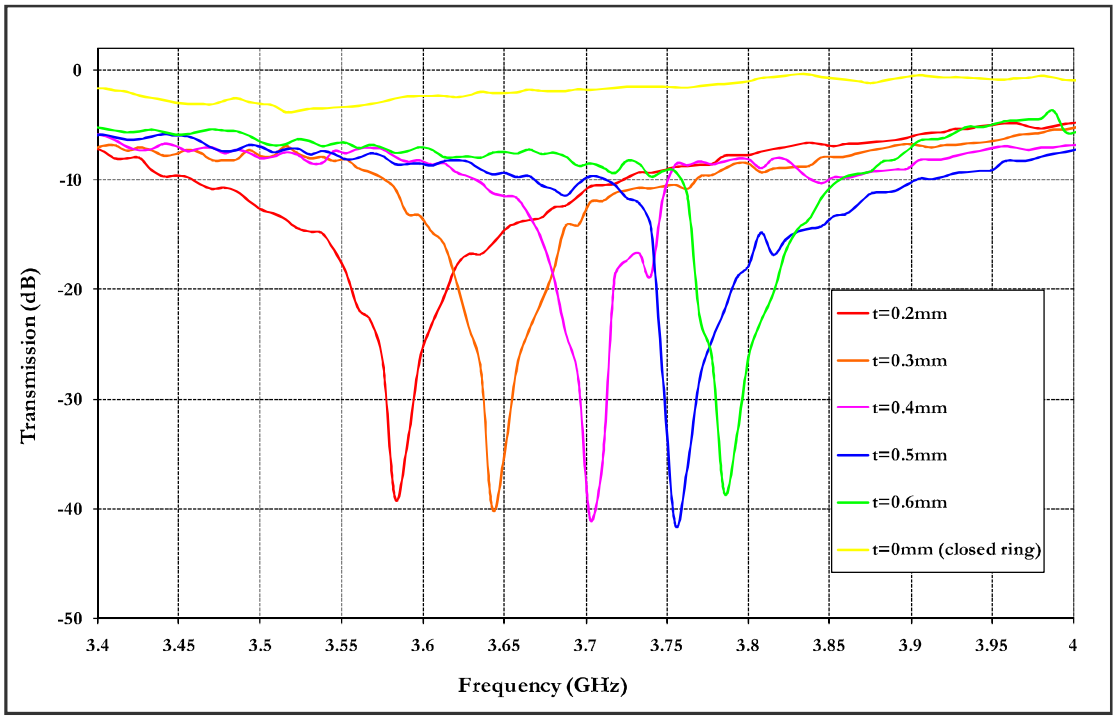

Figure (3.8): Measurements of the microwave transmission through SRR's.

Figures 3.7 and 3.8 show the simulated and measured transmission spectra of 6 SRRs structures with different split widths (t = 0.0, 0.2, 0.3, 0.4, 0.5 and 0.6 mm).

All SRR structures used in this experiment showed a dip in the transmission spectra at their resonance frequency, except the closed ring that shows no resonance at any measured frequencies. A good agreement can be seen in figure 3.9 between experimental results and the numerical simulations.

From figure 3.9 it is clear that the resonance frequency shifted to a higher value when the split cut width increased. This shift in the resonance frequency can be explained by considering the splits as behaving like a parallel plate capacitor.

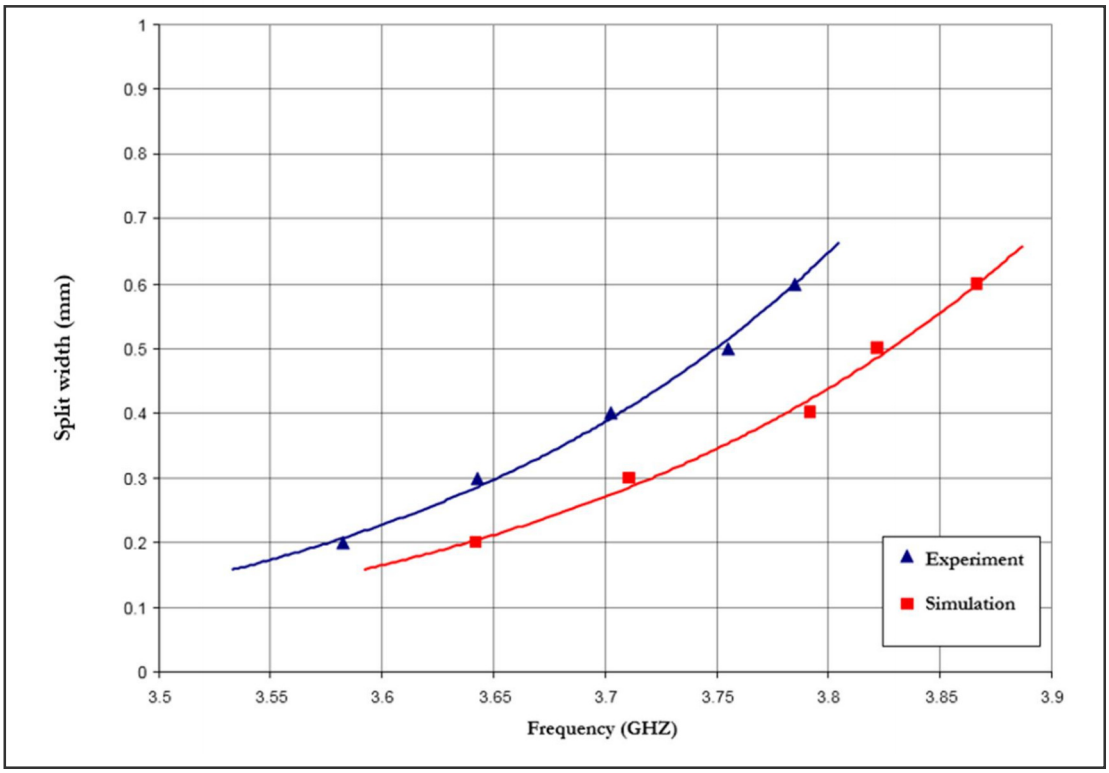

Figure (3.9): Split cut width vs. Resonance frequency for both experiment and simulation.

The only varying parameter in this capacitor is the distance between the two parallel plates which is the Split cut width (t). From capacitance general formula:

$$C = \frac{\varepsilon A}{t} \text{----------} (3.1)$$

Where ε= dielectric constant, A = area of the capacitor plate and t = Split cut width

As ε and A are constant $$C \propto \frac{1}{t} \text{----------} (3.2)$$

Also we know that $$f = \frac{1}{\sqrt{LC}} \text{--------} (3.3)$$

Where L = inductance, that remains nearly constant and f = frequency, thus

$$f^2 \propto t \text{---------} (3.4)$$

Therefore experimental results and simulations provided in this section agreed well with the analytical L-C resonance model of SRR in the literature [51, 52] which dictates that as the capacitance of system decrease the resonance frequency will increase.

3.2.2 Effect of the gap between rings

The proposed split ring resonator SRR structure composed two concentric rings with gap between them (***d***) showed in Figure 3.5. In this section we investigated the effect of this gap on the magnetic resonance frequency. The gap distance is varied ranging from 0.2 to 0.6 mm with 0.1 mm steps whereas all other geometrical parameters are kept constant. Geometrical parameters used in this section are: Split cut width (t) = 0.2 mm, metal width (w) = 0.8mm and radius of the inner ring (r) = 1.6mm.

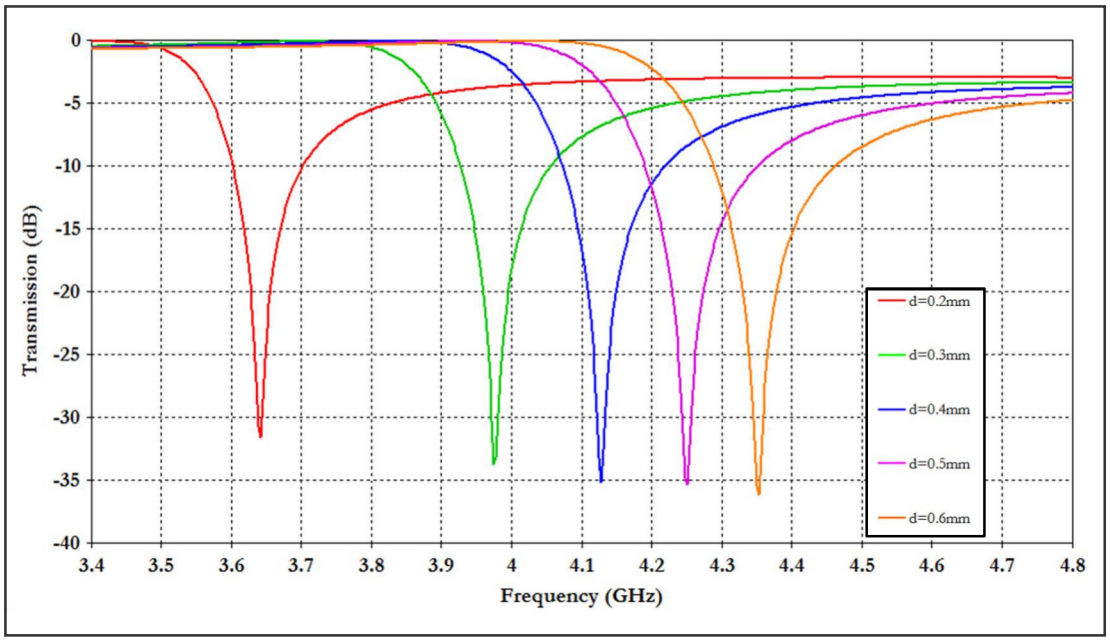

Figure (3.10): Simulated transmission spectrum of SRR structure with various gap distances *(d)*.

To keep the overall dimensions constant, the outer ring radius is kept constant (3.4mm). Thus increasing the gap distance will also decrease the size of the inner ring.

Figures 3.10 and 3.11 show the simulated and measured transmission (S21) respectively.

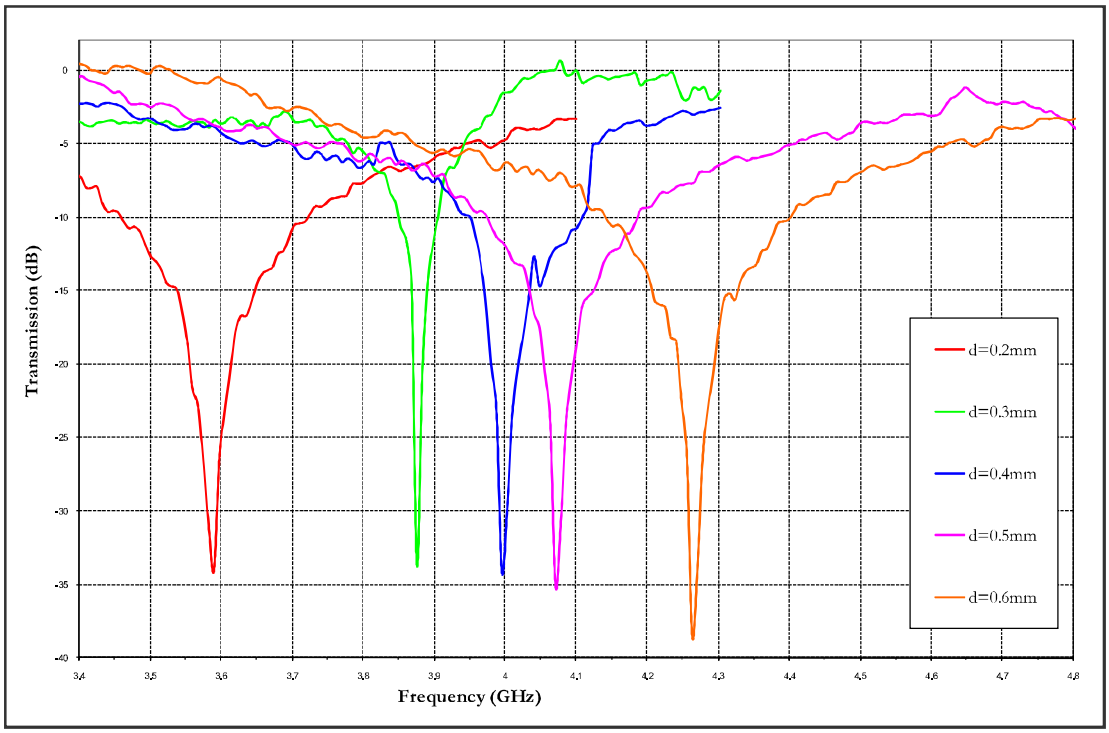

Figure (3.11): Measured transmission spectrum of SRR structure with various gap distances *(d)*.

These figures compare the transmission spectra of 5 SRRs with gap distances varied from 0.2 to 0.6 mm with 0.1 mm steps.

As can be seen in figures 3.10 and 3.11, the magnetic resonance shifted to higher frequencies when the gap distance *(d)* increased. Also results obtained both numerically and experimentally are in good agreement.

This resonant behaviour can be explained by an analytical model proposed by Sauivac et al [51]. In this model increasing the gap distance will decreases mutual inductance and mutual capacitance of the equivalent LC-circuit. By following eq. (3.4) above, we can conclude that the resonance frequency *(f)* proportional to the gap distance *(d)*.

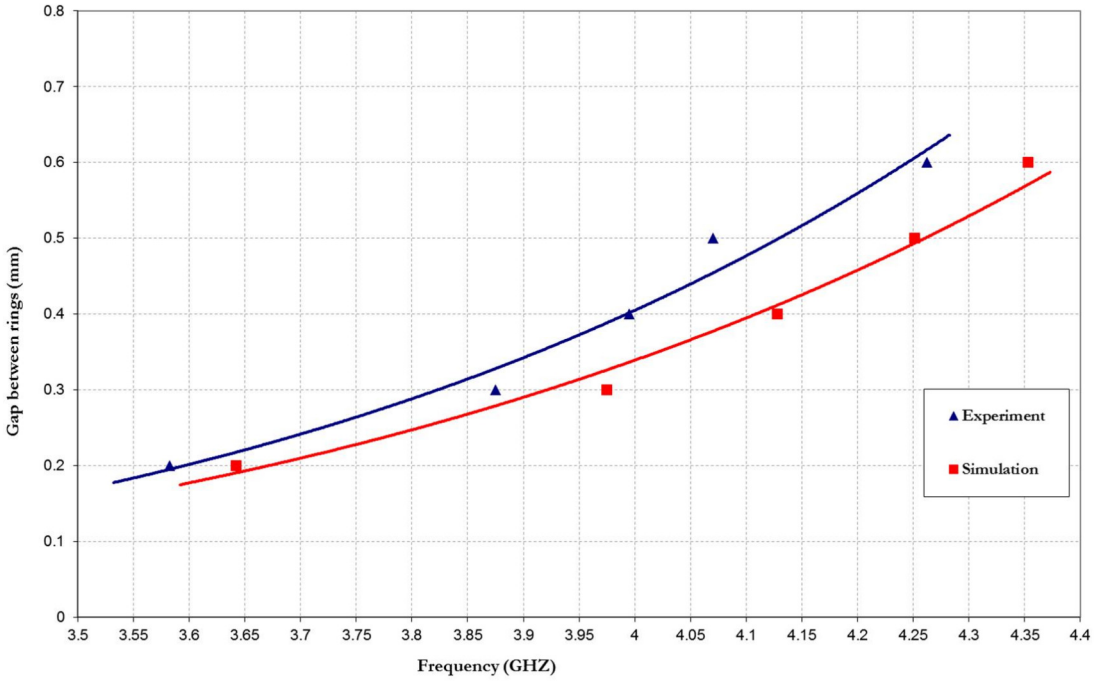

Figure (3.11a): Gap between rings vs. Resonance frequency for both experiment and simulation.

Figure 3.11a confirms that the resonance frequency shifted to a higher value when the gap between rings increased. The simulation values are higher than the measured one by a factor of around 0.1 GHz. The difference in these values can be attributed to many factors like noise in the measured result. However, as these differences are almost constant the reason for the shift in results most likely to be a constant parameter that has values in the simulation software differ from reality, example the permittivity of the FR4 base.

3.2.3 Effect of ring width

In this section we investigate the effect of ring width *(w)* on magnetic resonance frequency (see Figure 3.5). The ring width *(w)* is varied ranging from 0.4 to 1.0 mm with 0.2 mm steps whereas all other geometrical parameters are kept constant. Geometrical parameters used in this section are: Split cut width (*t*) = gap between them *(d)* = 0.2 mm, and radius of the inner ring (*r*) = 1.6mm.). To keep the overall dimensions constant, the

outer ring radius is kept constant (3.4mm). Thus increasing the ring width will also decrease the size of the inner ring. This means for narrower ring configurations, the inner ring is larger in diameter.

Figures 3.12 and 3.13 below show the simulated and measured transmission (S21) respectively. The (S21) of 4 SRRs with different ring width varied from 0.4 to 1.0 mm with 0.2 mm steps are compared in figures 12 and 13.

Once again, going back to Sauivac model where the ring width inversely proportional to mutual capacitance and mutual inductance [51]. This means the resonance frequency expected to shift to higher values as L and C decrease (equation 3.3) and the ring width increases.

The above statement agrees well with both simulations and experiment results reported in this section.

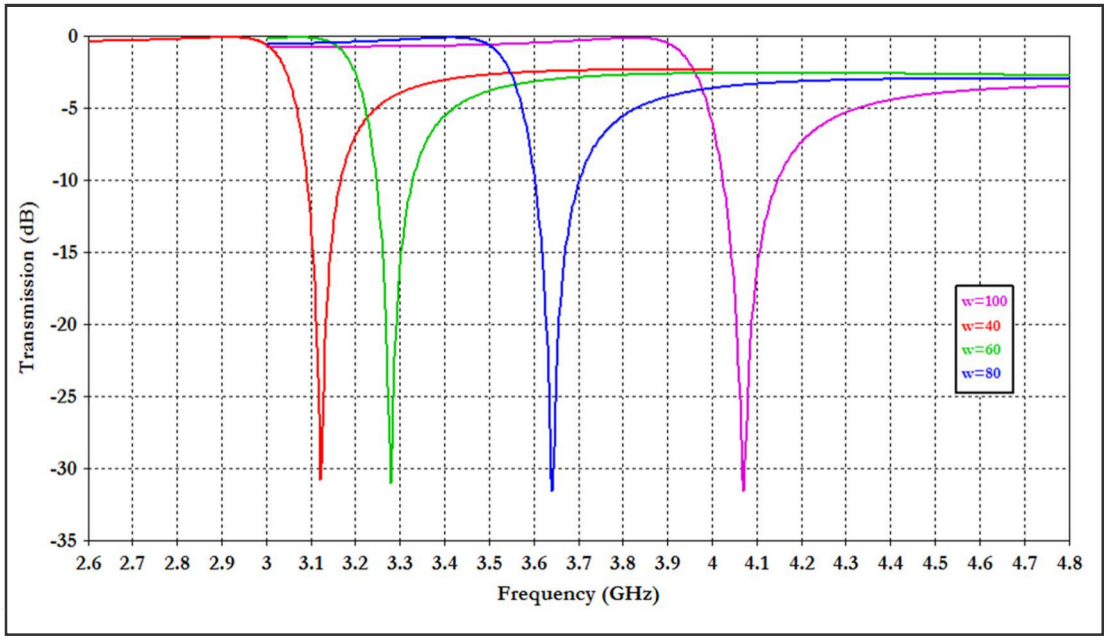

Figure (3.12): Simulated transmission spectrum of SRR structure with various ring width *(w)*.

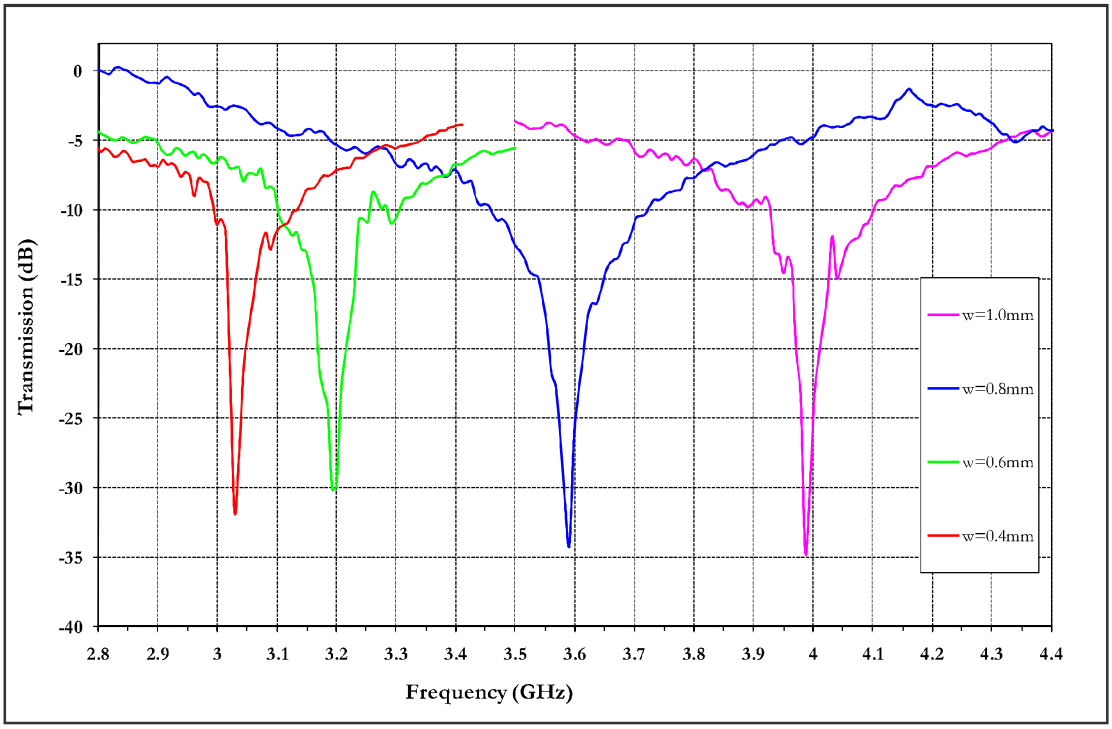

Figure (3.13): Measured transmission spectrum of SRR structure with various ring width *(w)*.

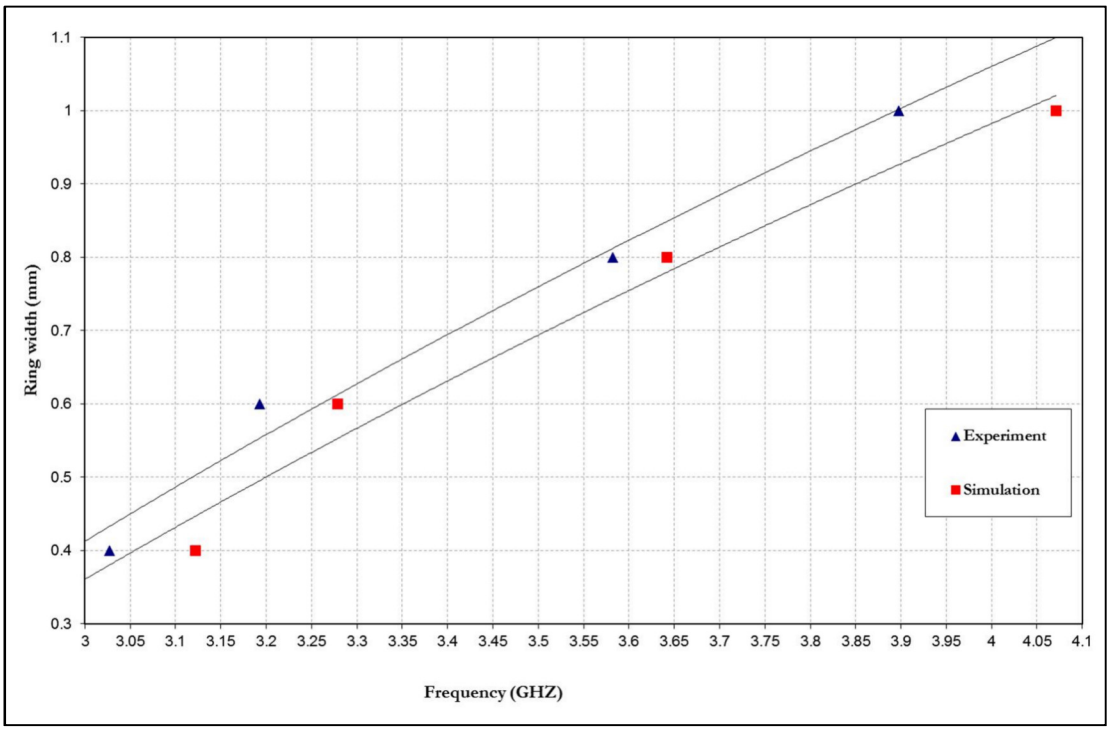

Figure (3.13a): Ring width vs. Resonance frequency for both experiment and simulation.

The experimental and simulation results are compared in figure 3.13a by taking the resonance frequency for each ring width for both simulation and measured values. Both results are in good match with a small shift in resonance frequency of about 0.1 GHz. This proves the statement on pervious section for the constant shift in the results that can be explained with the input parametric values on the CST software.

3.3 Effect of the base dielectric permittivity

In previous sections (3.2.1 -3.2.3) we use dielectric permittivity of $\epsilon = 4.0$ for both experiment and simulation which is the actual ϵ of the used FR4 substrate. However in this section we will investigate the effect of varying the dielectric permittivity analytically.

The initial geometrical parameters used in this section are: Split cut width (t) = gap between rings (d) = 0.2 mm, ring width (w) =0.8mm, radius of the inner ring (r) = 1.6mm and dielectric permittivity ϵ varied ranging from 3.8 to 4.6 with 0.2 steps.

In metamaterials the structures' dimensions are much smaller than the wavelength thus the effective medium solved using Maxwell equations for effective medium with effective permeability μ and effective permittivity ϵ. Therefore, dielectric permittivity of the substrate contributes to the value of the effective medium permittivity (SRR).

This means that when the dielectric permittivity of substrate increases, the effective permittivity of SRR medium increases. Also we know that the resonance frequency is inversely proportional to both permeability μ and permittivity ϵ. i.e. when the permittivity increases, the resonance frequency decrease.

Figure 3.14 below demonstrate that the transmission results (S21) shifted to higher frequency with lower dielectric permittivity.

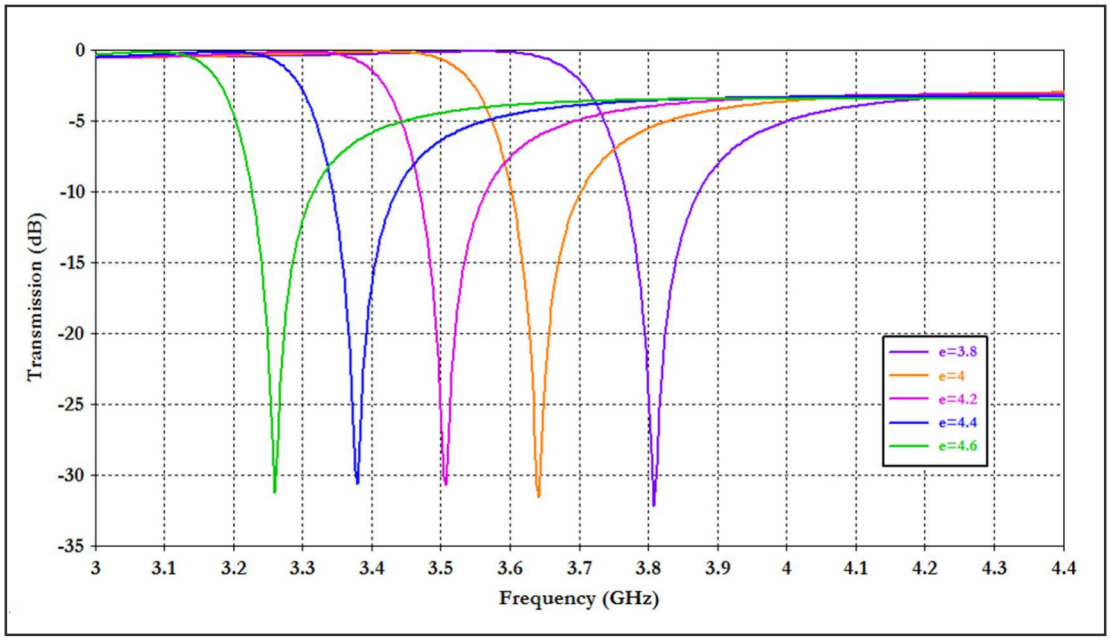

Figure (3.14): Simulated transmission spectrum of SRR structure with various dielectric permittivity ε.

The main reason behind investigating dielectric permittivity effect on the resonance frequency in this section and FR4 base thickness on the next section arise from the slight shift in resonance frequency between simulated and measured results in previous sections 3.2.1-3.2.3. Sections 3.3 and 3.4 proves that the resonance frequency changes when dielectric permittivity or base thickness changes. Comparisons between simulated and real measurement results was not possible at this stage as it is difficult to get PCB with different range of dielectric permittivity and thickness and the research was mainly focussed on processing standard PCB boards.

3.4 Effect of FR4 base thickness

The effect of s FR4 thickness on resonance frequency is investigated by varying the substrate thickness of a single SRR unit from 0.8 mm to 1.6 mm with 0.4 mm steps while keeping all other geometrical parameters constant.

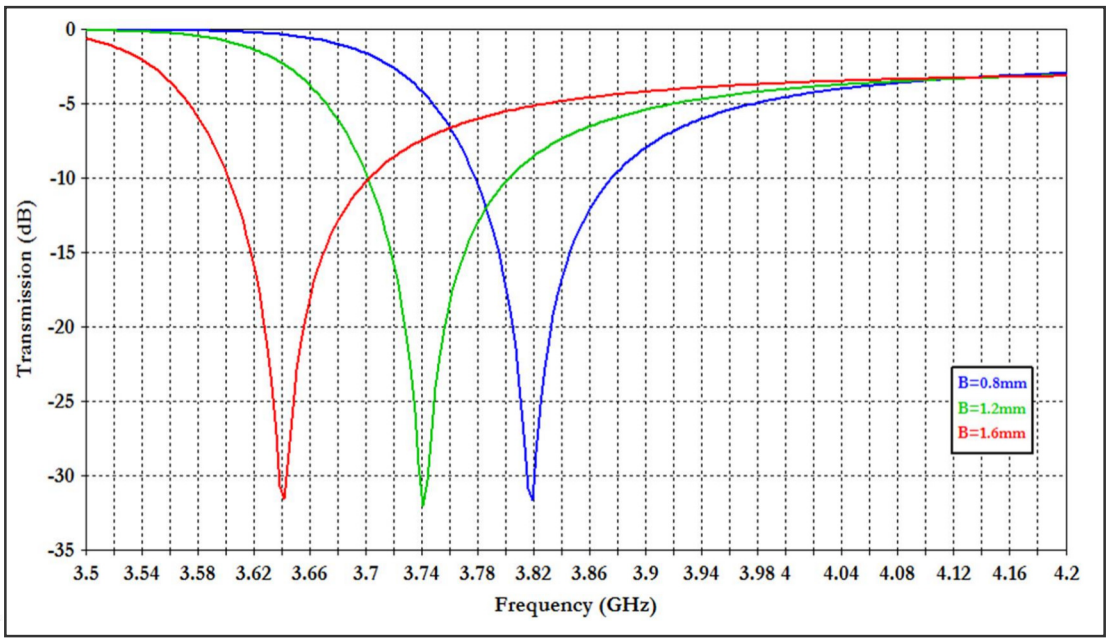

Figure (3.15): Simulated transmission spectrum (S21) of SRR structure with various FR4 base thickness.

The initial geometrical parameters used in this section are: Split cut width (*t*) = gap between rings *(d)* = 0.2 mm, ring width *(w)* =0.8mm, radius of the inner ring (*r*) = 1.6mm and dielectric permittivity ε=4.0.

As can be seen in Figure 3.15 above, increasing the substrate thickness decreases the resonance frequency of a single SRR unit.

The properties of the metamaterials medium are determined by the effective medium solved using Maxwell equations for effective permeability μ and effective permittivity ε. Therefore, increasing the dielectric base thickness will effectively increase the value of the effective permittivity of the medium (SRR).

3.5 Split Ring Resonators with different number of cuts

Conventional split ring resonator SRR and double ring resonator designs are based on a single split in the ring (rings in double resonator case) as illustrated in figure 3.5.

In this section the investigation explores the option of increasing the number of splits in each ring and the effect on the resonance frequency.

3.5.1 Conventional double SRR with different number of cuts

Split Ring Resonator structures with different number of splits will be investigated in this section. CST microwave studio simulation software is employed to measure the magnetic resonance of single SRR unit cell with two, four, six and eight cuts (splits). The double split ring resonator with two splits is the one that been investigated in previous sections (3.2 and 3.3) with the following parameters: Split cut width (*t*) = gap between rings *(d)* = 0.2 mm, ring width *(w)* =0.8mm, radius of the inner ring (*r*) = 1.6mm and dielectric permittivity of the FR4 base ϵ=4.0.

Figure 3.16 below show schematic drawings of the four SRRs used in this section with two, four, six and eight splits that were investigated.

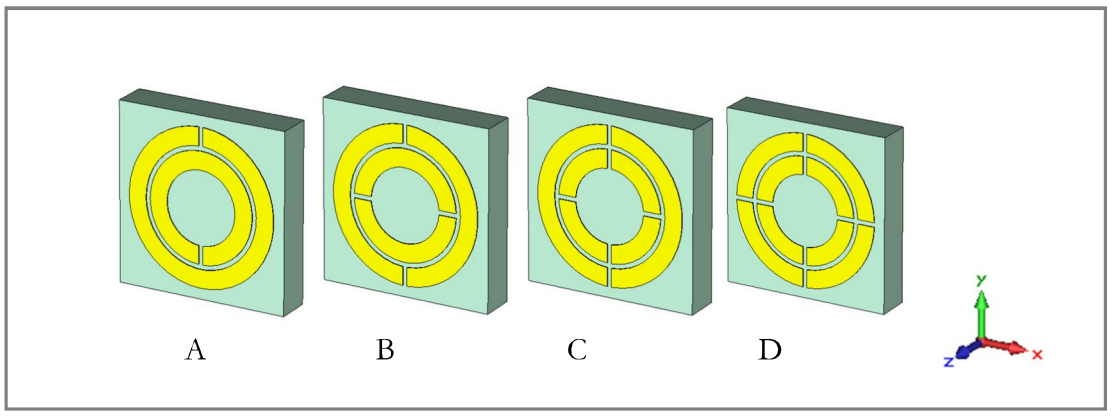

Figure (3.16): Schematics of SRR with: **A** 2 cuts. **B** 4 cuts, **C** 6 cuts and **D** 8 cuts.

The dimensions of all FR4 bases of each SRR unit cells are kept fixed to 7.75 mm x 7.75mm with thickness of 1.6mm. This also true for all previously investigated SRRs in this chapter.

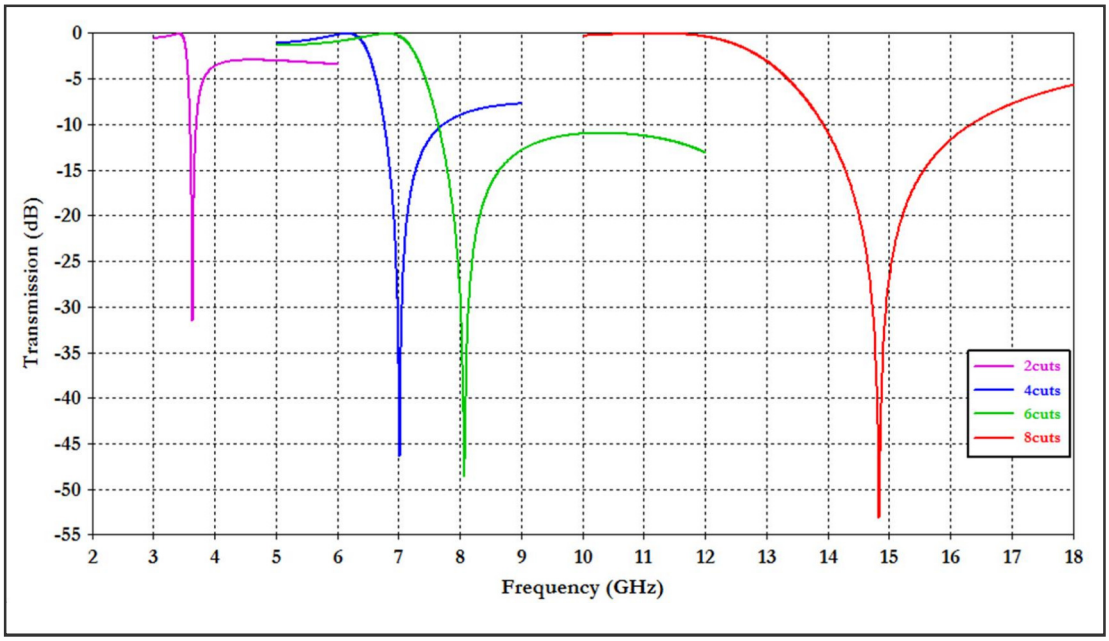

Figure (3.17): Simulated transmission spectrum (S21) of SRR structure with various numbers of splits.

The experimental results are shown in Figure 3.18 indicating that the resonance frequency of single SRR increases with additional splits.

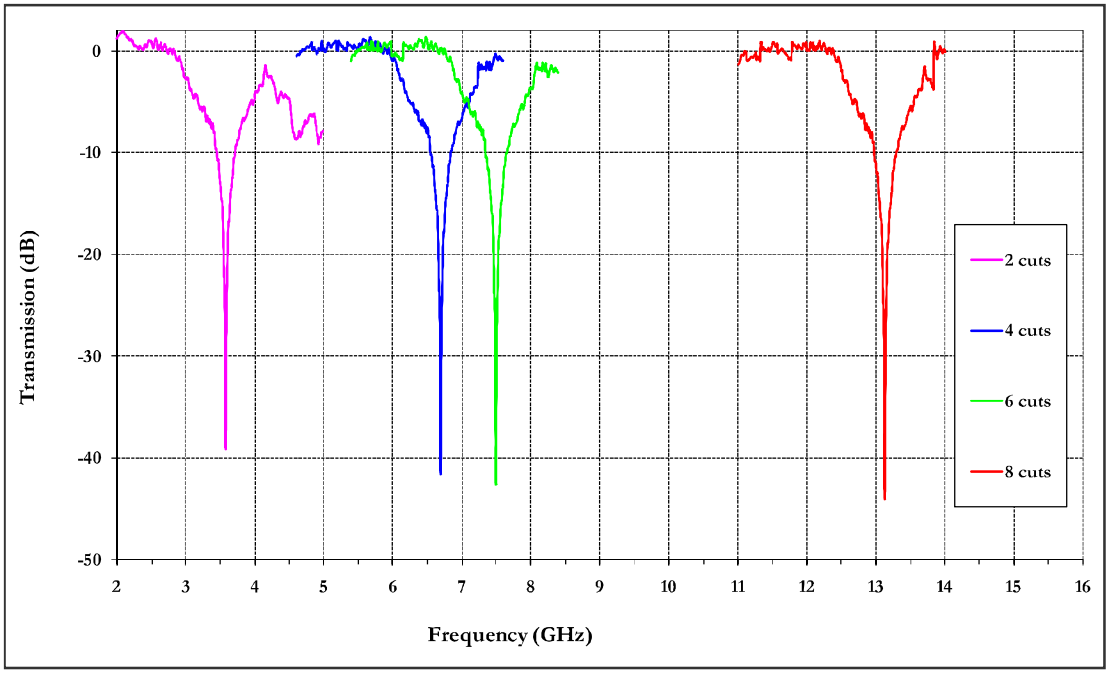

Figure (3.18): Measured transmission spectrum (S21) of SRR structure with various numbers of splits.

Also, simulation results in Figure 3.17 reveal that the additional cuts increase the resonance frequency of the single SRR structure which agrees well with the experimental results.

Adding additional cuts to the rings mean that additional capacitors are connected in series to the original capacitor (Figure 3.19). This leads to decrease the total capacitance of each ring in the SRR structure.

A simplified example can be considered, shown in Figure 3.19 below, to determine the total capacitance for each ring. Before adding the additional cuts the total capacitance for the outer ring equal to *C1*. The total capacitance is equal to *C1x C2/(C1+C2)* after adding one cut to the outer ring.

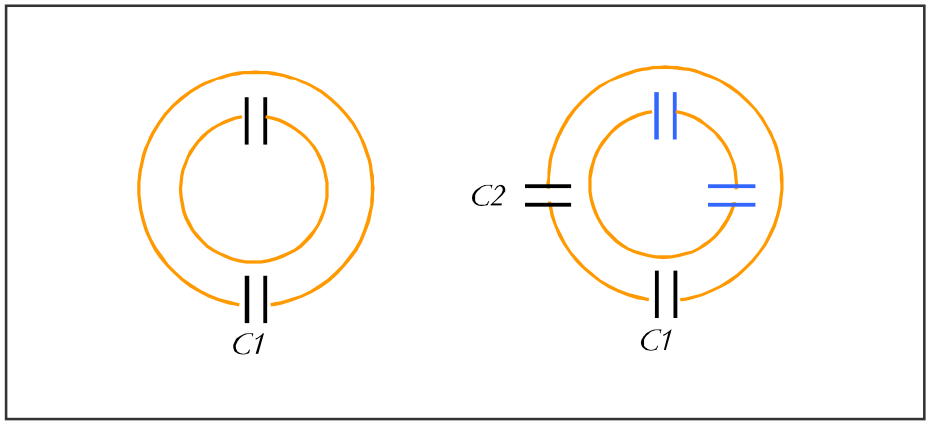

Figure (3.19): Schematic of SRR symbolize in capacitance circuit form.

As mentioned before in section 3.2.1 and using equation 3.3, the resonance frequency is inversely proportional to both capacitance and inductance of SRR structure. Therefore, the magnetic resonance frequency increases with the decreasing total capacitance:

$$f \propto \frac{1}{C} \propto \text{Number of splits (cuts)} \text{---------} (3.5)$$

3.5.2 Single Ring Resonators with different number of cuts

In this section we will investigate a single ring resonator structure with one, two and four splits. The single ring considered here is the same as the double ring SRR used in previous sections with only the inner ring removed. The double ring SRRs are composed of two concentric rings with splits oriented opposite to each other. The purpose of the inner ring of the SRR is to increase the total capacitance of the system and decrease the resonance frequency. It is expected to obtain magnetic resonance for this type of ring as there are capacitive element from the split/splits and inductive element from the metallic ring wire [55].

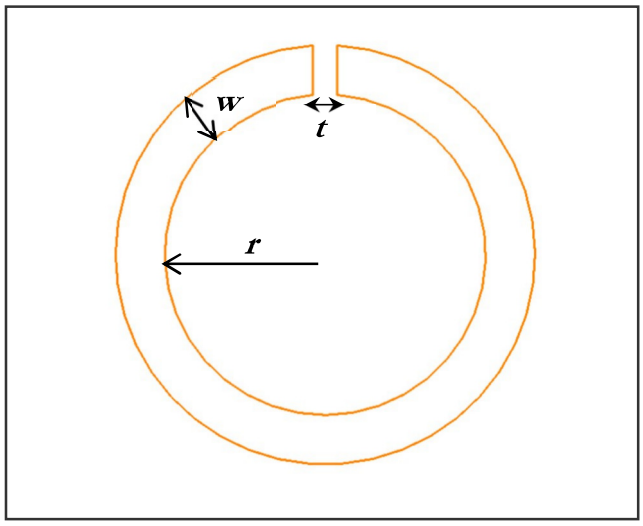

Figure (3.20): Schematics of single ring resonator.

The geometrical parameters of the single ring resonator are shown in Figure 3.20. The width of each split (t) is 0.2 mm, the width of the rings (w) is 0.8 mm, the inner radius of the ring (r) is 2.6 mm, and the thickness of the copper layer is 35 μm and the thickness of the FR-4 base 1.6 mm. The dimensions of the FR-4 base for all single rings unit cells is 7.75 x 7.75 mm and the thickness is 1.6 mm with dielectric permittivity constant $\varepsilon = 4.0$.

The magnetic resonance of single ring structures was investigated with one, two and four splits as depicted in Figure 3.21 below.

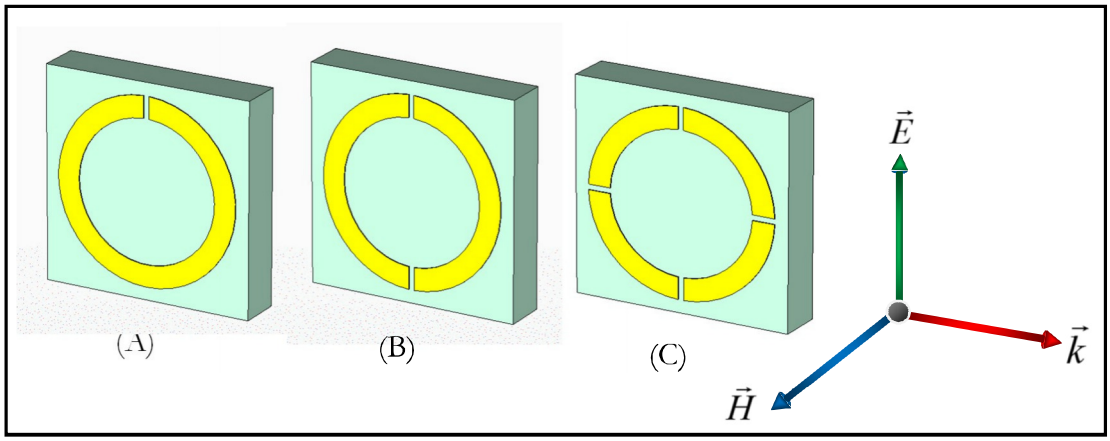

Figure (3.21): Schematics of single ring resonator with: (A) one split, (B) Two splits and (C) four splits.

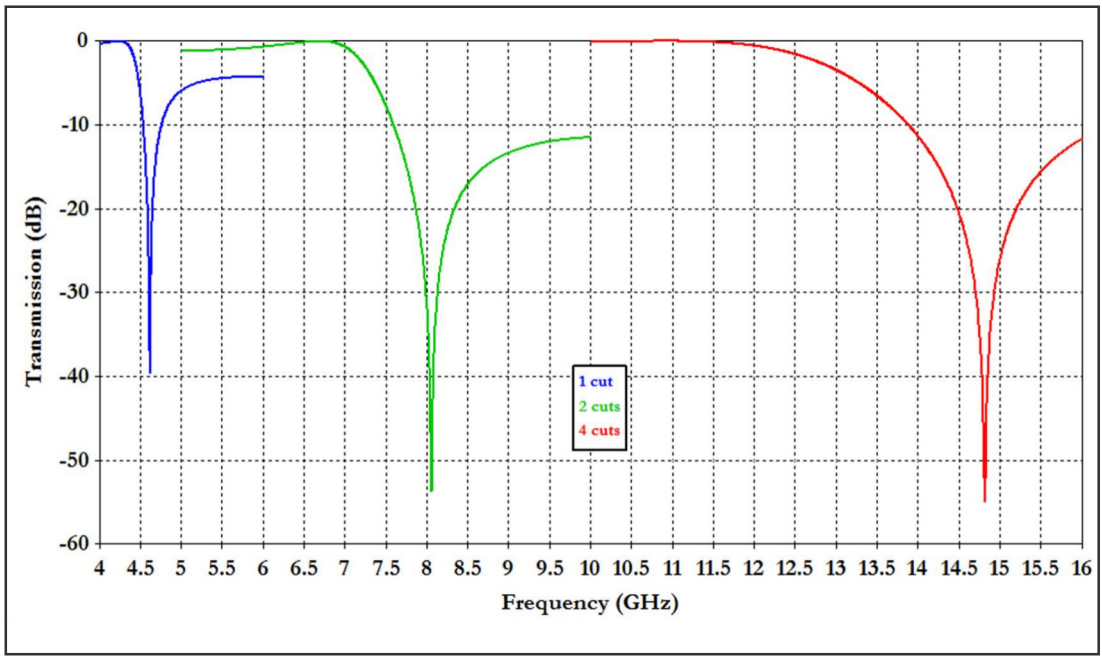

Figure (3.22): Simulated transmission spectrum (S21) of single ring resonator structure with various numbers of splits.

The transmission spectrum (S21) of the three single rings resonators is plotted against the frequency in Figure 3.22.

As can be seen in numerical results, the magnetic resonance frequency of single split, two split and four split structures are 4.6 GHz, 8.1 GHz and 14.8 GHz respectively.

As mentioned in the previous section, additional cuts will shift the resonance frequency to a higher value. As the resonance frequency is inversely proportional to both the capacitance add inductance of the system (single ring structure), the magnetic resonance frequency increases with the decreasing total capacitance or:

$$f \propto \frac{1}{C} \propto \text{Number of splits (cuts)} \text{---------} (3.5)$$

3.6 Effect of electromagnetic field polarizations on the SRRs electromagnetic resonance

In this section, the transmission properties of a single SRR resonator are simulated for different electromagnetic field polarizations and propagation directions. Four possible orientations of SRR structures are considered in this section depicted in Figure 3.23 below.

The split ring resonator with type "A" configuration is the one that has been investigated in previous sections (3.2.1-3.5.1) with the following parameters: Split cut width (*t*) = gap between rings *(d)* = 0.2 mm, ring width *(w)* =0.8mm, radius of the inner ring (*r*) = 1.6mm and dielectric permittivity of the FR4 base ε = 4.0.

The four SRRs can be classified into two groups according to the electric field (E) and the magnetic field (H) directions with respect to the SRRs. The first group include SRRs *A* and *B* type configurations will be designated "H-coupled SRRs" or "parallel oriented SRRs".

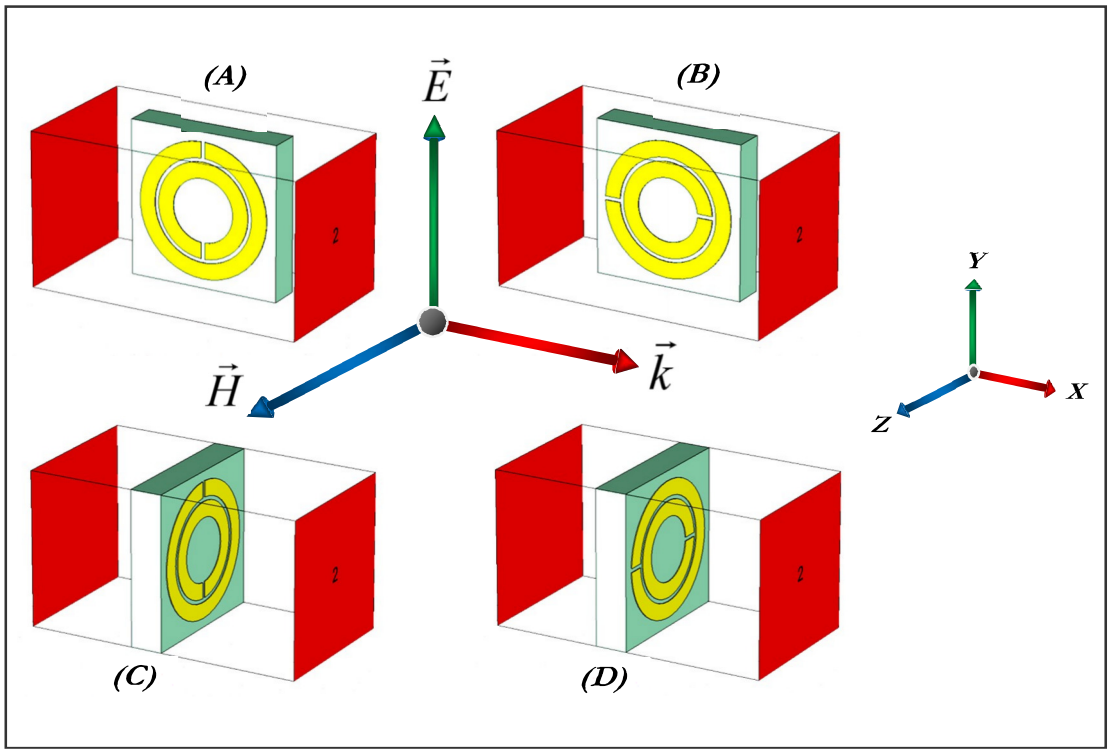

Figure (3.23): The four studied orientations of the single SRR unit cell with respect to K, E and H coordinate of the incident electromagnetic wave.

In this group the magnetic field vector (H) is perpendicular to the SRR plane causing the magnetic excitation of the rings and the magnetic resonance is expected to take place at certain frequency as can be seen in previous sections in this chapter. Also, this group can be called parallel oriented as the electromagnetic wave propagation direction is parallel to the plane of the SRR structure.

On the other hand, the second group include SRRs *C* and *D* type configurations will be designated "E-coupled SRRs" or "perpendicular oriented SRRs". In this case, the magnetic field vector (H) of the incident electromagnetic wave is parallel to the rings leaving these types of SRRs with no magnetic excitation. Meanwhile, the electric field vector (E) of the incident wave is effective on these types of configuration SRR structure. Moreover, as the electromagnetic wave propagates in a direction perpendicular to the plane of the SRR structure; this group can be called perpendicular oriented.

CST microwave studio software is used to perform the theoretical simulation. Open boundary conditions are employed along the propagation direction (K); electric boundary conditions are polarized in (E) direction and magnetic boundary aligned in (H) condition showed in Figure 3.23. The transmission spectrum (S21) of the four SRRs orientations plotted against the frequency in Figure 3.24.

SRR type-A configuration is the conventional case used throughout this chapter and positioned in the X-Y plane with the incident electromagnetic wave propagating along the X-direction. The magnetic field vector (H) is perpendicular to the SRR plane and the electric field vector (E) parallel to the symmetry axis of the SRR [56]. The magnetic resonance exists as expected since the magnetic field (H) is perpendicular to SRR type-A plane.

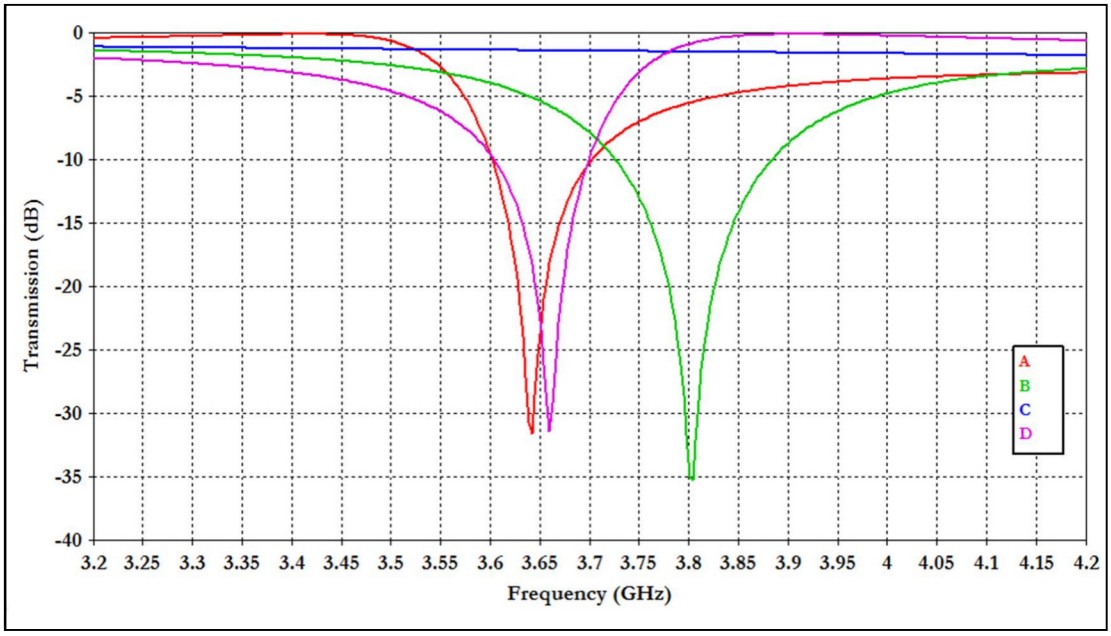

Figure (3.24): Simulated transmission spectrum (S21) of SRRs structures with four different orientations.

SRR type-B located at X-Y plane too. The incident electromagnetic wave propagates along X-direction, with magnetic field vector (H) and electric field vector (E) along the Z

and Y directions respectively. Similarly to type-A SRR, the magnetic field is perpendicular to the structure plane, hence the magnetic resonance exists. However, the split rings geometry is symmetrical in the E-k plane, so there is electrical resonance as well in the SRR type-B [56].

Therefore, the resonance of type-B SRR is stronger than type-A SRR orientation and thus the dip value of type-A SRR structure is lower dip value as can be seen in Figure 3.24.

This means the SRR of type-B is excited both magnetically and electrically making it the strongest resonator among all the orientations considered as the electrical and magnetic resonances work constructively.

SRR type-C oriented in the Y-Z plane with incident electromagnetic wave propagates along X- direction. The magnetic field vector (H) and the electric field vector (E) polarised along Z and Y directions respectively. The magnetic field, in this case, is parallel to the SRR plane and therefore, there is no magnetic resonance. Also, the electric coupling does not occur as the electric field vector (E) is parallel to the symmetry axis of this type of SRR structure. In other words, as can be seen in Figure 3.32, type-C SRR structure is a mirror symmetric structure which prevents the electrical coupling to the resonance of SRR [56].

SRR type-D is 90^0 rotated version of type-C SRR orientation, the incident electromagnetic wave propagates along X- direction, with magnetic field vector (H) and electric field vector (E) polarised along Z and Y directions respectively. For this configuration, similar to the type-C SRR, the magnetic field is parallel to the SRR plane and magnetic resonance is unexpected. However, electric excitation is expected similar to type-B SRR which couples to the magnetic resonance of these SRRs. The electric effect

on type-B and type-D SRRs can be explained by considering the metallic ring structure of these SRRs acts like discontinuous wires for incident electric field vector (E) and gets excited electrically which in turn generates magnetic resonance [56] as can be seen in Figure 3.24.

3.7 Discussion

SRR is a resonant unit cell with both capacitance and inductance, the capacitance is more effectively introduced because capacitance can arise from the gap between the two rings in addition to the two cuts of each individual ring, while inductance that has one turn only is comparably weak

For LC resonant circuits with a given resistance, the higher the capacitance compared to inductance the narrower the bandwidth. In terms of the quality factor or Q factor the higher the Q, the narrower and sharper the peak is. For this reason all measured and simulated results in this chapter have narrow bandwidth while the result on chapter four for the bulk SRR have much wider bandwidth as the bulk equivalent capacitance is reduced.

Another factor to consider in this part of the research is the depth of resonance which in microwave and antenna point of view; the steeper the resonance the better the device. The main purpose of this chapter was to investigate the effect of single unit cell physical geometrical parameters on the resonance frequency. However, in some cases the depth of the resonance has been slightly changed. The reason for this is that the band width was very narrow even when preforming the transmission measurements in small scanning steps (0.0075 GHz). Near the resonance frequency, each step in frequency may change the depth by about 10-15 dB. That leads to a conclusion that the resonance frequency may falls between two steps and gives depth error of around 15 dB.

3.8 Summary

Split Ring Resonator (SRR) is the base metamaterial unit cell considered in this project. The design had been modified for ease of fabrication and calculations with CST microwave studio simulation software that can calculate the expected resonance frequency.

The fundamental electromagnetic resonance mechanisms of Split Ring Resonators (SRR) had been explored in terms of the relationship of the physical shape of a SRR on its electromagnetic resonance frequency. The single unit cells (SRR) described in this chapter will form the base to build metamaterial blocks presented in chapter four.

The magnetic resonance frequency of the SRR measured experimentally and theoretically for each SRRs shape geometrical dimensions variation. The investigation in this chapter includes the following parameters; split cut width, gap between rings, ring width, base dielectric permittivity and base thickness. Additionally, the effect of electromagnetic field polarisation on the SRRs electromagnetic resonance had been also investigated in this chapter.

CST Microwave Studio® software is employed for the numerical simulations to determine the resonance frequency for each case. These results were used to estimate the resonance frequency for the experimental measurements to narrow the actual measurement time and frequency sweep band.

Appendix 3.1: Unit cell size validation

Mostly the open ring resonator can be considered as an LC circuit where the capacitance can described by the usual textbook formula.

For a large capacitor with the separation between the plates is small compared to the dimensions of the plates, to ensure a uniform distribution of the field over plate's area:

$C \propto$ plate area/distance

And the inductance by the formula for a coil with N windings:

$L \propto$ coil area/length (for N = 1)

For simplicity, we can consider the width of the metal is equal to the distance between the capacitor plates (t)

$C = \varepsilon_o \varepsilon_c \, t \, d / t$ where:

ε_c = the effective permittivity of the material in between the plates and

d = the metal thickness

$L = \mu_o \pi r^2 / d$ where:

r = radius of the coil

LC-resonance frequency:

$$\omega_{LC} = 1/\sqrt{LC} = \frac{1}{r\sqrt{\pi}} \frac{1}{\sqrt{\varepsilon_c}} \frac{1}{\sqrt{\varepsilon_0 \mu_0}} = \frac{1}{r\sqrt{\pi}} \frac{c}{\sqrt{\varepsilon_c}}$$

Where c = speed of light = $\frac{1}{\sqrt{\varepsilon_0 \mu_0}}$

And the LC-resonance wavelength

$$\lambda_{LC} = \frac{2\pi c}{\omega_{LC}} = 2\pi\sqrt{\pi}\sqrt{\varepsilon_c}\, r$$

For relevant parameters $\varepsilon_c \approx 4$ this yield $\lambda_{LC} \approx 10 \times 2r$.

Thus, for microwave wavelength of $\lambda \approx 1$mm, the linear dimension of the coil would need to be on the order of $w = 100$ μm, implying minimum feature sizes around 50μ.

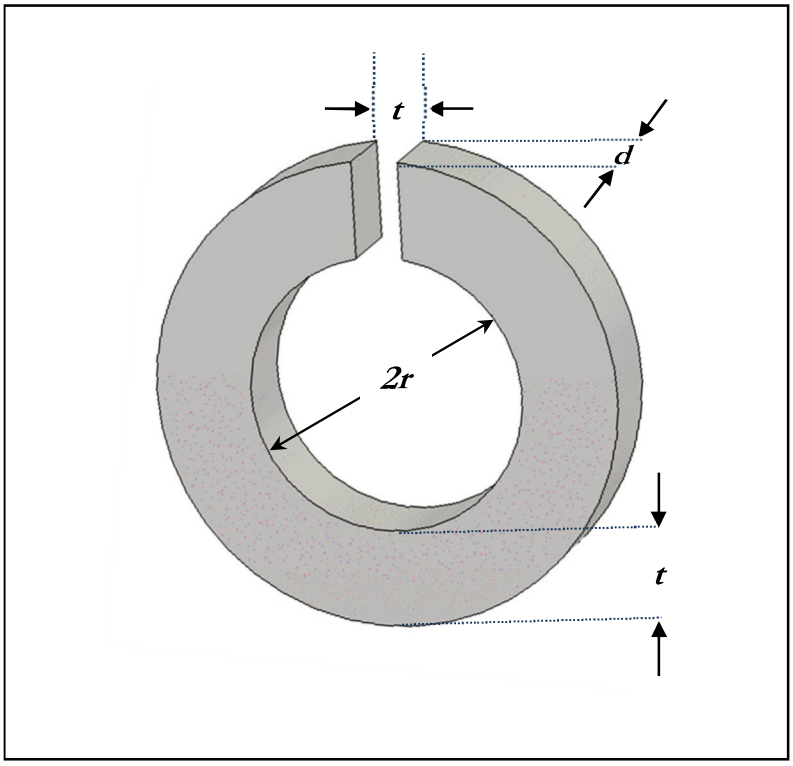

Figure shows the schematics of the elementary unit cell.

Chapter 4

Double Negative Metamaterials

4.1 Introduction

Metamaterials appeared to have unattainable properties from ordinary materials, as Veselago pointed out, substances with negative magnetic permeability ($\mu<0$) could not seemingly be achieved at that time. However the work opened the possibility to consider both negative permittivity and permeability materials, introducing a new classification of materials according to their permeability (μ) and permittivity (ε) as illustrated in figure 4.1.

Because of the lack of any experimental evidence this theory remained as a mere prediction, until Pendry *et.al* [1] proposed structures that can exhibit negative permittivity at a certain frequency. This artificial material consists of an array of split-ring resonators (SRR) and thin wires.

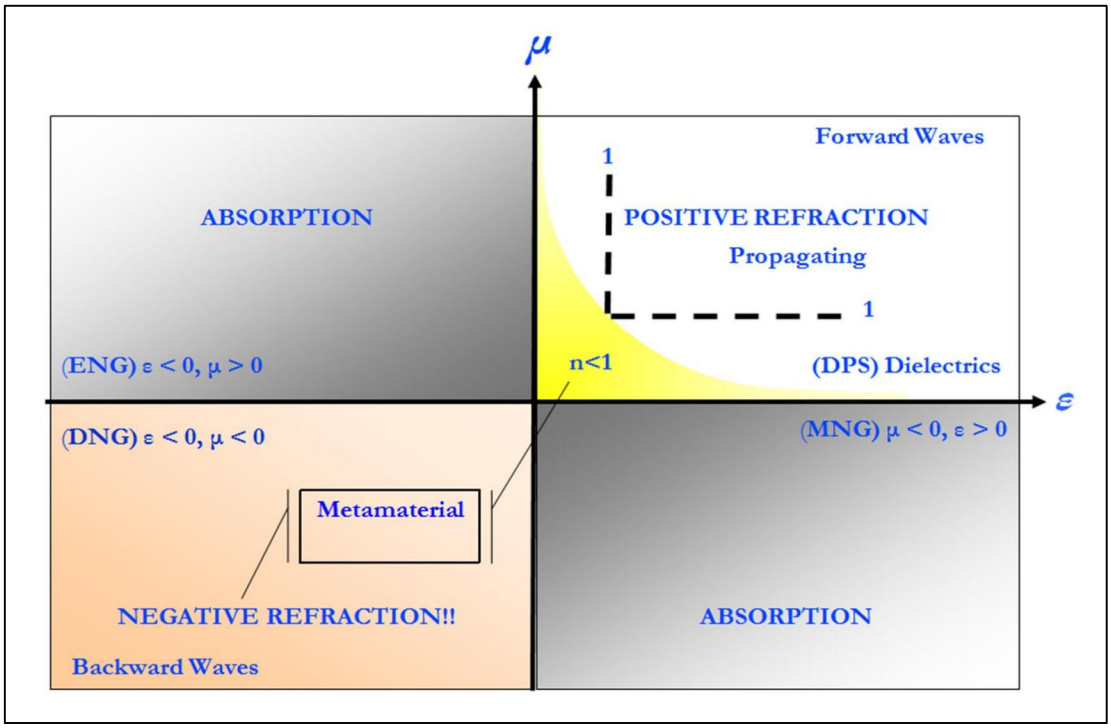

Figure (4.1): Material classifications according to their permittivity and permeability values.

He showed theoretically that an open ring could provide a negative permeability when the magnetic field component of the EM wave is perpendicular to the ring plane. In the same paper, he showed that a periodic array of wires and rings could create a structure with a negative index of refraction [1].

The analogy is as follows: Natural materials are made of atoms, which are dipoles. These dipoles modify the light velocity by the refractive index factor (n). The ring and wire units play the role of atomic dipoles. The thin wire acts as a ferroelectric atom that exhibits negative permittivity (ε). While the ring can be considered as a LC circuit; the ring wire acts as an inductor (L) and the open section of the spit ring acts as a capacitor (C). When the electromagnetic field passes through the ring, an induced current is created and the generated field is perpendicular to the magnetic field of the incident EM wave. As there is a magnetic resonance in the system, the permeability is negative, and the index of refraction is negative too.

Based on this concept Shelby et al [57] designed periodic structures with split-ring resonators and wire strips with both, negative permittivity and permeability. Smith et al [5] took the first steps to realise this novel type of material and left-handed propagation was observed in a narrow frequency band. Composite metamaterials with both negative dielectric permittivity and magnetic permeability were experimentally verified to have negative index of refraction by Shelby et al, [58]. Soon after, left-handed metamaterials with negative index of refraction were successfully demonstrated by various groups [59, 60] and this led to a great increase in interest in the investigation of metamaterials, their properties, methods of realisations and applications.

In this chapter, the transmission and refraction properties of metamaterials comprised of split-ring resonator and wire arrays and prove the backward propagation of microwave signal are investigated.

4.2 Classification of materials

It is well known that the response of a system to the presence of an electromagnetic field is determined by the macroscopic parameters permittivity ε and permeability μ.

Thus, generally, materials can be classified according to their dielectric permittivity and magnetic permeability values (Figure 4.1).

In the first quarter, figure 4.1, both the permittivity and permeability are greater than zero ($\varepsilon > 0$, $\mu > 0$). Most naturally occurring media have both permittivity and permeability greater than one and can be termed as Double-Positive medium (DPS). As the index of refraction has a positive value, the phase velocity will move forward under the right hand rule. Also, under this region, there is interesting area where $1 > \mu > 0$ which can be considered as a metamaterial (yellow area in Figure 4.1). The cloaking device realisation is based on metamaterials that fall in this region (yellow), this will be explained in more detail in chapter 5.

The second quarter (top left in Figure 4.1), has a medium with permittivity less than zero and permeability greater than zero ($\varepsilon < 0$, $\mu > 0$), designated an epsilon-negative (ENG) medium. Typically, metals under optical-UV frequencies exhibit this attribute [61].

In the third quarter (bottom left in Figure 4.1), both permittivity and permeability are less than zero ($\varepsilon < 0$, $\mu < 0$) and so designated a Double Negative medium (DNG) or Left-Handed Media (LHM). To date, this class of materials has only been demonstrated with artificial constructs.

Finally, bottom right in figure 4.1 is a medium with the permittivity greater than zero and permeability less than zero ($\varepsilon > 0$, $\mu < 0$), designated a Mu-Negative Medium (MNG). In certain frequency regimes some gyrotropic materials exhibit this characteristic.

4.2.1 Wave propagation according to unit cell size

The evenly distributed sub-wavelength meta-atoms in metamaterial make the whole medium macroscopically uniform. For this reason metamaterials are classified as a type of material instead of a device. To understand the wave material interactions, mediums are classified according to their unit cell size compared to the incident wavelength in this section.

The electromagnetic spectrum can be broadly segmented into three regions compared to unit cell dimension (a) showed in figure 4.2 below;

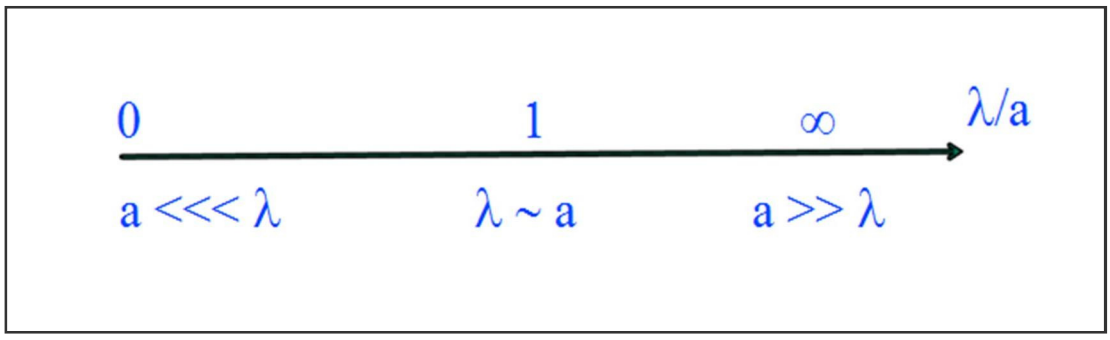

Figure (4.2): Unit cell size compared to wavelength for corresponding resonance frequency.

The first region, where the unit cell size is much smaller than the wavelength of interest, an effective medium description is employed using Maxwell equations with a uniform μ and ε based on the structures of the unit cells, an example of which is artificial metamaterials.

The second region (middle), when the scale of the unit cell is of the order of a wavelength, the response of the structure is dominated by diffraction and interference effects. Phenomena in this category occur across nearly the entire electromagnetic spectrum, including crystals in X-ray diffraction and photonic crystals in optics. The most well-known example in this region is Young's single and double slit experiments where the slit width is of the order of the incident wavelength.

With even larger unit cell sizes, the response of structures is usually described using geometrical optics and ray tracing. Example for this region can be found in our daily life e.g. shadows and lens systems.

4.3 Defining Left-Handed Materials (LHM)

To understand the concept of a left handed metamaterial we first restate the established right hand rule in electromagnetism. It states that when the direction of the magnetic field $\vec{H}$ and the electric field $\vec{E}$ are perpendicular to each other and represented by the index finger and thumb of the right hand respectively, then the middle finger gives the direction of propagation of the wave $\vec{K}$, which is normal to both other fingers (Figure 4.3). Mathematically, this rule can be represented as in the following equation:

$$\vec{S} = \frac{c}{4\pi}[\vec{E} \times \vec{H}] \text{---------} (4.1)$$

Where $\vec{S}$ is the Poynting vector, $\vec{E}$ is the electric field and $\vec{H}$ is the magnetic field. Also in this case $\vec{S}$ is the same as $\vec{K}$ the direction of propagation of the wave.

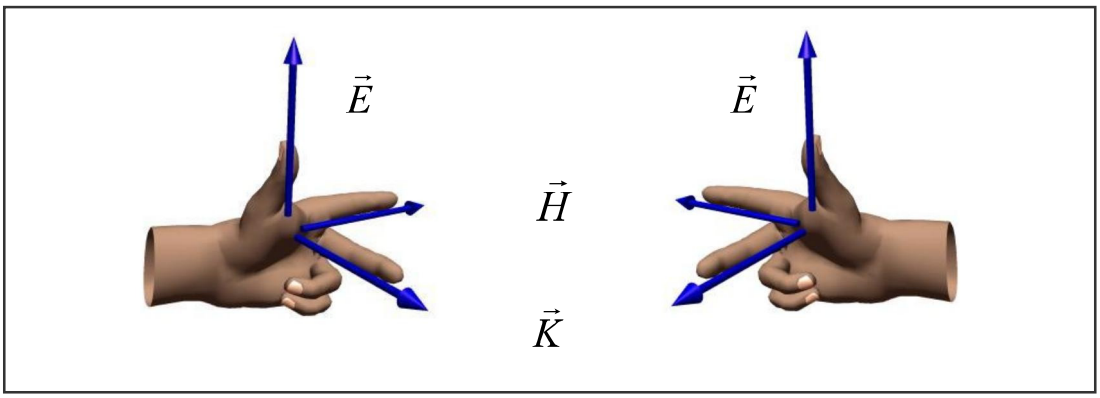

Figure (4.3): Left hand rule compared to original right hand rule.

The Maxwell's equations that describe the electromagnetic wave with respect to electric and magnetic field are:

$$\vec{k} \times \vec{E} = \frac{\omega}{c} \mu \vec{H} \quad \text{--------(4.2)}$$

$$\vec{k} \times \vec{H} = -\frac{\omega}{c} \varepsilon \vec{E} \quad \text{--------(4.3)}$$

Where $\vec{K}$ is the wave vector along the direction of the phase velocity.

In the previously mentioned case where the medium exhibits both negative permittivity and permeability, the phase velocity will be anti-parallel to the direction of wave propagation or energy flow. It can be said that the wave has a 'negative phase velocity' in that medium (Figure 4.4).

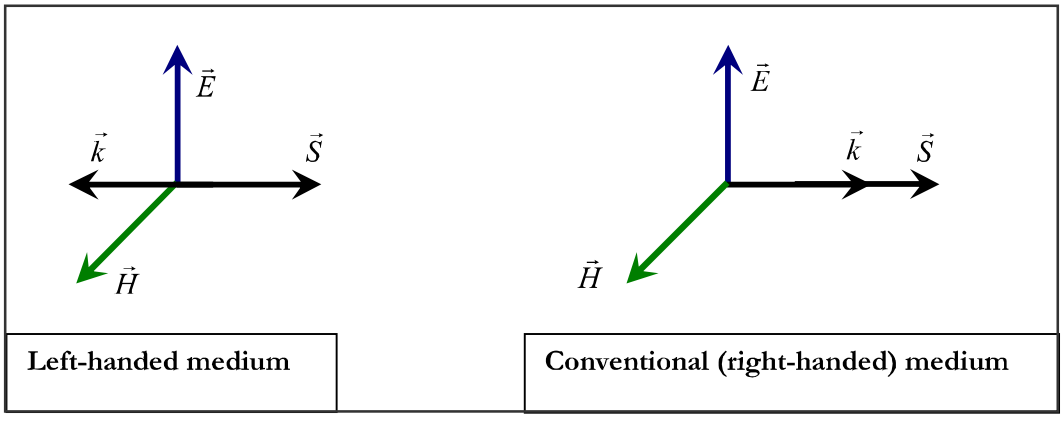

Figure (4.4): The wave propagation in a right-handed and left handed medium

Hence, although, the direction of energy flow is always from the sender to the receiver, the phase moves in the opposite direction.

Here the S vector follows the right hand rule, while the k vector is anti-parallel to the S vector.

Next is to define the refractive index for this left handed medium when both permittivity and permeability are negative. The refractive index of a material is defined by the square root of the product of the permittivity and permeability:

$$n = \pm\sqrt{\varepsilon\,\mu} \quad \text{--------} \quad (4.4)$$

Where n = refractive index, μ = magnetic permeability and ε = dielectric permittivity.

Apparently, the negative permeability and permittivity will not cause the refractive index to be negative. However, the typical choice of the refractive index in this case can be considered to be the negative square root of the product. Ziolkowski [62] proved that the index of refraction taking the negative value of the square root is mathematically correct when both permeability and permittivity are negative.

The energy flux can be determined by the Poynting vector:

$$\vec{S} = \frac{c}{4\pi}\left[\vec{E} \times \vec{H}\right] \quad \text{--------} \quad (4.5)$$

According to Veselago [3], the Poynting vector [S] always forms a right handed set of vectors with the electric [E] and magnetic [H] field. Also [S] and [K] are in the same direction for a medium with positive index of refraction and opposite to each other for a medium with negative index of refraction.

Based on Snell's law a wave travels in a medium with negative index of refraction bends to the same side of the normal as the incident ray (Figure 4.5).

Veselago predicted that it was essential for the medium to have both permeability and permittivity negative to be considered a Left Handed Metamaterial. However, research in 2006 by Enghetal [63] has considered materials with only one of these parameters having a negative value. These materials are described as single negative materials (SNG) with ε negative (ENG) or μ negative (MNG) (Figure 4.1). Also in the same research a material with ε near zero and μ near zero are identified as (ENZ) and (MNZ) respectively. These materials have been proven to have similar properties to the Left Handed Metamaterial and have great interest especially in constructing cloaking devices.

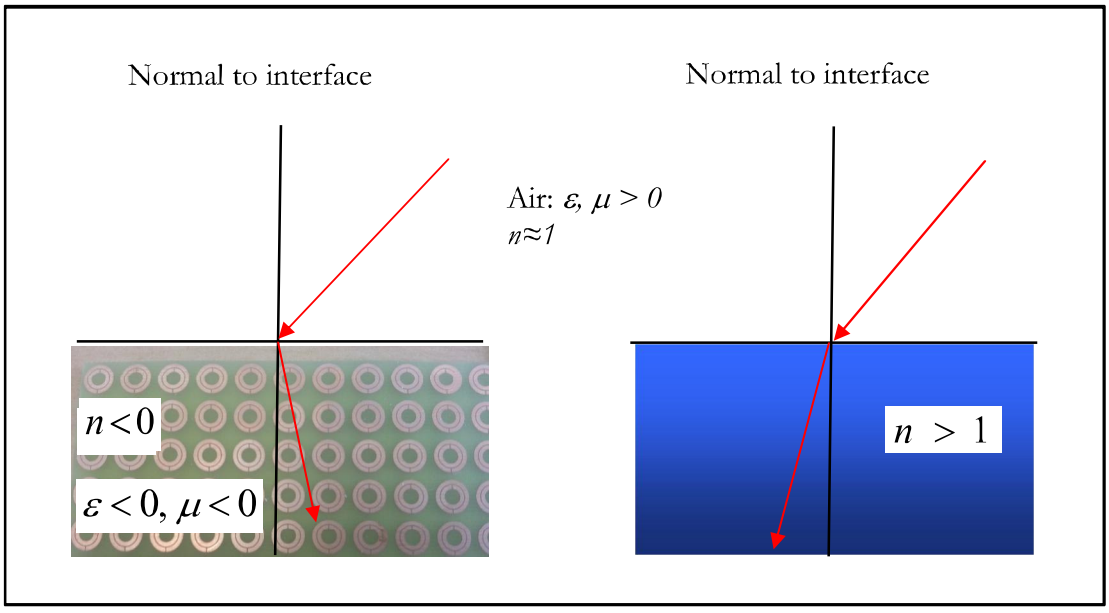

Figure (4.5): Refraction through LHM (left) and conventional right-handed medium (right).

4.4 Realisations of Left- Handed Materials

Metamaterials are artificial materials realised by embedding periodic metallic structures in dielectric substrates. These complex structures regulate the effective permittivity and

permeability of the bulk composite medium to negative values at certain frequencies. Metamaterials are dispersive in nature, which is why they are left-handed only in a certain range of frequencies.

Left-Handed materials were first realized by Smith et al [5] by creating a periodic array of interspaced conducting split ring resonators (SRR) and continuous wires. The bulk medium exhibited negative effective permeability μ_{eff} and permittivity ε_{eff} simultaneously.

The conducting SRR can modify the permeability of the host substrate to give a frequency dependent negative effective permeability μ_{eff}. While frequency dependent negative epsilon ε_{eff} is achieved by constructing a mesh of conducting thin wires [1].

Both structures combined form a mesh of alternative interspaced SRR and wire strips. The bulk medium possesses frequency dependent negative effective parameters (negative permeability and permittivity) [5]. This medium gives uniform alteration of the properties of the base dielectric material if the size of the unit cell of these periodic structures is considerably smaller than the considered wavelength [Appendix 3.1].

An analogy could easily be established for these effective media; any conventional material is a composite of periodic arrays of atoms or molecules. Long wavelengths are blind to such small atoms and hence the periodic structures appear to the wave as a homogeneous medium.

This phenomenon occurs under the condition that there has to be a constraint on the unit cell dimension that would make it appear homogeneous to the wave under consideration. Similarly, with metamaterials, the meta-atoms are much smaller than the operating wavelength and thus the medium can be described with effective permittivity and permeability [1].

Figure 4.6 below gives a generic view of metamaterials made with periodic SRR and thin wires. Wire strips and SRR will be briefly discussed and examined in detail to understand their contributions to the composite medium.

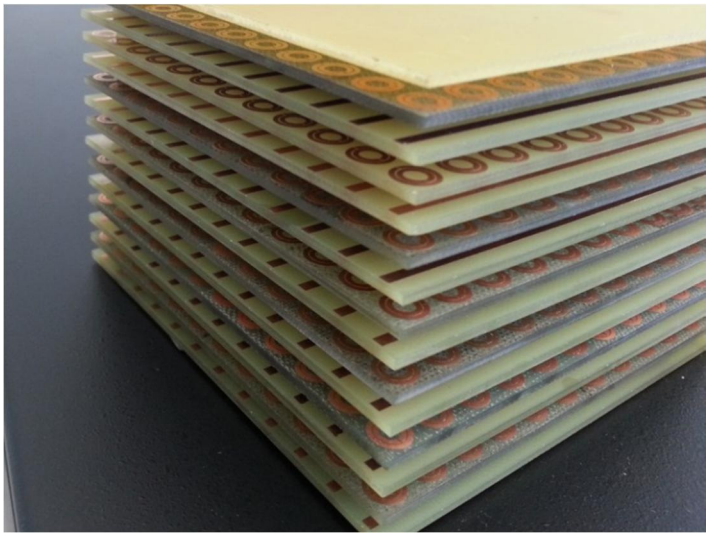

Figure (4.6): Fabricated LHM metamaterial.

4.5 Microwave transmission in Left-Handed Metamaterials

In this section, the transmission properties of left-handed metamaterials composed of periodic SRRs and thin wires arrays, shown in Figure 4.6 and 4.7 will be investigated.

Figures 4.6 and 4.7 shows a three dimensional Left Handed Metamaterial composed of layers of SRR and wire arrays altogether a composite metamaterial of 7 layers of SRRs and 7 layers of thin wires. Each layer is separated by a 3.15 mm gap. All the layers were machined from 100x100mm PCB with 12x12 units of SRRs and the corresponding array of 12 thin wires.

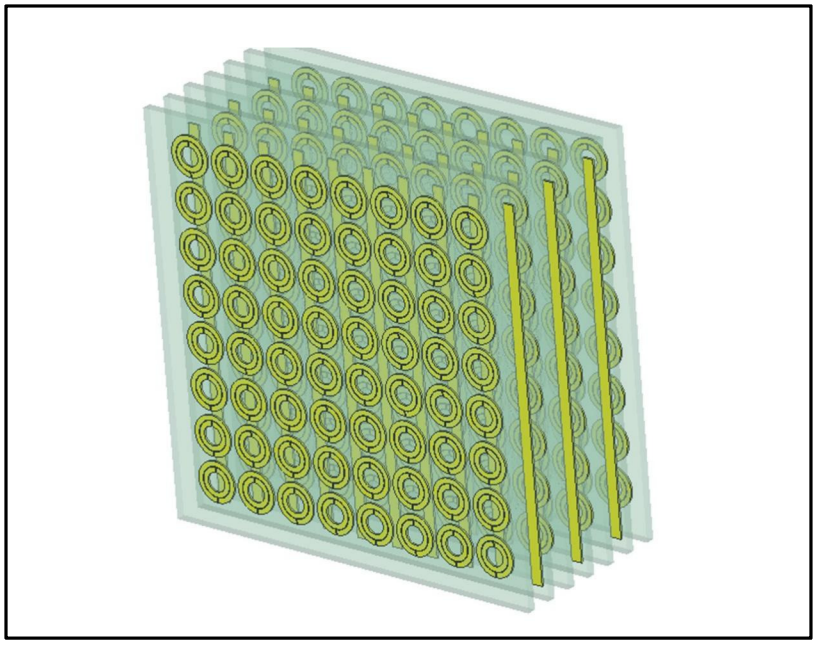

Figure (4.7): Designed LHM metamaterial with CST microwave.

4.5.1 Negative permittivity

Negative permittivity can be attained by fabricating periodic thin metallic wire structures onto dielectric substrate with appropriate parameters. Pendry *et al* calculated in detailed the negative permittivity achieved at microwave frequencies [64]. In summary, he derived the following equation which defines the thin wire geometrical parameters at a given frequency:

$$\omega_p^2 = \frac{2\pi c^2}{a^2 \ln(a/r)} \text{----------} (4.6)$$

Where ω_p is the resonance frequency (plasma frequency in this case) (*a*) is the lattice constant, *(c)* is the speed of light in free space and *(r)* is the radius of the wires.

The effective medium theory holds true for the thin wire case as the corresponding wavelength for the resonance frequency is much larger than the radius of these wires.

Therefore, an effective dielectric permittivity is considered, in this case, to determine the permittivity of the medium.

The negative permittivity concept is demonstrated by machining a periodic array of thin wire structures on standard PCB boards using an IR nanosecond fibre laser (section 2.10.1). This process is capable of directly machining the copper layer of the PCB to form structures with dimension of around 3mm and minimum track width of 200μm for the SRR case.

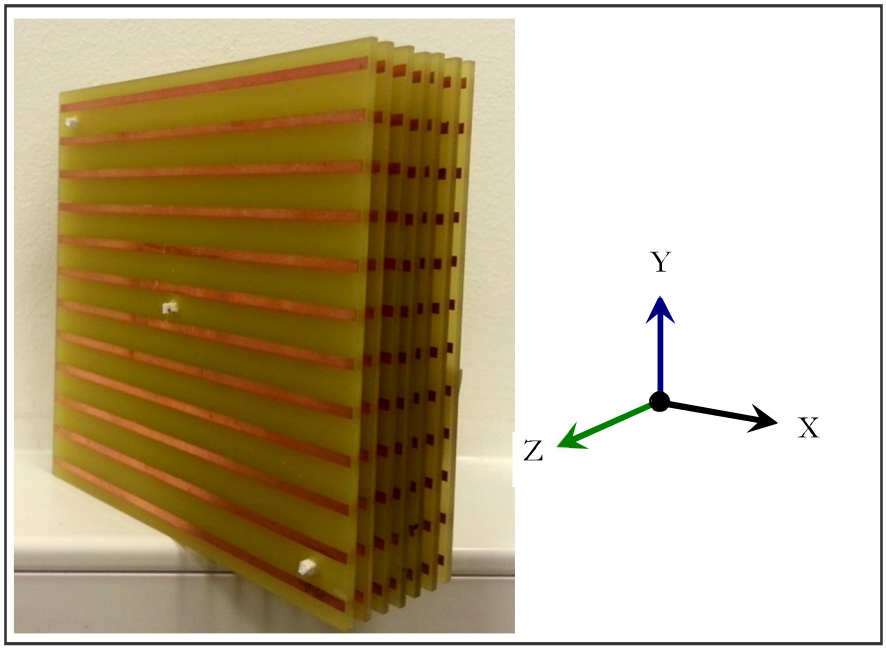

Figure (4.8): Fabricated thin wire medium on 100x100 PCB boards.

It is anticipated that these structures are active in the microwave region that can then be tested using an Anritsu 37397D Network Analyser (10MHz-65GHz). The length and width of the continuous thin wire structures are l = 98.5 mm, and w = 2.0 mm. each PCB board cut to 100 x 100 mm and contain 12 wires separated by 6.3 mm. The array is designed such that when combined with SRR array boards each wire will take a central position behind each SRR (Figures 4.6-4.7). The lattice spacing in z-direction = y-direction = 6.3 mm.

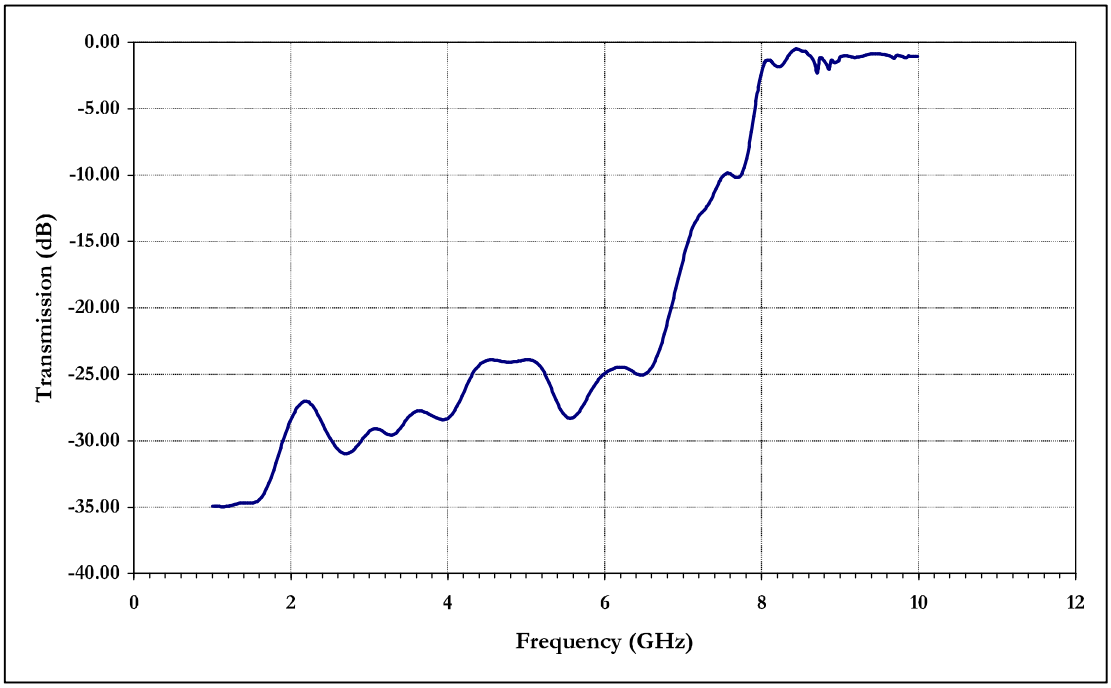

Figure (4.9): Measured transmission spectra of periodic thin wire arrays.

Figure 4.9 above shows measured transmission spectra of a thin wire media. The plasma frequency is located at 8.0 GHz, below which the electromagnetic waves are not transmitted as the permittivity is negative.

The measurement was performed with the network analyser with a sweep set from 1 GHz to 10 GHz, and standard high gain microwave horn antennae as the transmitter and receiver (Figure 4.10).

The wire grid medium is placed between the two horn antennae with the wire direction parallel to the electrical field as shown in figure 4.10 below. The purpose of this setting is to measure the scattering parameters particularly the transmission parameter (S21).

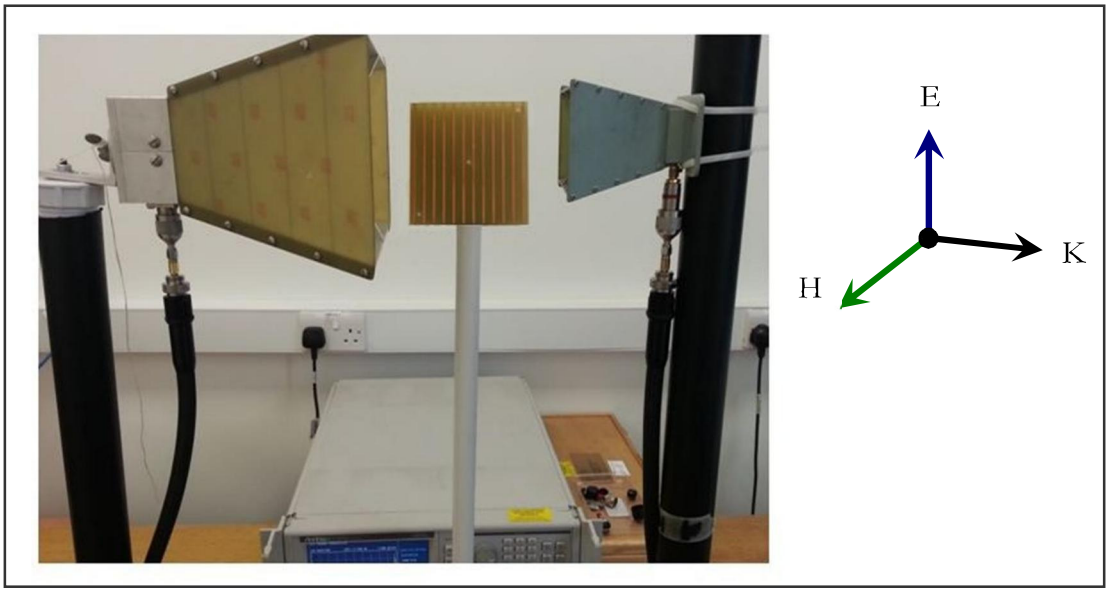

Figure (4.10): Experiment setup to measure transmission through thin wire medium.

Electromagnetic waves are not transmitted in a medium with a negative dielectric permittivity. To explain this behaviour, metals have many free conduction electrons that are free to flow around while the heavy ions remain stationary. Metals behave as a good conductor because these free electrons can be excited and can cancel out any field generated by the incident waves. A metal mirror is an example to this behaviour that can reflects 90-99% of the light. However at high frequencies metals act like plasma and the incident EM wave oscillates too fast for the free electrons and can no longer eliminate the incident wave to reflect all the light.

The metal, in this case (plasma) becomes transparent and the wave can pass through the metal like it was a vacuum but this is a dispersive vacuum (loss medium).

The plasma frequency can be defined as the resonance frequency below which the waves oscillate slowly enough for the electrons to follow.

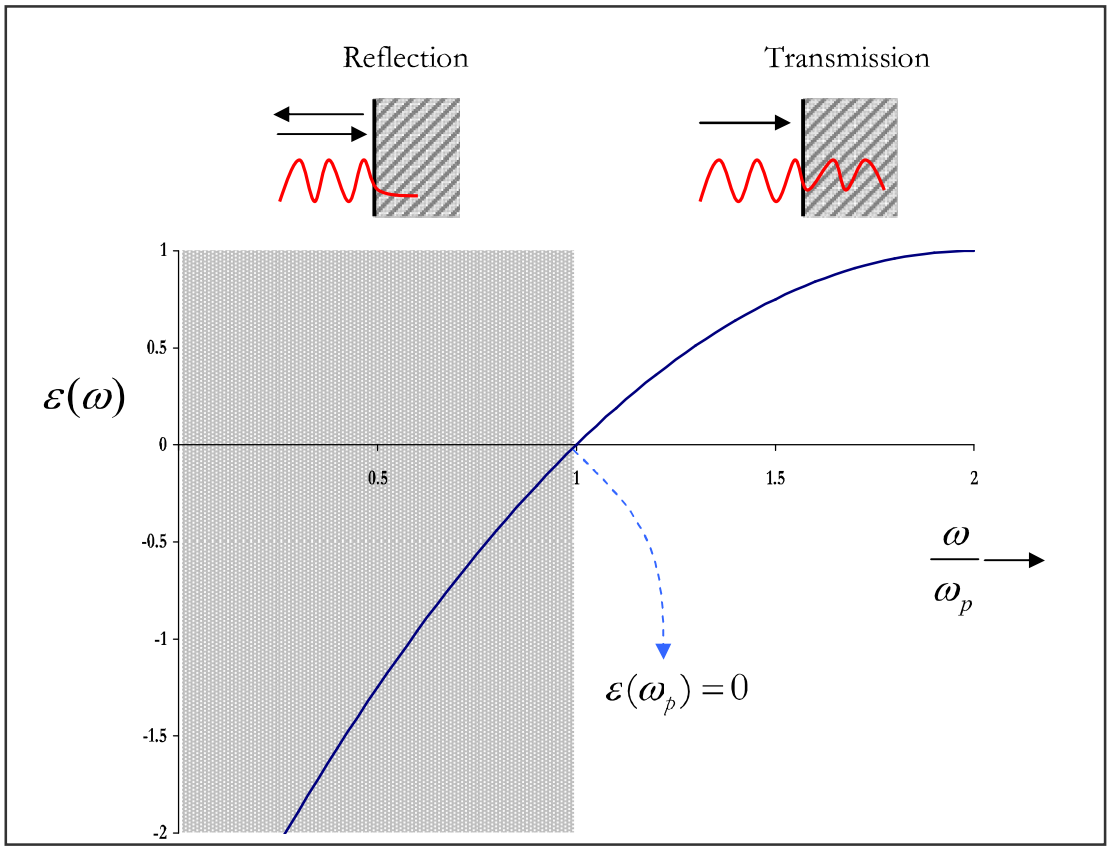

Figure (4.11): Frequency dependant permittivity showing the definition of the Plasma frequency.

The dielectric constant for dispersive medium assuming vacuum permeability and neglecting damping factor can be defined as [61]

$$\varepsilon(\omega) = 1 - \frac{\omega_p^2}{\omega^2} \text{--------(4.7)}$$

Where ω_p is the plasma frequency and ω is the resonance frequency

Equation 4.7 is plotted in figure 4.11 above to determine the region that gives negative permittivity.

Therefore, we see that the equivalent permittivity requires having negative value below plasma resonance and positive value when above this resonance. The following section (4.5.2) demonstrates the effect of adding the SRR structures to the medium. It is to be anticipated that the SRRs contribute to the total effective permittivity causing a

downward shift in the resonance frequency determined from wire structures only. This effect can be observed by using a medium consisting of periodic alternating layers of SRRs and wires (Figure 4.6). SRRs respond to the electrical field due to the discontinuous nature of the SRRs. This resonant frequency is much lower (3.6 GHz) than the plasma frequency of the wire-only structures.

Therefore, designing the Left Handed Metamaterial must take into account whether the plasma cut-off frequency of the wire structures covers the magnetic resonance of the SRR structure.

4.5.2 Negative permeability

Negative permeability can be attained by fabricating periodic split ring resonator (SRRs) structures onto a dielectric substrate with appropriate parameters. The basic form of the effective permeability of the SRRs is derived by Pendry *et al.,* the outcome of their results suggest that SRRs structures could be used to realise a negative effective permeability up to infrared frequencies [1].

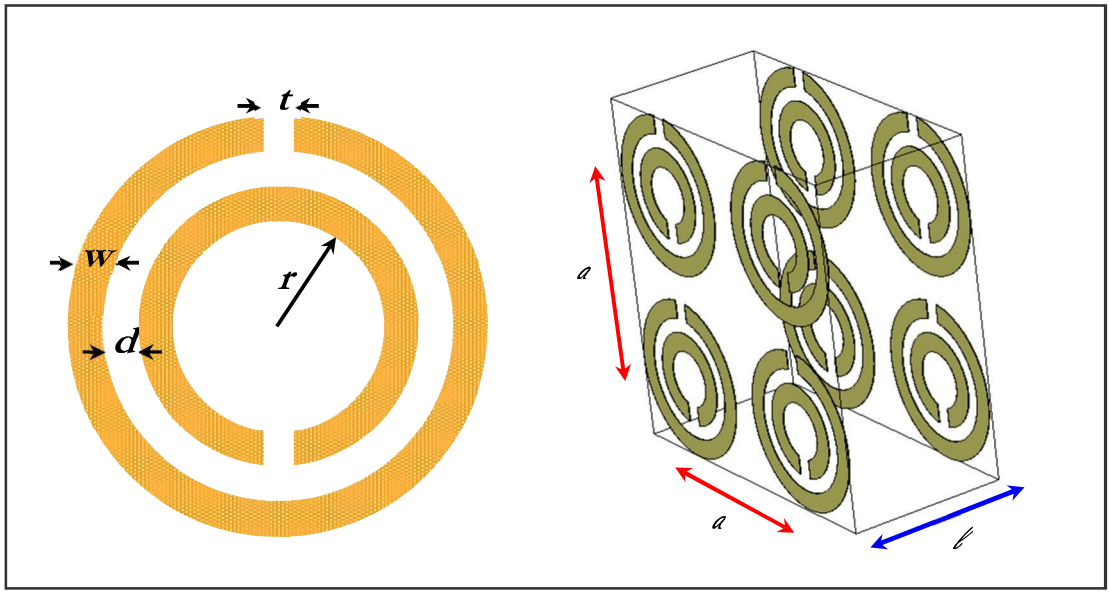

Figure (4.12): left Single SRR and 3D SRRs mediun right.

Ishikawa derived the following equation which defines the SRRs geometrical parameters at a given frequency [65]:

$$\mu_{eff} = 1 - \frac{F\omega^2}{\omega^2 - \frac{1}{C\,L} + i\frac{Z\omega}{L}} \text{--------(4.8)}$$

Where F is the filling factor, Z is the impedance, L and C are the geometrical inductance and capacitance and ω is the angular resonance frequency.

Based on figure 4.12 above, the filling factor F can be represented by:

$$F = \frac{\pi r^2}{a^2} \text{--------(4.9)}$$

Where *(r)* and *(a)* are the inner radius of the SRR and lattice spacing in X-Y plane respectively.

The effective medium theory applies for the SRRs case as the corresponding wavelength for the resonant frequency is much larger than the radius of single SRR. Therefore, an effective magnetic permeability is considered, in this case, to determine the permeability of the medium.

The negative permeability concept can be achieved by machining the periodic array of SRRs structures on standard PCB boards using the ns IR fibre laser (Figure 4.13).

The inner radius of the single SRR is r = 1.6 mm, w = 0.8 mm, d=t =0.2mm. The outer diameter of the ring = 6.8 mm and the unit cell dimensions is 8.33 mm.

Each PCB board is cut to 100 x 100 mm and contains 12 x 12 SRRs separated by 1.53 mm. The lattice spacing in z-direction ℓ = 3.2 mm (Figure 4.12).

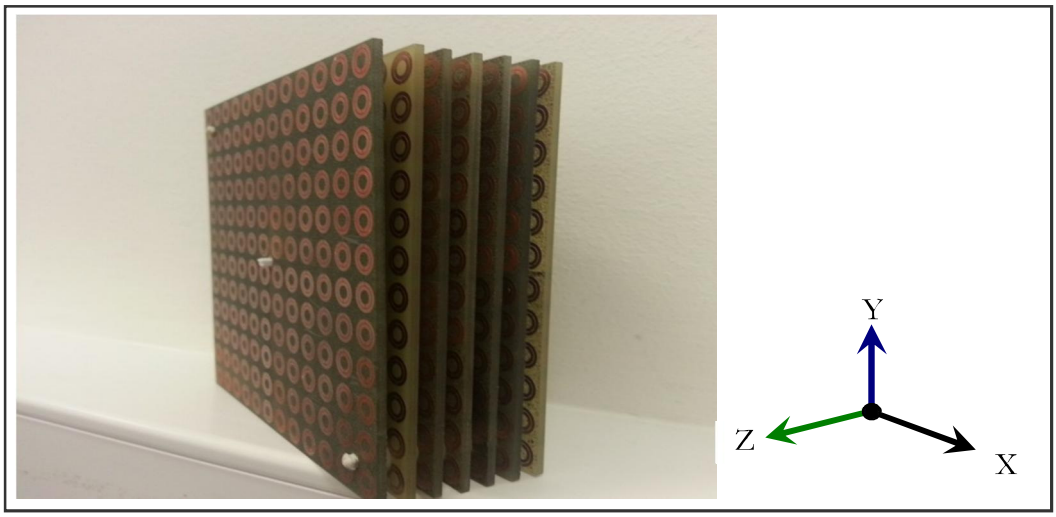

Figure (4.13): Fabricated SRRs medium on 100x100 mm PCB.

Figure 4.14 below shows measured transmission spectra of SRRs media. The resonance frequency is located at 3.5-4.0 GHz, at which the electromagnetic waves are not transmitted as the permeability is negative.

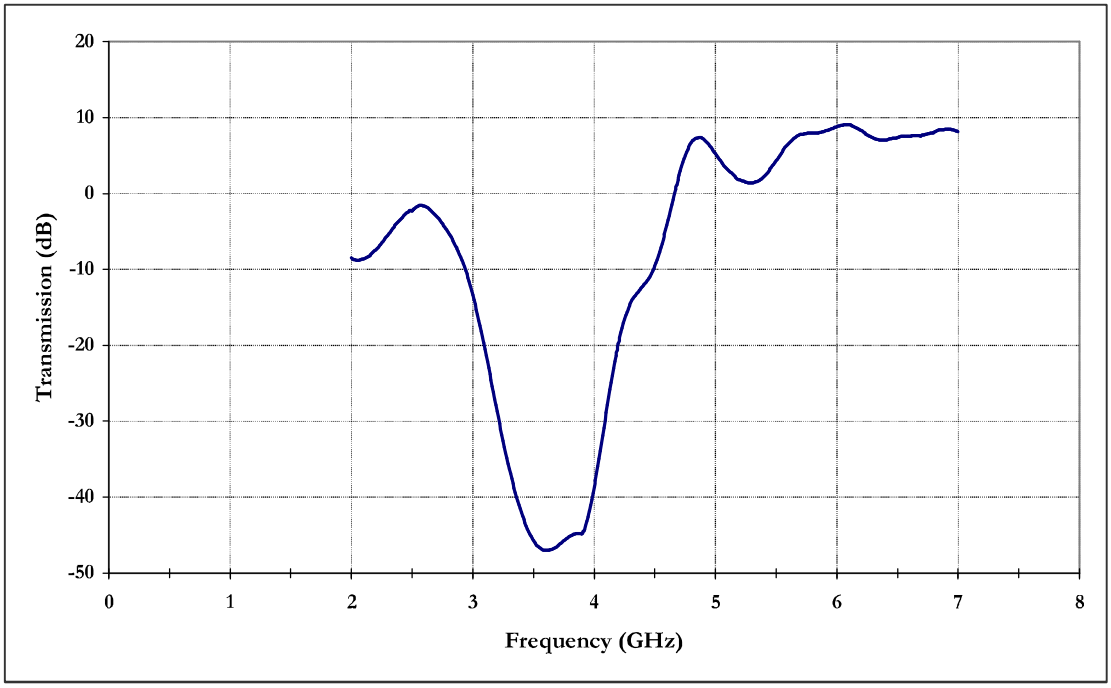

Figure (4.14): Measured transmission spectra of periodic SRRs arrays.

The previous statement can be simply justified with the refractive index definition that determines the EM wave phase velocity propagation. Refractive index is the square root of permeability multiplied by permittivity. If either permeability or permittivity is negative, then the refractive index becomes imaginary, which leads to decay in the EM wave instead of transmission. The other case seen in section 4.5.3 where both permeability and permittivity are negative, which leads to a real, but negative index of refraction which means that the EM wave can propagate, but with reversed phase velocity.

The measurement preformed with Anritsu 37397D Network Analyzer 10MHz-65GHz, a standard high gain microwave horn antennas as the transmitter and receiver as illustrated in figure 4.15 below.

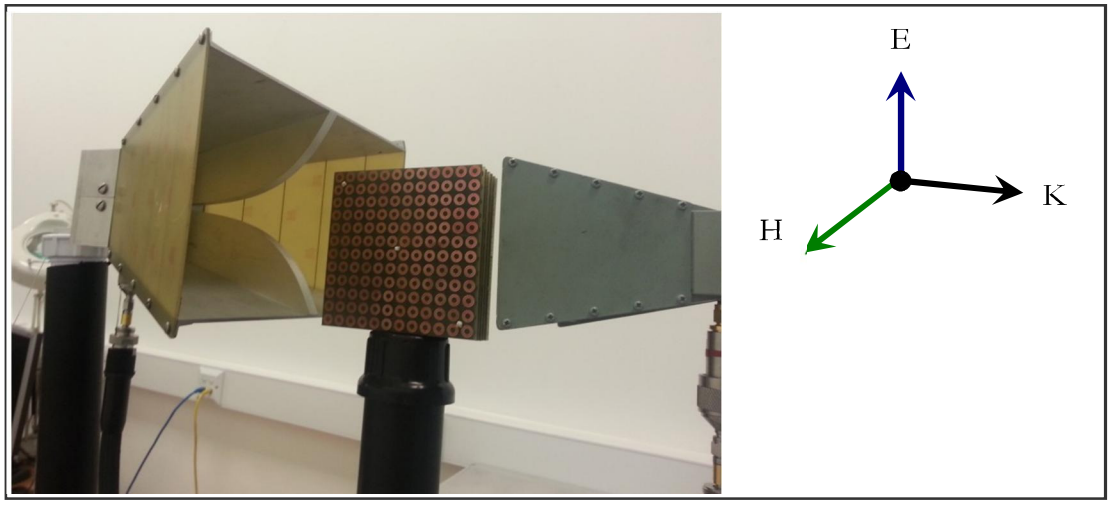

Figure (4.15): Experiment setup to measure transmission through SRRs medium.

The SRRs medium is placed between the two horn antennae with the SRR plane direction perpendicular to the magnetic field as can be seen in figure 4.15 above.

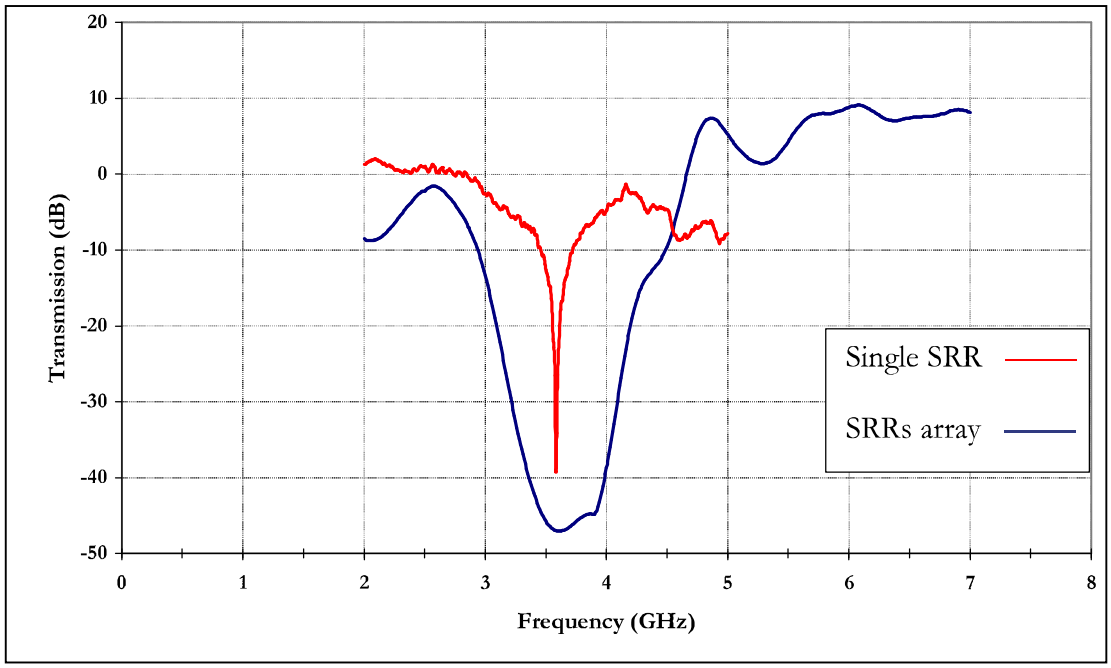

Figure (4.16): Measured transmission spectra of periodic SRRs arrays and single SRR.

The scattering parameters, particularly the transmission parameter (S21), are then measured. The measured transmission results of the transmission parameter (S21) for a single SRR unit cell and periodic array of SRRs shows that there is only a little increase in the transmission magnitude near the resonant frequency and a wider resonance (see Figure 4.16). Therefore, the magnetic resonant frequency results for a single SRR structure can be utilised to predict the magnetic resonant frequency for the periodic array of SRRs.

4.5.3 Double negative metamaterial

Double negative metamaterials are composite structures that exhibit left handed behaviour. The electromagnetic properties of these metamaterials are determined by effective electromagnetic parameters; effective permeability and effective permittivity.

In this section, SRRs structures rendering negative permeability are combined with a thin wire media that exhibiting negative permittivity are used to obtain a double negative metamaterial with left handed electromagnetic properties.

The individual SRRs and thin wire structures used in this section are described in the previous sections 4.5.2 and 4.5.1 respectively.

A schematic drawing and actual photo of the bulk double negative metamaterial is shown in figures 4.7 and 4.6 respectively. This bulk of double negative metamaterial is composed of 7 layers of SRRs interleaved with 7 layers of thin wires. Each layer is separated by a 3.15 mm gap.

All the layers were machined on 100x100 mm PCB boards with 12x12 units of SRRs corresponding to the 12 thin wires.

The length and width of the continuous thin wire structures are l = 98.5 mm, and w = 2.0 mm. Each PCB board contain 12 wires separated by 6.3 mm. The array is designed such that when combined with SRR array boards each wire will take a central position behind each SRR (Figures 4.6-4.7).

The lattice spacing in z-direction = y-direction = 6.3 mm. Each SRR layer machined on 100 x 100 mm PCB board and contains 12 x 12 SRRs separated by 1.5 mm. The inner radius of the single SRR is r = 1.6 mm, w = 0.8 mm, d=t =0.2mm (Figure 4.11). The outer diameter of the ring is 6.8 mm and the unit cell dimension is 8.3 mm. The lattice spacing in z-direction ℓ = 6.3 mm (figure 4.18). The s-parameter measurements were performed with an Anritsu 37397D Network Analyzer 10MHz-65GHz, using standard high gain microwave horn antennas as transmitter and receiver (Figure 4.17).

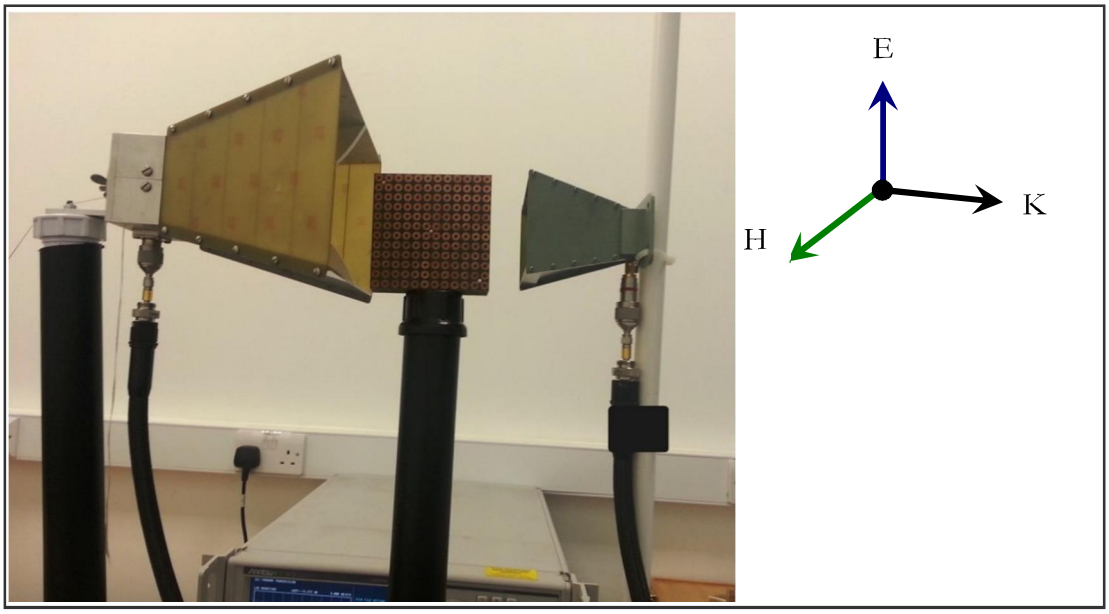

Figure (4.17): Experiment setup to measure transmission through DNG medium.

The DNG medium is constructed with the wires running parallel to the planes of the SRRs (figure 4.18). The entire DNG medium placed between the two horn antennas with wire direction along the electrical field while the magnetic field is perpendicular to the SRRs plane as can be seen in figures 4.17 and 4.18.

The purpose of this setting is to promote negative permeability and permittivity from the SRRs and thin wire structures respectively. These negative parameters are expressed by mean of scattering parameters particularly the transmission parameter (S21) and reflection (S22).

Figure 4.19 below compared the measured transmission spectra of SRRs layers (blue line) with composite DNG layers (red line). The SRRs structures arrangement and transmission parameters are identical to the one examined in previous section (4.5.2).

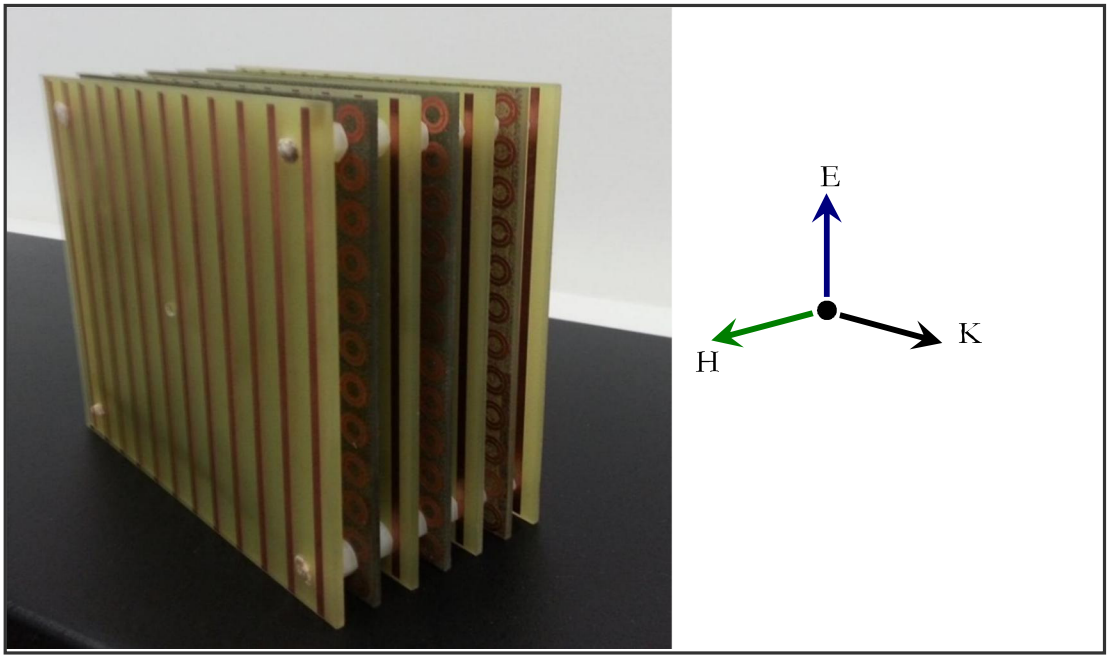

Figure (4.18): Direction of electrical and magnetic field components passing through an example of constructed DNG medium.

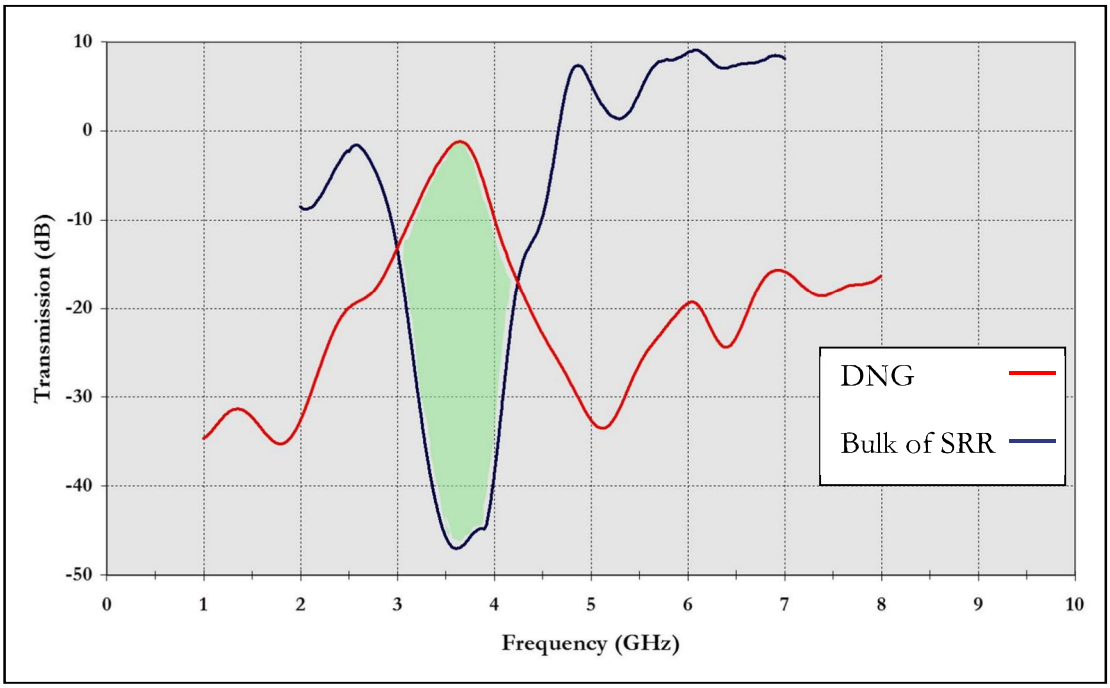

Figure (4.19): Measured transmission spectra of DNG and periodic SRR

The stop band (plasma frequency) of the thin wire array that is used to construct this DNG metamaterial is located at frequency below 8 GHz as in the previous section

(4.5.1). Consequently, the effective permittivity of the thin wire array is negative at frequencies below 8 GHz.

The resonance frequency of the SRRs is located between 3.5 and 4.0 GHz which influence the stop band in the transmission spectrum as explained previously in section 4.5.2. The effective magnetic permeability is negative within this frequency range.

Left handed transmission is achieved with this DNG metamaterial, that is both the effective permeability and permittivity are simultaneously negative at a particular frequency range. The frequency band at which both permeability and permittivity are negative is located between 3.5 and 4.0 GHz (the shaded area in the figure 4.19).

The transmission frequency for the thin wire media alone has a stop band below 8 GHz as can be seen in figure 4.9 in section 4.5.1. Meanwhile, this stop band has been shifted to a lower frequency when adding SRRs structures to construct DNG metamaterials. This is due to electric responses of the SRRs that contribute to the total electric responses of the composite DNG medium. This can be seen in figure 4.19 when the DNG peak goes up again.

4.6 Left handed behaviour verification

The transmission prosperities of SRRs and DNG media were investigated in the previous section to characterize the negative permeability and permittivity. In this section, two experiments are carried out to verify left handed behaviour and to determine the index of refraction of the DNG metamaterial within the resonance frequency region (shaded area in figure 4.19). The first experiment performed was to calculate refraction from cuboid (slab)-shaped DNG metamaterial. The second refraction experiment is to construct a

wedge-shaped DNG to verify the left-handed property and to calculate the negative refractive index of the structure.

4.6.1 Refraction through slab-shaped DNG metamaterials

In this section, the left handed behaviour imposed by double negative media (DNG) is investigated and compared with typical dielectric media that have right handed properties. The direction of the electromagnetic wave transmission through the material can be determined by the law of refraction (Snell's law).

Figure 4.20 (a) below shows the expected directions of EM wave travelling through dielectric material with positive index of refraction, FR4 in this case, based on Snell's law. Whereas figure 4.20 (b) demonstrates the anticipated behaviour of the same EM wave inside DNG media with negative index of refraction.

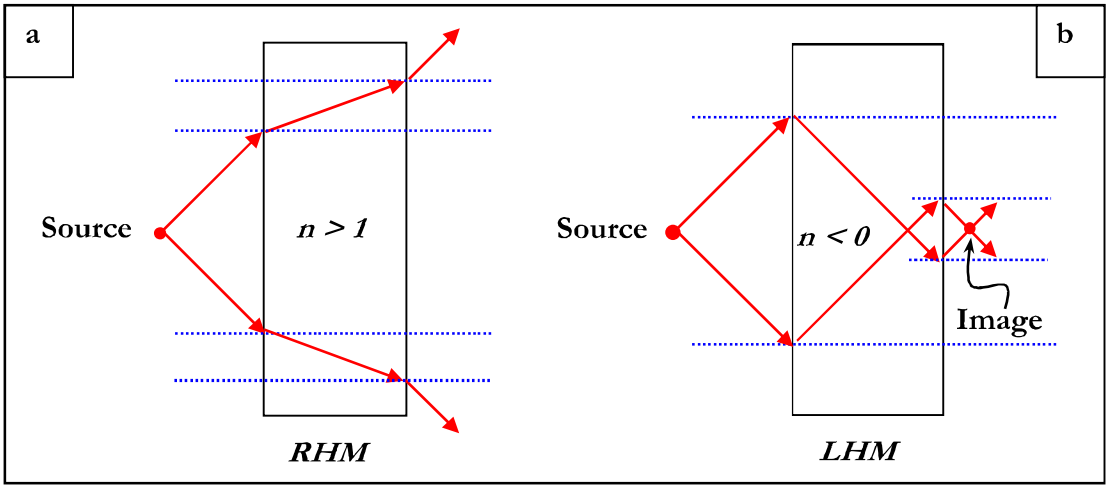

Figure (4.20): EM wave passing through (a): RHM media and (b): LHM media.

The measurements were performed with Anritsu 37397D Network Analyzer 10MHz-65GHz, a standard high gain microwave horn antenna as the transmitter and a monopole antenna as a receiver (figure 4.21).

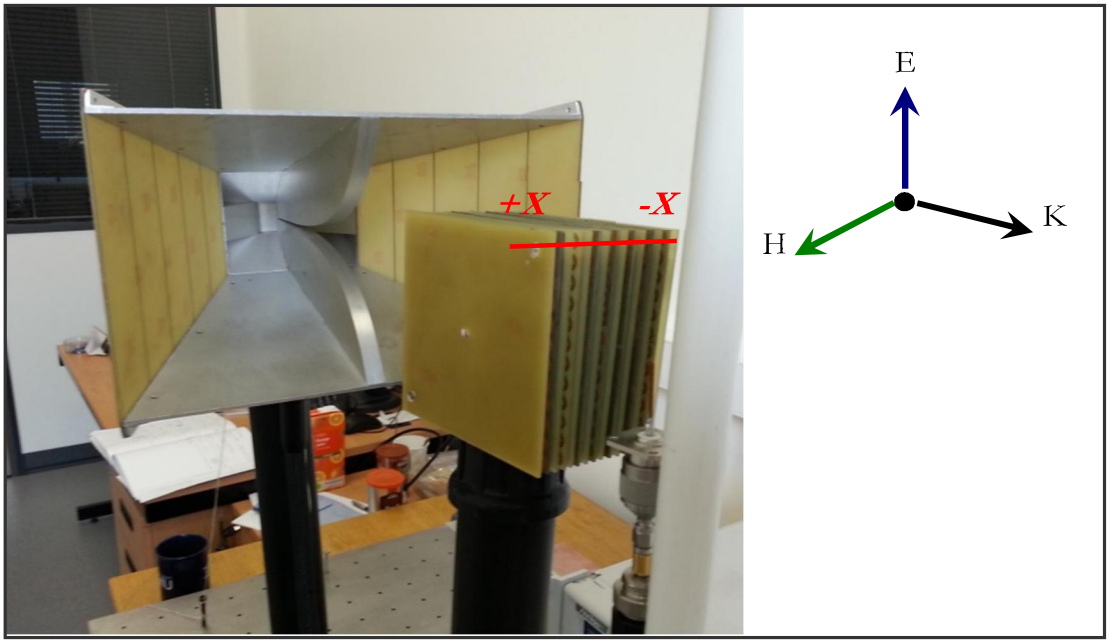

Figure (4.21): Experiment setup to measure refraction through DNG slab.

The monopole antenna design is based on the frequency range where both permittivity and permeability are expected to have negative value from section 4.5.3 (shaded area on figure 4.19). A 7 x 1.67 mm copper wire soldered to N-type connection made for monopole antenna construction. The monopole is then connected to the Network Analyzer to measure the reflection parameter (S22). The length of the copper wire was reduced gradually until a reflection peak appears at desired frequency range. The reflection peak or peaks means that the monopole antenna will work well at that frequency or frequencies in the case that multiple peaks are seen.

The final length of the monopole antenna was 4 cm which agreed with the half wavelength rule of constructing monopole antennas. The centre line of the working frequency is υ= 3.75 GHz and the corresponding wavelength equal to $c/\upsilon = 3 \times 10^8 / 3.75 \times 10^9 = 8$ cm.

The horn antenna used is a pyramidal horn antenna (four-sided pyramid) with a rectangular cross section. This type of horn is used with rectangular waveguides that

transmit linearly polarized plane waves. The pyramidal horn has equal flaring in both electrical and magnetic field directions and the wave propagates normally to the plane of these vectors.

The power transmitted from the waveguide is radiated in a forward direction and as the edge of the horn is flared, the diffraction at the edge is decreased and directivity improves. Therefore the wave will remain unchanged over short distances compared to the desired wavelength size (85 mm) and this type horn antenna [66]

Figure 4.22 below is a schematic drawing showing the experimental setup to better understand and compare left handed media (Figure 4.22 A) with the conventional right handed behaviour illustrated in figure 4.22 B.

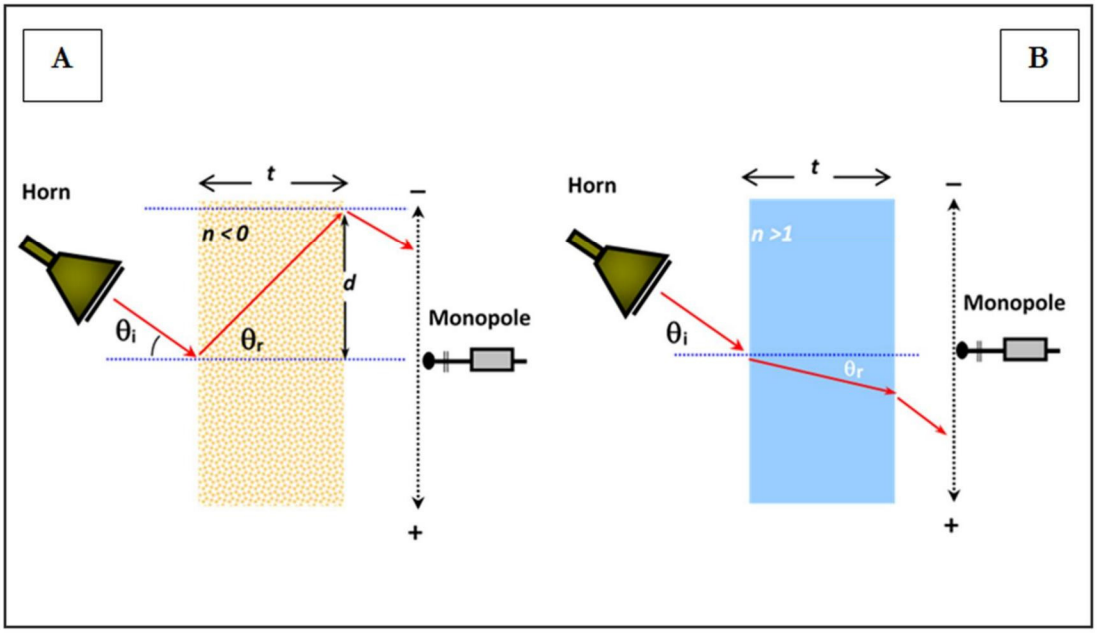

Figure (22): Experimental setup comparing left handed refraction with conventional right handed refraction through a glass like dielectric material and DNG slab.

The monopole antenna is fixed on linear stage with a millimetre graduated scale and 25mm away from the 63.35 mm side of the slab.

The desired microwave frequency of 3.75 GHz transmitted from the horn antenna and detected with the monopole antenna on the other side of the DNG.

The transmission horn antenna is mounted on a rotating stage with 360^0 graduated perimeter scale and positioned on the other side of the DNG slab (figure 4.21). The plane microwave is sent through the DNG slab with an incident angle of $\theta_i = 20^0$ with respect to the DNG surface normal.

The transmitted power spectrum of EM wave is measured by the monopole antenna mounted to the linear stage and moved in 4 mm steps.

The same experiment was performed on empty PCB boards where the entire copper layer had been etched off and cut to 100 x 100 mm and assembled to form a slab of FR4 only. This dielectric slab consists of 14 layers separated by 3.15 mm gap. The overall outer dimensions of this slab are 100x100x63.35 mm.

Figure 4.23 below compare the refraction direction between dielectric (red dashed curve) and DNG slab (blue solid curve). Measurements were made every 4mm as indicated by the datapoints. The graph shows one experiment. It was observed that the curves obtained were very stable, and the peaks did not vary greatly in position, but not enough data was collected to quantify error bars. The refracted peak power observed at the x-positive side for dielectric slab corresponding to a positive index of refraction. For the DNG sample, the peak occurs at the x-negative side from which we deduce the index of refraction to be negative based on Snell's law which illustrated in figure 4.22.

An effective method to calculate the refractive indices is to employ Snell's law on both dielectric and DNG slabs. The refracted beam from the DNG slab is located at -12 mm away from the centre of the slab. The signal measured at 25 mm away from the slab end,

therefore the index of refraction will be calculated in two steps from the following diagram (figure 4.24).

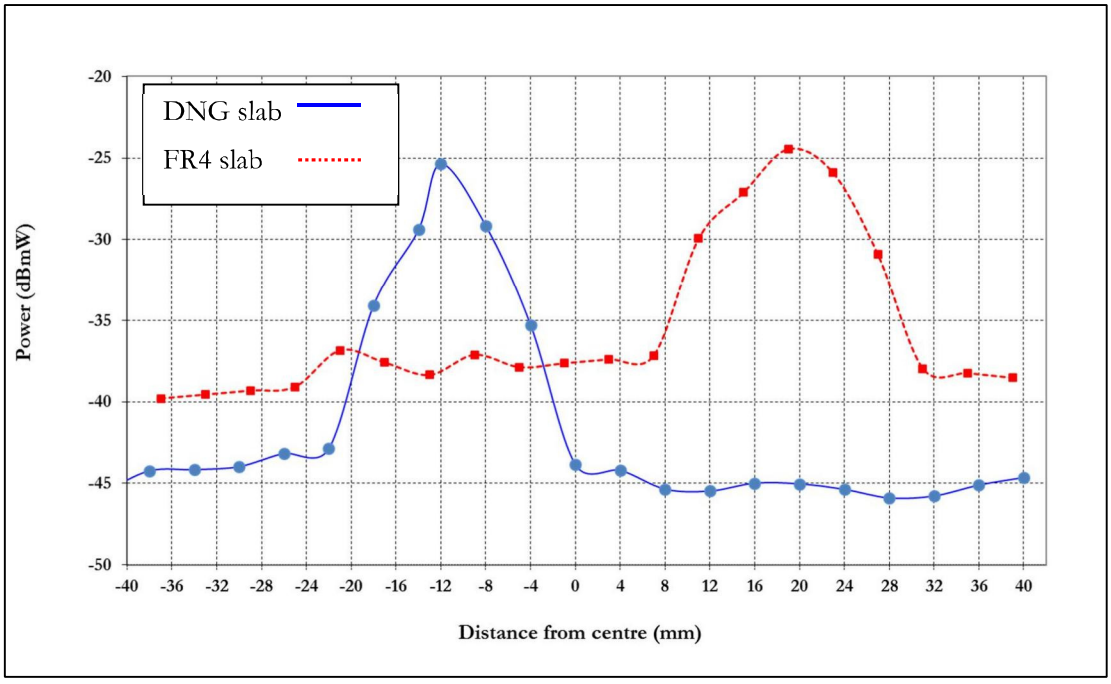

Figure (4.23): Transmitted power of the outgoing EM wave at 3.75 GHz along X-axis.

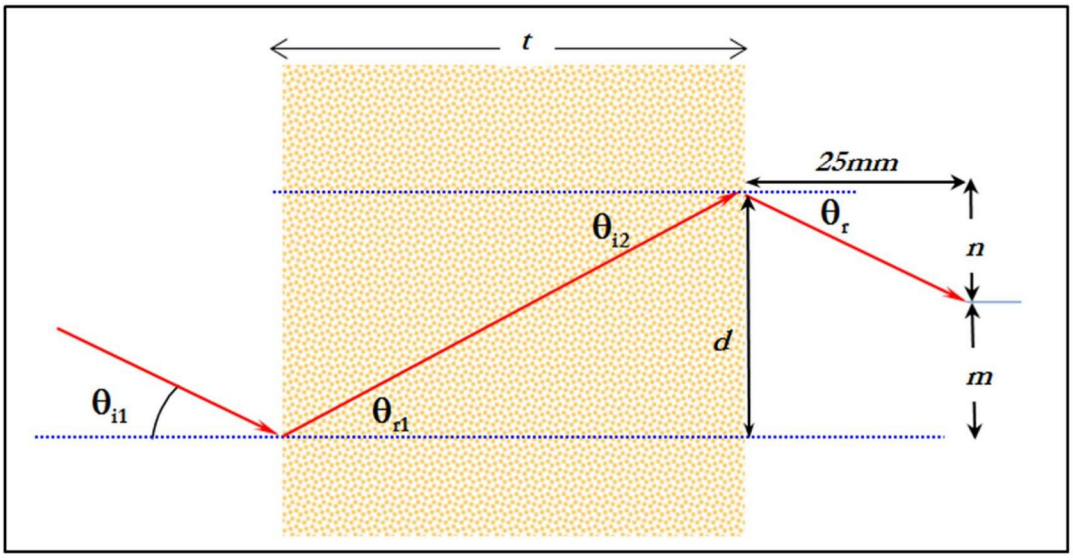

Figure (4.24): Ray tracing for left handed refraction through DNG slab.

The ray incident on the first side of the slab making angle θ_{i1} with the normal and refract inside the slab through angle θ_{r1} (see figure 4.24). In the slab, it travels to the opposite side and becomes incident on the other side through angle θ_{i2} and finally refracts back into air through angle θ_{r2}

From the figure above, m is the measured height, $\theta_{i1} = \theta_{r2}$ and $\theta_{r1} = \theta_{i2}$

$n = 25 \tan\theta_{r2} = 25 \tan\theta_{i1} = 25 \tan 20 = 9.1$ mm

$d = m + n = 12 + 9.1 = 21.1$ mm

The angle of refraction can be calculated from figure 4.24 as following:

$$\theta_r = \tan^{-1}\frac{d}{t} \text{--------} (4.10)$$

Where d is the shift of the beam from the centre and t is the slab thickness.

$\theta_{r1} = \tan^{-1}(d/t)$

$\theta_{r1} = \tan^{-1}(-21.1/63.35) = -18.4^0$

The refractive index of this DNG is then can be calculated from Snell's law:

$$n_{air}\sin\theta_i = n_{DNG}\sin\theta_r \text{---------} (4.11)$$

$$\Rightarrow n_{DNG} = \frac{\sin 20}{\sin(-18.4)} = -1.1$$

Similarly, the refraction index of the FR4 slab can be calculated from figure 4.25 below.

The microwave beam, in this case, shifted 19 mm on the positive side from the centre;

$n = 25 \tan\theta_{r2} = 25 \tan\theta_{i1} = 9.1$ mm

$d = m - n = 19\text{-}9.1 = 9.9$ mm

$\theta_{r1} = \tan^{-1}(+9.9/63.35) = +8.9^{0}$

$$n_{FR\ 4} = \frac{\sin\ 20}{\sin\ 8.9} = 2.18$$

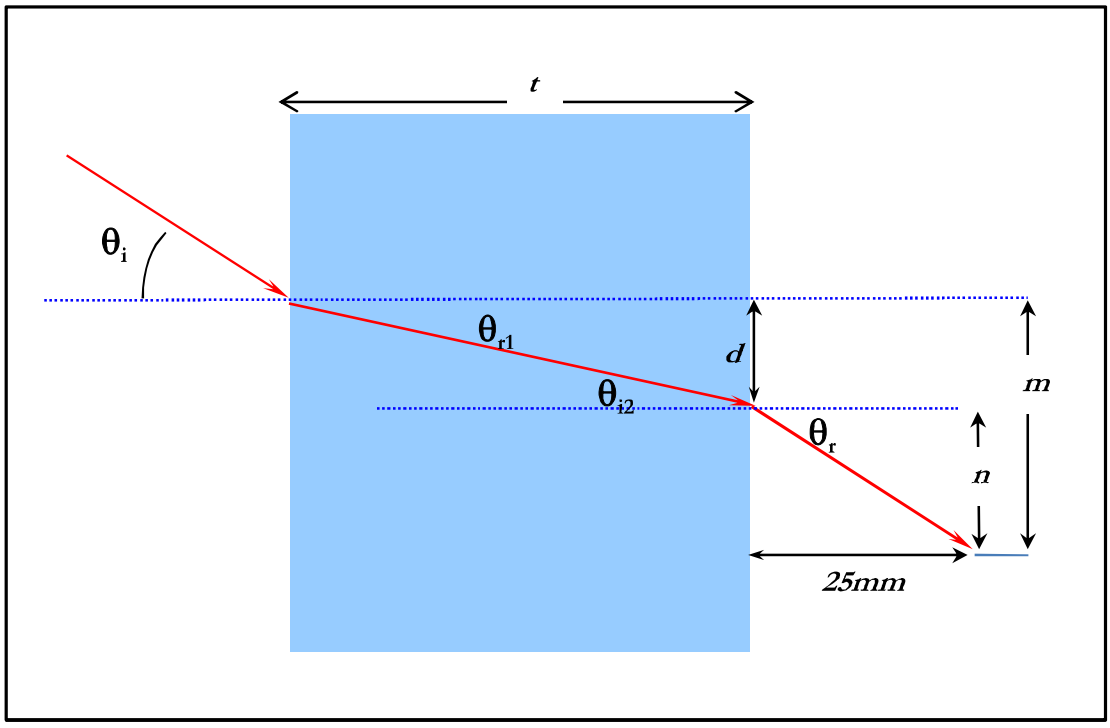

Figure (4.25): Ray tracing for left handed refraction through dielectric material slab.

The PCB manufacturers are secretive when it comes to releasing their trade secrets. In general, the dielectric constant permittivity of FR4 is 4.34 @ 1 GHz with the relative permittivity (εr) is 4.8 [67]. The dielectric constant permittivity for the flexible PCB used throughout this investigation is 5 @ 1 MHz [68].

The refractive index of a material (n) is defined as the ratio of the speed of light in a vacuum to the speed of light in that material.

$$n = \frac{c}{\upsilon} \text{----------} (4.12)$$

Where c is the speed of EM wave in a vacuum and υ is the speed of EM wave in the material. And;

$$c = \frac{1}{\sqrt{\varepsilon_0 \mu_0}} \text{----------} (4.13)$$

Similar equation is applicable to the speed of EM wave in any material, υ:

$$\upsilon = \frac{1}{\sqrt{\varepsilon \mu}} \text{----------} (4.14)$$

The permeability is equal to μ_0 for a non-magnetic material, so that:

$$\upsilon = \frac{1}{\sqrt{\varepsilon \mu_0}} \text{----------} (4.15)$$

The refractive index of the material can be expressed in terms of ε and μ as:

$$n = \frac{1}{\sqrt{\frac{\varepsilon_0 \mu_0}{\varepsilon \mu_0}}} \Rightarrow n = \sqrt{\frac{\varepsilon}{\varepsilon_0}} \text{----------} (4.16)$$

Finally, the definition of the dielectric constant in terms of permittivity is:

$$k = \frac{\varepsilon}{\varepsilon_0} \text{----------} (4.17)$$

$$\therefore n = \sqrt{k} = \sqrt{4.43} = 2.08$$

This calculation agrees well with index of refraction found experimentally above.

4.6.2 Refraction through wedge-shaped left-handed materials

Typically, the left handed refractive behaviour can be demonstrated with a prism-like metamaterial shape by means of refraction through the negative index of refraction material [58-60]. In this section, a wedge shape structure composed of DNG metamaterial is examined with a microwave source from a network analyser to prove the direction of refraction which in turn indicates whether the medium possesses a negative or positive refraction index.

There are several ways to confirm left-handed properties of metamaterial and to verify the proposed structure as a true DNG metamaterial. To name a few, negative beam shift, negative Goos-Hanchen shift, reversed Cherenkov radiation, and reversal Doppler shift [5,57]. However the most straight forward method is to use Snell's law on a wedge shape or flat-slab as refraction at the surfaces causes the electromagnetic wave to deflect by a fixed angle. Also a wedge shape is easy to construct or to engineer from a flat-slab shape.

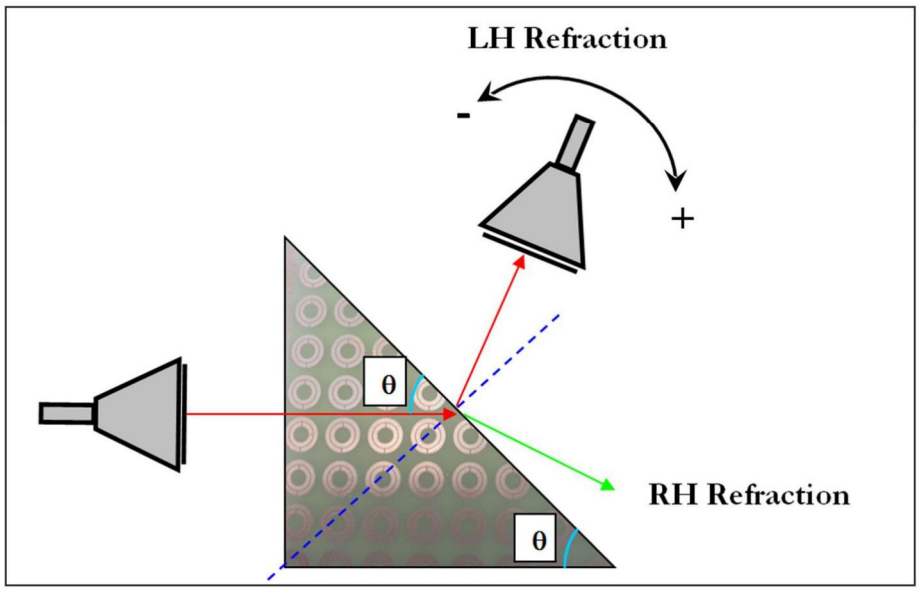

Figure (4.26): Compare left handed with the conventional right handed refraction through wedge shape dielectric material and DNG wedge.

With Snell's law the incident wave will be bent to the same side of the surface normal as that of the incident wave for DNG material, while for normal materials, the beam refracted to the opposite side of the surface normal.

Figure 4.26 above shows the experimental setup and compares the left handed refraction with the typical right handed one.

In this experiment the wedge shaped structure composed of 2D SRR and thin wire PCB boards stacked in the same manner as the one been used previously in section 4.5.3 and 4.5.1. The DNG wedge structure is composed of 12 layers of SRRs and 12 layers of thin wires with each layer separated by 2.5 mm gap (figure 4.27).

The layers spacing reduced from 3.15 mm (slab shape spacing) to 2.5 mm to cut down the wedge height to increase stability. Also it is expected that reducing the wedge height will yield smaller wedge angle that refract the beam to a higher angle. This will help in distinguishing between right handed and left handed refraction.

In this context reducing the gap between unit cells will increase the filling factor (Eq. 4.9) that according to equation 4.8 will shift the resonance frequency to a slightly lower value.

The wedge arranged in 12 steps with the number of unit cells reduced by one with each step. Each step is formed of two layers of SRRs and wire board that has the same external dimensions. The first step consist of SRR and wire layers machined on 100 x 100 mm PCB board with 12 x 12 units of SRRs correspond to 12 thin. The final step of the wedge has a 1 x 12 SRRs unit cells and one thin wire. The short side of the wedge contains 12 SRRs cells and 1 thin wire; the long side contains 12 x 12 SRRs unit cells and 12 wires.

The resultant outer dimensions of the wedge are 100x100 base and 96 mm height that yield a wedge angle of $\tan^{-1} 96/100 = 43.8^0$.

The measurement preformed with Anritsu 37397D Network Analyzer 10MHz-65GHz, two standard high gain microwave horn antennas as transmitter and receiver (figure 4.27).

The electromagnetic wave from the transmission horn is incident normally on the first interface of the DNG wedge sample (Figures 4.26 and 4.27). Thus, the incident beam will not be refracted at the first surface.

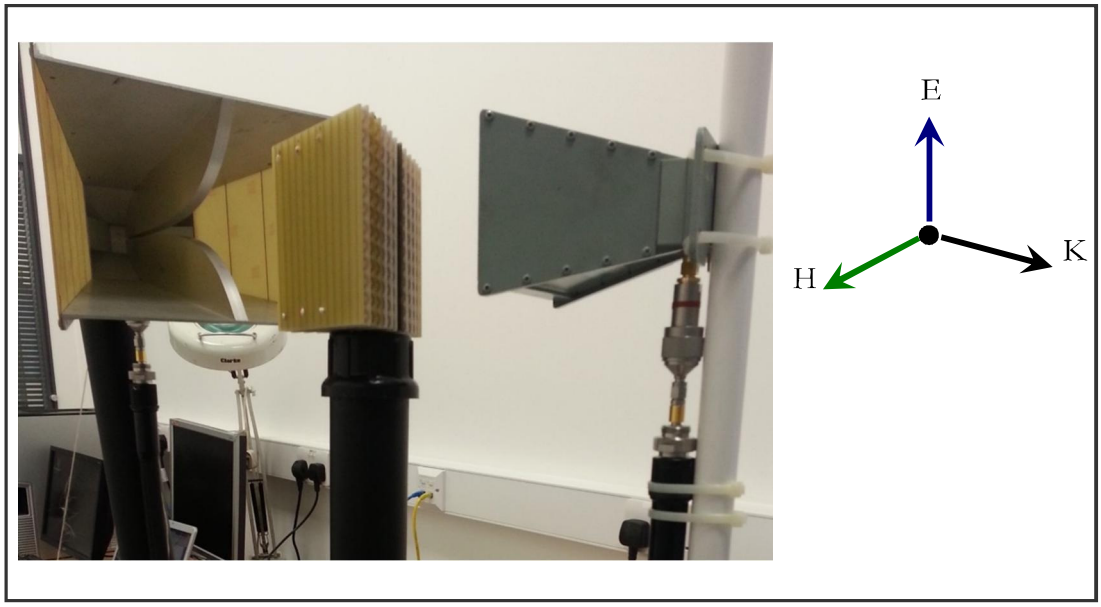

Figure (4.27): DNG wedge shaped experiment setup.

The refraction is expected to occur at the second interface of the wedge as the beam is incident at an angle equal to the 90° less the wedge angle. Figure 4.26 compares the direction of the refracted beam from wedges with positive and negative refractive indices. According to Snell's law the beam will be refracted at the opposite side of the normal for positive refraction index material (green arrow in figure 4.26). However, if the wedge

structure has a negative index of refraction, the refraction will occur at the same side of the normal (red arrow in figure 4.26).

The transmission horn antenna is mounted on a fixed post to send the microwave beam normally on the first surface of the wedge. This beam exits the DNG wedge with an angle to be detected by the receiver horn antenna. The receiver horn antenna is mounted on a rotating stage with 360^0 graduated perimeter scale to obtain the angular power distribution of the refracted microwave. This detector antenna was rotated in 10° steps on a circular arc centred on the wedge's post holder and the transmitted power spectrum at each step was recorded with the Anritsu 37397D Network Analyzer.

The network analyser system was calibrated with the two horns connected and without the wedge structure in between. The wedge structure is then positioned on a fixed post between the horns' antennae.

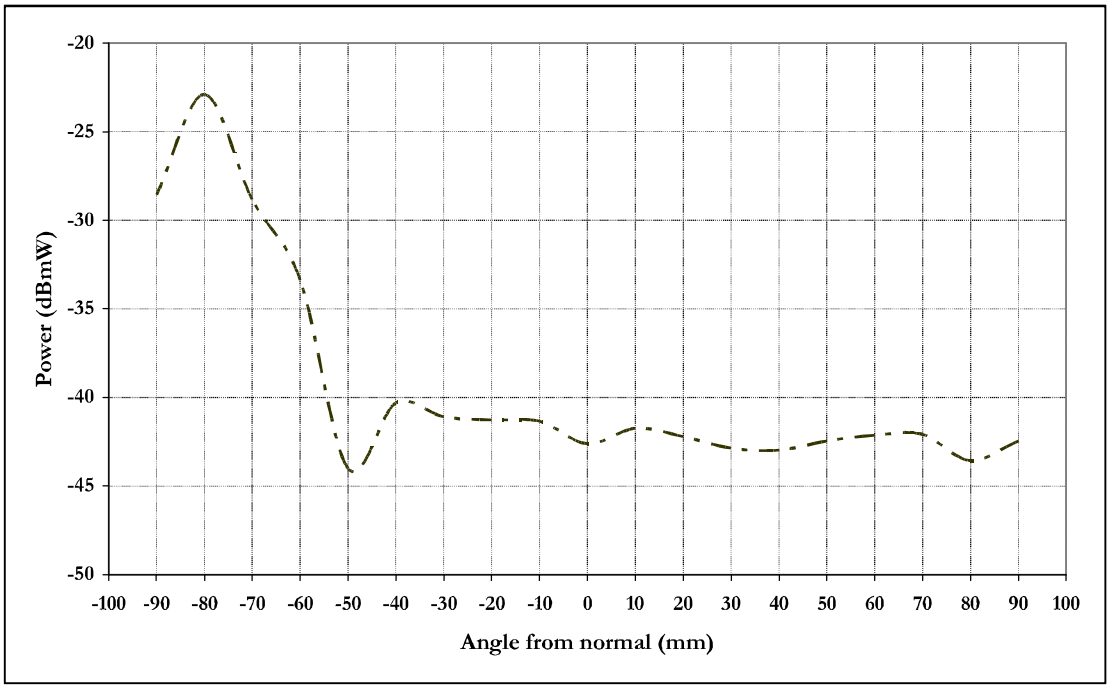

Figure (4.28): Transmitted power at 3.75 GHz of the outgoing EM wave along x-axis.

The result from figure 4.28 above is compared with the refraction diagram on figure 4.26. It is evident from the figure above that the transmitted beam is refracted on the same side of the incident beam with respect to the normal line perpendicular to the boundary on the wedge surface (see figure 4.26). This negative refraction of 3.75 GHz microwave at the DNG wedge corresponds to the negative index of refraction where both permittivity and permeability are negative.

The measured angle of refraction was $\theta_{refraction} = -80°$ corresponding to 3.75 GHz incident wave frequency. Snell's law can be employed to calculate the index of refraction of the DNG wedge metamaterial as following:

$n_{eff} \sin\theta_{incident} = n_{air} \sin\theta_{refractio}$.

$\theta_{incident}$ = 90-wedge angle =46.2^0 and the angle of refraction $\theta_{refraction} = -80^0$

The refractive index (n_{eff}) = -1.36

4.6.3 Refraction through engineered left-handed materials wedge

This section will explore the engineering possibility of DNG metamaterials and in particular examine the performance of a geometry machined into a bulk DNG metamaterial. From the point of view of a metamaterials user, it may be preferred that the bulk metamaterial can be cut to the shape and size required without affecting its electromagnetic properties.

The slab-shaped DNG structure used previously in sections 4.5.3 and 4.6.1 is employed in this experiment with one difference; that is all the gaps between the layers are filled with FR4 boards. The DNG slab formed in this case is a solid bulk. It can then be cut by mechanical saw across the diagonal of the square side that contain SRRs (figure 4.29).

The cut goes through all layers forming 2 wedges. The sawn cut edge will have passed through SRR's and wires, so each wedge will have incomplete SRRs or wire (figure 4.30).

The DNG structure is composed of 4 layers of SRRs, 4 layers of thin wires and 21 layers of FR4. Each layer separated by 4.8 mm FR4 boards. All layers machined on 100 x 100 mm PCB board with 12 x 12 units of SRRs corresponding to 12 thin wires. The FR4 layers were cut to 100 x 100 mm. The resultant outer dimensions of the slab are 100x100x 46.4 mm.

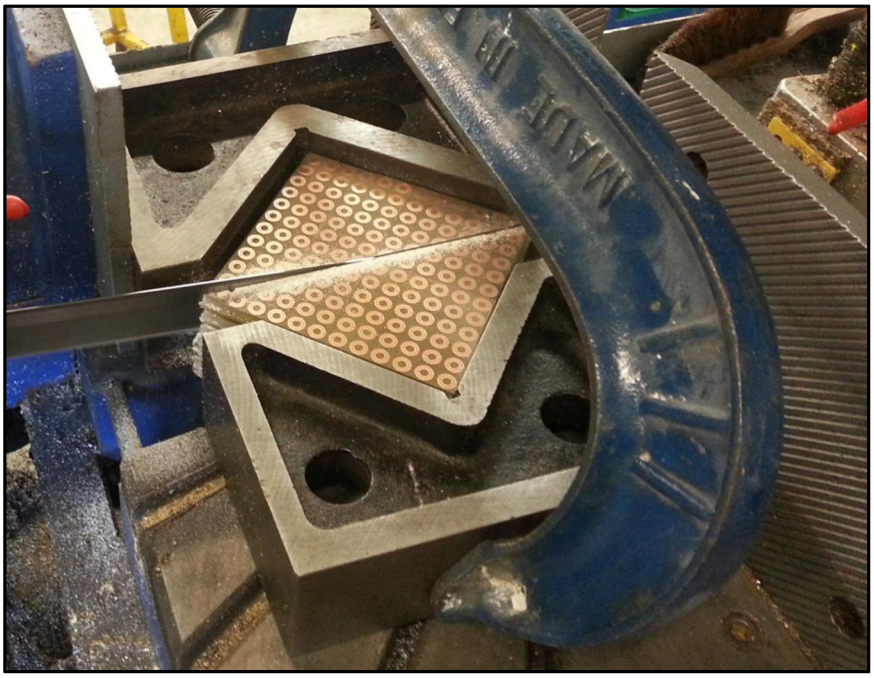

Figure (4.29): Bulk DNG metamaterial cut in 2 halves.

The final dimensions of the cut wedge are 100 x 100 side, 141.4 diagonal and 46.4 height. The transmission measurements were performed with Anritsu 37397D Network Analyser 10MHz-65GHz and two standard high gain microwave horn antennae as the transmitter and receiver (Figure 4.30).

The transmission horn antenna is mounted on a fixed post to send the microwave beam in a direction normal to the first surface of the wedge. This beam exits the DNG wedge with an angle to be detected by the receiver horn antenna.

The receiver horn antenna is mounted on a vertical linear stage to obtain the power distribution of the refracted microwave. This detector antenna was moved up in 10 mm steps on a linear path centred on the wedge's post holder and the transmitted power spectrum at each step was recorded with the Anritsu 37397D Network Analyser.

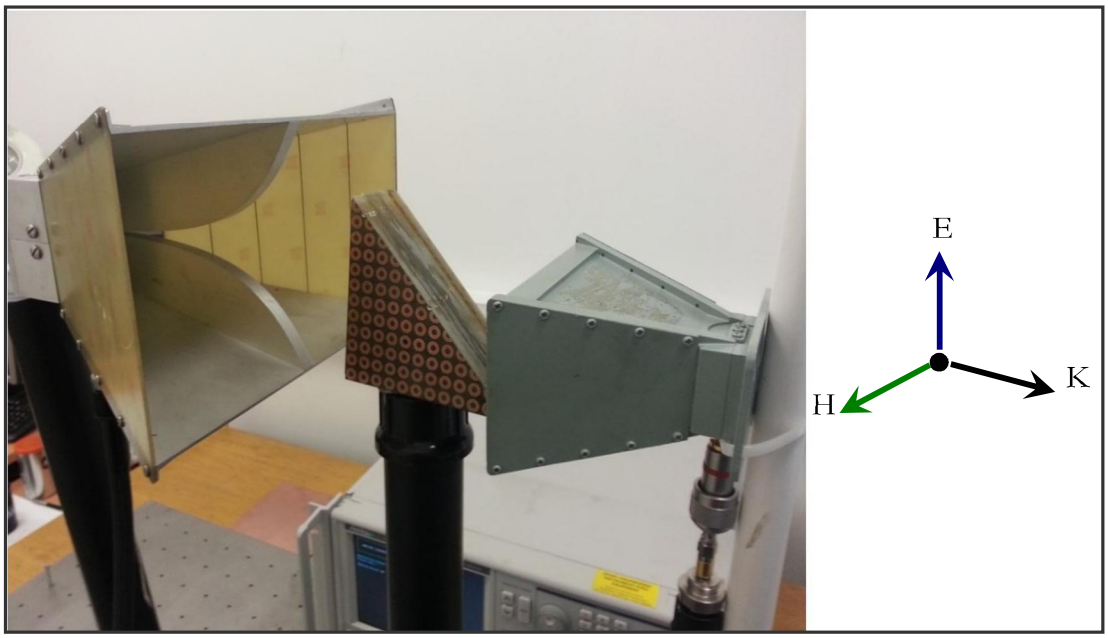

Figure (4.30): Experiment configuration to measure the transmitted power at 3.75 GHz.

This experiment differs from the one performed in the previous section 4.6.2 because the wedge thickness is smaller and the wire direction is upwards (E direction in figure 4.30). The original slab was designed so that when cut in to half, both wedges have partial SRRs and partial wires, and the saw cut is on the face of the SRR plane. If we were to use the designed wedge explained on section 4.6.2 then the cut must be on the side of the slab to keep SRRs aligned to the magnetic field direction and the wires to the electrical field

direction. This can be acknowledged by visualising the orientation of both wedges illustrated in figures 4.27 and 4.30. In addition, this wedge design has narrower depth compared to the previously constructed one. Therefore a linear stage was employed to perform the transmission spectrum with this experiment.

The network analyser system was calibrated with the two horns connected and without the wedge structure in between. The wedge structure is then positioned on a fixed post between the horns antenna.

It is evident from figure 4.31 that the transmitted beam is refracted on the same side of the incident beam with respect to the normal line perpendicular to the boundary of the wedge surface (see figure 4.32).

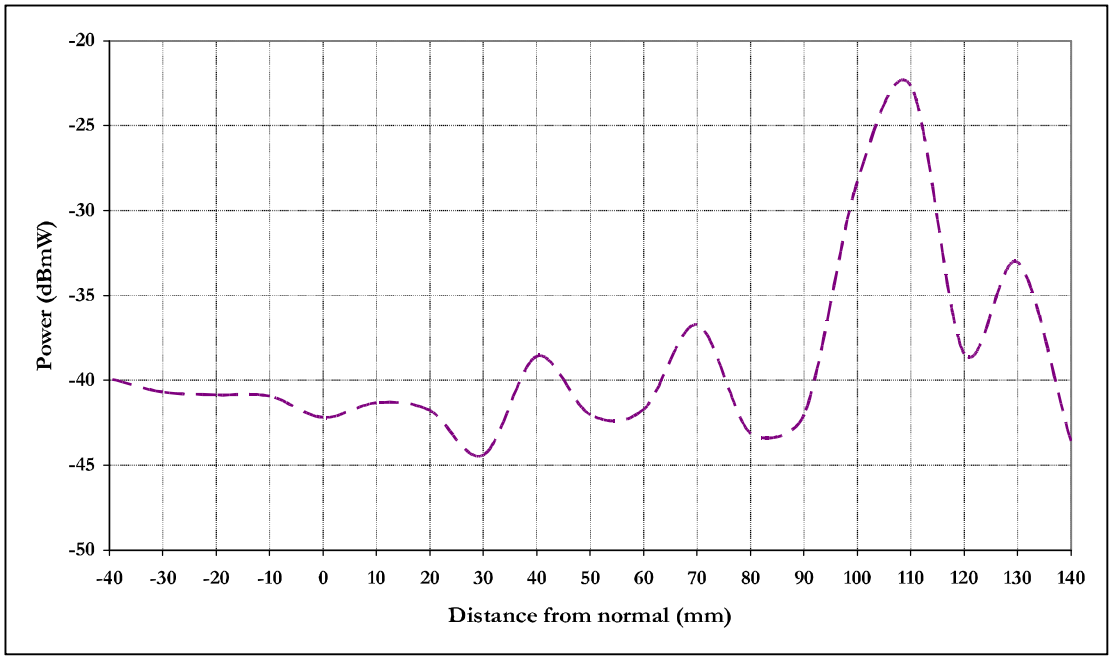

Figure (4.31): Transmitted power at 3.75 GHz of the outgoing EM wave along x-axis.

This negative refraction of 3.75 GHz microwave at the DNG wedge corresponds to the negative index of refraction where both permittivity and permeability are negative.

The refracted peak power observed at the upward side of the wedge from which we deduce that the index of refraction to be negative based on Snell's law which illustrated in figure 4.32 below.

The maximum peak power measured at -110 mm (upward) corresponding to 3.75 GHz incident wave frequency. Employing Snell's law, the index of refraction of the DNG wedge metamaterial can be calculate as following:

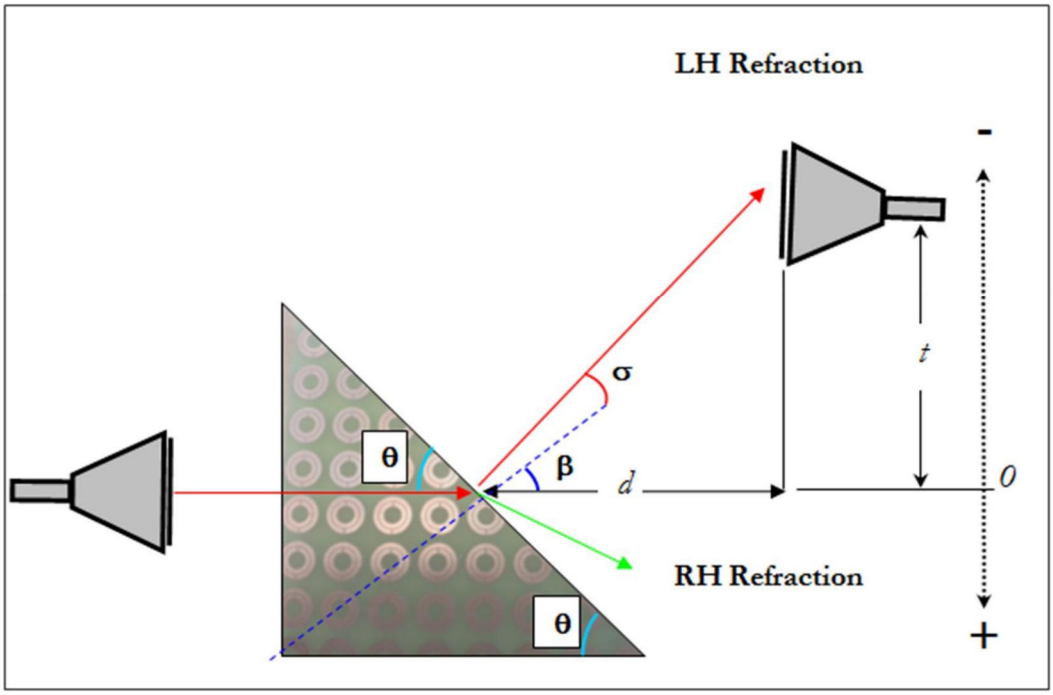

Figure (4.32): Compare left handed with the conventional right handed refraction through wedge shape and ray tracing for left handed refraction calculations.

$n_{eff} \sin\beta_{incident} = n_{air} \sin -\sigma_{refractio}$.

Wedge angle = $\tan^{-1} 100/100 = 45^0$

The incident angle $\beta_{incident}$ = 90-wedge angle $=45^0$

t = 110 mm

d= 20 mm distance from wedge surface to the receiver horn antenna

The angle refraction $\sigma_{refraction} = - [(\tan^{-1} t/d) - \beta] = - [79.7 - 45] = -34.7^0$

The refractive index (n_{eff}) = - 1.24

The aim of the previous sections 4.6.1-4.6.3 was to prove left handed metamaterial behaviour concept rather than determining the precise value of the refraction index.

The metamaterial properties and thus the left handed behaviour of the three shapes used in these sections are different. Metamaterial properties primarily depend on the physical shape of its component unit cells shape, size and distance between them. Also the dielectric constant of the material between the unit cells can affect metamaterial property as explained in details in chapter 3 section 3.3-3.4. These factors alter the effective permeability and permittivity which in turns changes the index of refraction value. Therefore, it was expected to have different index of refraction values for each of the shapes investigated in sections 4.6.1 to 4.6.3. In addition the engineered wedge has partial unit cells that will not act as full resonators and they may cause distortion or losses to the incident wave. However, the magnetic permeability and electric permittivity described with effective medium according to Maxwell equations therefore the effect of one row of half unit cells will be modest compared to the bulk metamaterial.

4.7 Summary

The designed single unit cell SRR and structures obtained from the previous chapter has been employed to construct 2D metamaterials using laser processing techniques as explained in chapter two. These SRRs were machined on standard 2D rigid PCB boards and stacked together to form 3D wedges and slab shaped metamaterials.

The double negativity of permeability and permittivity had been demonstrated for both slab and wedge shaped structures employing refraction measurements and Snell's law for verification. These negative values explain and prove the expected negative index of refraction and metamaterial behaviour.

The microwave transmissions in these LHM metamaterials were investigated to determine the index of refraction value for each 3D structure. The transmission measurements were performed with Network Analyser and two standard high gain microwave horn antennae as the transmitter and receiver.

A rigid wedge shaped had been cut out of slab shaped LHM metamaterial and the continued metamaterial behaviour is verified. The resultant wedges have properties similar to the original cube.

Appendix 4.1: Metamaterial Abbreviations and Nomenclatures

Abbreviations and Nomenclatures	
Backward Wave Medium	BW
Complementary Split Ring Resonator	CSRR
Double Negative Material	DNG
Double Positive Material	DPS
Double Spiral Resonator	DSR
Double Slit SRR	DSSR
Electromagnetic Band Gap structured material	EBG
Epsilon Negative Material (Permittivity)	ENG
Left-Handed Material	LHM
Mu Negative Material (Permeability)	MNG
Metamaterial	MTM
Negative Index of Refraction Material	NIM
Negative Index of Refraction Material	NIR
Negative Phase Velocity Material	NPV
Negative Refractive Index Material	NRM
Photonic Band Gap Material	PBG
Single Negative Material	SNG
Spiral Resonator	SR
Split Ring Resonator	SRR

Chapter Five

Optical Transformation and Cloaking

5.1 Introduction

Based on a coordinate transformation approach, Pendry et al (2006), have reported electromagnetically anisotropic and inhomogeneous cloaks that, in theory, completely shields an interior object of arbitrary size from electromagnetic fields without disturbing the external fields [69].

The design of such a cloak requires the use of an optical transformation. Optical transformations allow scientists and engineers to control the path of the electromagnetic waves in an unprecedented manner. Moreover, the optical space can be curved by creating complicated spatial distributions of the electric permittivity (ε) and magnetic permeability (μ) [70].

The concept of electromagnetic cloaking devices is inspired by ideas of optical transformation. However, cloaking is only one topic within the broad context of optical transformation. A hypothetical space with desired topological properties can be designed using the optical transformation technique, a situation that looks quite similar to the curved time-space in the general relativity [71, 72]. Another application of transformation optics is negative refraction, where electromagnetic waves follow coordinates that run backward in space [73] or time [74].

The development of optical transformation techniques are based on the early fundamental results developed in 1961 by Dolin and Post [71, 75]. Dolin successfully realised that Maxwell's equations are form invariant under a space-deforming transformation. In his work, he considered that an incident plane wave can pass through a spherical inhomogeneity with a specific set of anisotropic permeability and permittivity tensors without distortions, which is the idea behind today's transformation based

electromagnetic cloak. These important early studies were almost forgotten, until recently when the field of optical transformation has been reconsidered.

With this form-invariance of Maxwell's equations, under coordinate transformations, a functional device can be designed on the basis of an objective-oriented technique as of the following procedure:

Apply a form-invariant transformation to Maxwell's equations to distort real space, in accordance to the required functionality. Then the permittivity and permeability tensors are determined from the coordinate transformations to achieve the real space distortion. This then specifies an inhomogeneous and anisotropic medium. Finally, the required material properties are designed to eventually realise the device. This normally requires a metamaterial solution. Metamaterials are man-made structures that are potentially very versatile, but they are not naturally occurring materials and are hard to synthesize using conventional technologies. This is the major reason that the optical transformation approach was not fully appreciated and has only gained popularity because of the recent research on metamaterials.

To visualise the optical transformation idea, take an electromagnetic cloaking device with the coordinate transformation demonstrated in Figure (5.1). The curved transformation coordinates of physical space (Figure 5.1 B) are transformed from the straight Cartesian coordinates in a virtual space (Figure 5.1 A). The electromagnetic waves follow straight lines in the "empty" space that appear curved in physical space. In other words, the coordinate transformation expands a single point in the electromagnetic space to an extended volume in physical space; anything "inside this point" is invisible.

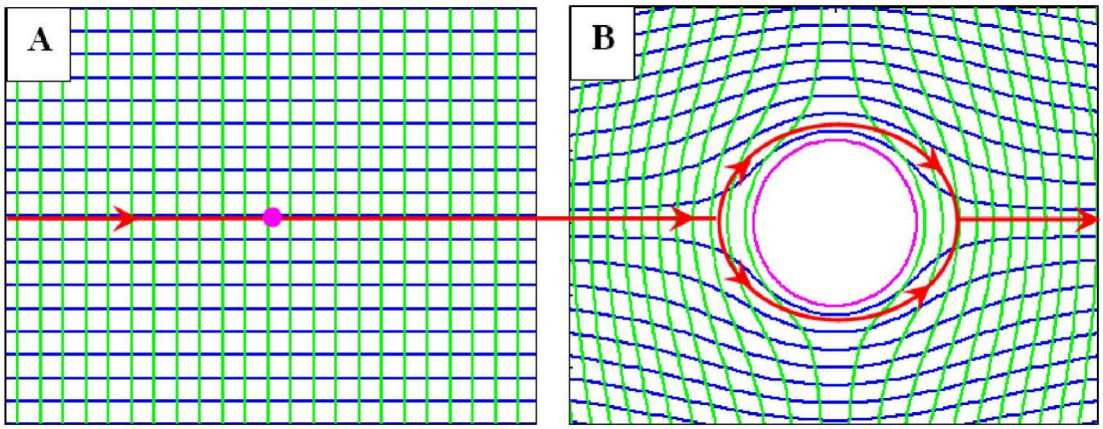

Figure (5.1): Cloaking device, (A) Virtual space, (B) physical space [69, 73].

In virtual space, the electromagnetic wave passes a point in very short time, but the point has become an extended region in physical space. Thus, electromagnetic wave must propagate faster along this extended region [73]. This is possible only at certain frequencies that correspond to resonances of the metamaterial's unit cell. Other electromagnetic wave frequencies would not be cloaked but instead be distorted. The considered space is represented by a Cartesian coordinate system with this method; a hole is created in the fabric of space (mathematically) by distorting the coordinate system. The pink circle (Figure 5.1 B) represents the invisible cloaked region. This is because the space that the electromagnetic wave travels in has been deformed, and therefore no light can be scattered from it. The properties of the transform are subsumed into a new form of spatially dependent permittivity and permeability in order to retain the invariance of Maxwell's equations. The cloaking effect in this case is the same as creating the hole in space.

5.2 Optical Conformal Mapping

The optical conformal mapping method is an alternative approach to the optical transformation concept used to design a medium that realises a perfect invisibility cloak in the ray-tracing limit [72, 76].

In dielectric media, electromagnetic waves will take the shortest optical path according to Fermat's principle [77]. This path-length is defined by the refractive index of that media. The shortest optical paths are not always straight lines, but are curved when the refractive index is spatially varying. Many optical illusions are caused by such bending of the light rays.

A cloak could be manufactured with the situation where a light is guided around a hole in medium so all the parallel incident rays are bent around the hole and recombined in precisely the same direction as they entered the medium. The difference between light passing through the medium and propagating across empty space is not distinguishable. Thus any object placed in this hole would be hidden from an observer and the medium would create the ultimate optical illusion of invisibility [18].

5.3 Optical Transformation Medium

A transformation medium is the medium that performs an active coordinate transformation. In such a medium, electromagnetism in physical space, including the effect of the medium itself, is equivalent to electromagnetism in transformed coordinates where space appears to be empty. This means transformation media maps electromagnetic fields in physical space to the electromagnetism of flat empty space [69, 73].

Example applications employing this medium includes; macroscopic invisibility devices [18, 69, 72] and perfect lenses [7] are another demonstration of transformation media.

Transformation media shows some critical but interesting characteristics. To start with, the defined optical path is the same in both the virtual space and the transformation media.

Secondly, the transformation media has zero reflection given that the outer boundary is preserved before and after a coordinate transformation. In this context, when satisfying the topological condition, the electromagnetic media can also be reflectionless. This means that transformation-optical elements finite embedded coordinate transformation can be reflectionless if the axes of the transformation-optical medium in the direction normal and parallel to the interface between the transformation-optical medium and the surrounding medium are continuous at the boundary.

5.4 Invisibility Devices

Transformation optics appears to offer the potential of "Invisibility" that had been a long-lasting dream of scientists, writers, artists, movie makers, and many more. This aspiration may date back to the emergence of early human civilization. Certainly achieving invisibility would open the door to a world of applications limited only by our imaginations.

The concept of being invisible or undetectable, however, has belonged to the realm of legends, folklore, science fiction and mythological tales rather than to our real world. A famous Greek mythology is a good example of the invisibility fantasy, when the son of Zeus Danaë (Perseus) beheaded one of the Gorgons (Medusa) when equipped with a helmet of invisibility (Figure 5.2) [78].

Similarly, nowadays the trance of invisibility occurring in modern art works such as movies, and TV series. The "invisible man" in Wells (2002) used a chemical drink to turn the refractive index of his body identical to that of air thus making him transparent. This is one of the fictional works sources of many popular and similar subsequent stories including the well-known series of seven fantasy novels and eight-part film series Harry Potter and popular book series and movie trilogy The Lord of the Rings.

Despite the fact that these heroic tales have held the attention of people for generations they have nothing to do with real life. Actuality, nature is comprised a number of phenomenon that approach invisibility to some extent.

Figure (5.2): Perseus with Medusa's head - Sculpture by Antonio Canova, Museo Pio-Clementino, Roma [78].

© 2009 Marie-Lan Nguyen / Wikimedia Commons

Accessed on 14th December 2014 at http://commons.wikimedia.org/wiki/File:Perseus_Canova_Pio-Clementino_Inv969.jpg

Scientifically, only few attempts have been made to achieve invisibility. The desired phenomena of being effectively invisible may be grouped in to three principal methods: camouflage, transparency and cloaking:

5.4.1 Camouflage

Camouflage can be defined as a visible object becoming undetectable in its surrounding medium due to similarity or likeness in colours or patterns or both. Many animals and plants protect themselves from predators using camouflage by mimicking the colours of their surroundings. Other animals, for example jellyfish, are naturally transparent.

Camouflage can also be achieved with active approach (active camouflage). This is a more straightforward method that is accomplished by taking real-time video of a scene

then projecting this video on to a screen that is blocking the scene itself. For example, the screen can be a coat worn by a person that displays a real time scene taken from behind that person. Effectively, giving the illusion of transparency to an observer standing in front of the screen (the coat in this case) [79]. In this example, the coat fabric is made of 50 microns wide mirrors that act as a screen. This virtual reality approach has been reported by Japanese scientist invents 'invisibility coat' (Figure 5.3).The team led by Susumu Tachi, from Keio University, is now adapting their findings to help pilots, drivers, doctors and others using this technique.

Figure (5.3): Reflective projection technology (RTP).

5.4.2 Stealth

Another method of being undetectable is to prevent detectors (like radar in this case) from getting information about an object. This is usually achieved by reducing the cross-section of the object against particular sources. This can be done, for example, using specific absorptive surfaces along with special shapes and materials that hinder the radar

signal whose wavelength is typically 2 cm. This is the idea behind stealth techniques also known as low observable technology [80].

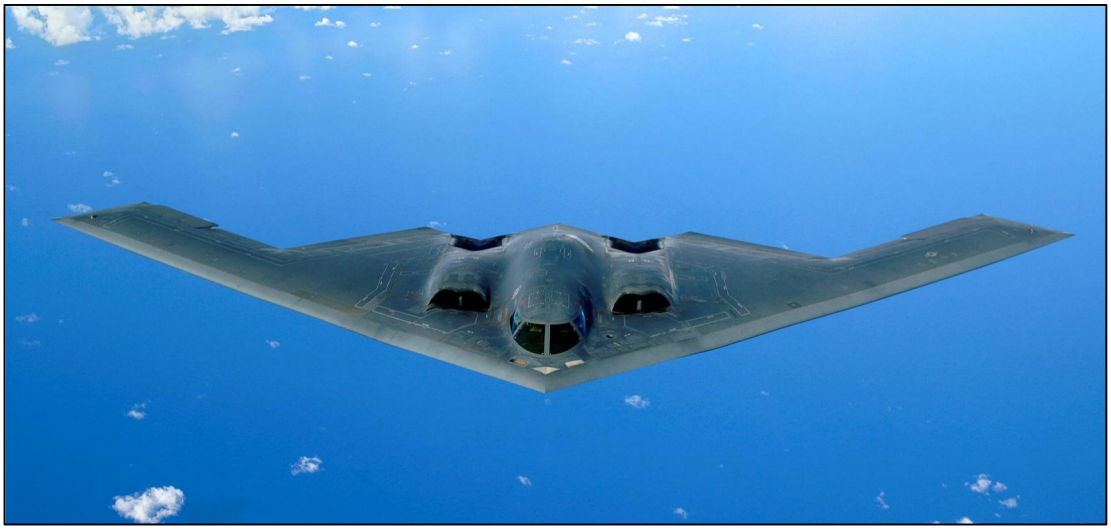

Figure (5.4): Air Force B-2 Spirit "Stealth" bomber [82].

The stealth technique has been adopted in many military applications like The Northrop Grumman B-2 Spirit. The aircraft, also known as the Stealth Bomber, is designed to penetrate dense anti-aircraft defences without being detected (Figure 5.4).

Stealth techniques mainly depend on reducing reflection from broad band frequencies including the microwave, infrared and radio-frequency spectrum. The first attempt to use stealth technique started in Germany during the Second World War. The Horten Ho 229 was the first stealth aircraft designed in Germany. The design was based on special graphite paint that absorbed radar signals together with the unique flying wing shape that gives the inspiration later to design the B-2 stealth bomber (Figure 5.4) [81]. This was followed by many well-known U.S aircraft include the F-117, F-22 and the B-2 Spirit.

However, the stealth aircraft is not completely invisible to some radars but difficult for conventional radar to detect or track these aircrafts.

5.4.3 Invisibility cloak

The final version of invisibility is to give an object the same scattering properties as those of a vacuum by making this object reflect no light and absorb no energy. This can be achieved by creating complicated spatial distributions of the electric permittivity and magnetic permeability [69-72]. The rapid development of the optical transformation theory has led to the design of new materials that can steer light along arbitrary curves. The implementation is made possible by metamaterials [69-72].

Among various novel applications of metamaterials, the most interesting is a cloaking device designed to bend light around a shielded region, rendering any object inside the cloak "invisible". In electromagnetic language, rendering an object not identifiable means to significantly lower its scattering cross-section, ideally to zero, at which point the object does not scatter any of the incident waves.

In the early stages of cloak fabrication, efforts were focused on spherical and circularly cylindrical cloaks, which were perceived to be posing very little difficulty to design, analyse and perform simulations on them. In theory, these cloaks can render any stationary object invisible within the cloak shell. However, practically, spherical and circularly cylindrical cloaks are not convenient for concealing thin and long objects. Therefore, elliptical–cylindrical cloak design was considered to overcome the above difficulty and open the route for wide range of applications.

The elliptical-cylindrical cloaks have two advantages over circular–cylindrical cloaks discussed in [83]. First, it is possible to conceal larger ranges of shape. Second, they have fewer singularities in the cloaking region making them easier to fabricate. In comparing an elliptical–cylindrical coordinate system with the coordinate transformation of an

elliptical cloak, the cloaking region can be reduced to a zero-width line instead of a point, thus singular values in material parameters can be avoided [83].

The inner boundary of the cloak often requires singular parameters values to realise a perfect cloak. This makes it difficult to facilitate in practical realisations even when filling the cloak with metamaterial [18]. To overcome the imperfections of a reduced-parameter cloak, the concept of a carpet cloak needs to be considered, as singular value requirements for the material parameters become less severe [84]. Experimentally, a broadband low-loss metamaterial was employed to fabricate the carpet cloak at microwave frequencies [85].

The above discussion focussed on electromagnetic invisibility cloaks that employ metamaterials as the transformation medium. However, it is also possible to achieve and approximate other types of designs that apply transformation functions or even nonmagnetic cloaks [86]. In this context, other shape parameters might be very important in certain applications. In all previously mentioned cloaks, the boundaries of the inner and outer metamaterial shell have similar shape. However, in real applications, the outer boundary shape would depend on the external environment. Meantime the object of application may take an arbitrary shape, thus, preferably, the inner shell of the metamaterial may have the same shape as the object. This means that it is not always true that the exterior and interior boundaries are of similar shapes. Optical transformation techniques can design cloaks with different outer and inner boundaries.

5.4.4 Other Invisibility Devices

5.4.4.1 Invisibility tunnel

An invisibility tunnel is one of the more interesting invisibility devices proposed and analysed in [87]. In this design a mathematical description was presented, in which the invisible tunnel conceals the electromagnetic waves that propagate inside the tunnel making these waves invisible to the observers.

All the invisibility cloaks discussed in this section have a continuous boundary region in which the electromagnetic wave is guided smoothly around the cloak and excluded from the cloaked region without, or with very little, distortions. These types of cloaks can be denoted as closed cloaks.

One obvious advantage of open cloaks over the closed ones is that they have at least one open window through which both information and matter can be transmitted, an issue that makes closed cloaks impractical for moving objects. Many types of open cloaks were proposed in [88]. These types of cloaks have one or more open windows, hence a concealed object can be exchanged with another one, and this means information and matter with the outer environment can be exchanged [88].

5.4.4.2 Remote Cloaks

A new approach for an invisibility cloak has been proposed in [89]. This type of cloak can conceal an object that lies outside the cloak exterior boundary. This design is based on the concept of special type of transformation media called complementary media. At a given wavelength, this transformation can cancel a certain volume of space and replace it with the required image.

The working principle of such cloak can be summarised as follows: the object and the closely surrounding virtual space is optically cancelled by using a complementary media layer with an enclosed image of the object. This complementary media is realised with

metamaterials that have negative index of refraction. Then, the required optical path in the cancelled space is restored by a dielectric core material (Figure 5.5). This means that the cancelled space is replaced with the whole invisibility system that must fit exactly in the empty space void [90].

This type of cloaks would open new routes to many potential applications, mainly of military interest and imaging components such as the super-lens. A remote cloak is a transformation device, however it operates like camouflage system by changing the actual appearance of the object.

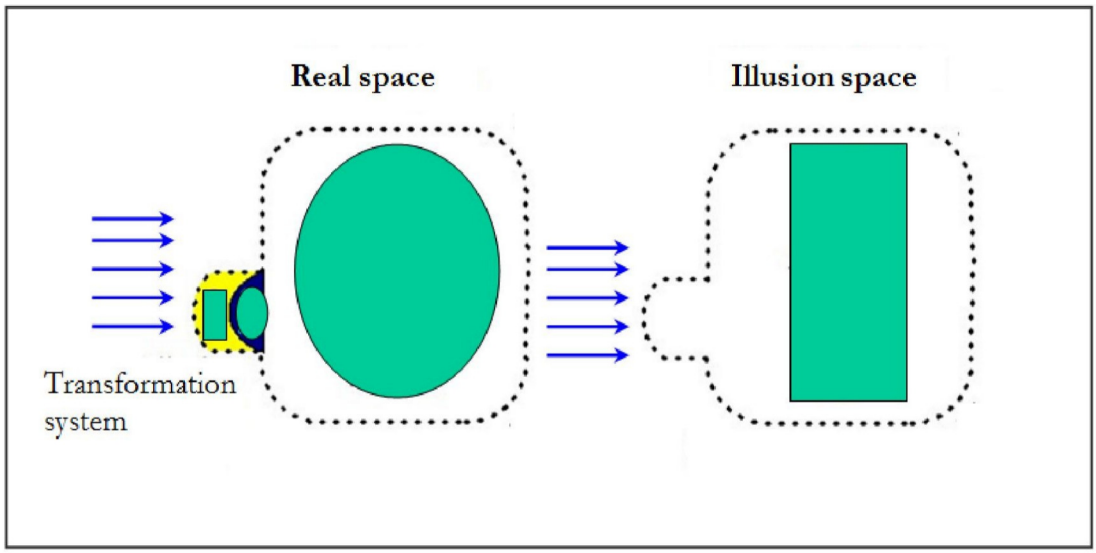

Figure (5.5): working principle of Remote Cloak that transforms the object (oval) into that of the illusion (rectangle). The dashed curves represent the shared boundary for both real and virtual space.

In a similar, but not the same story, BAE Systems use different technique to achieve similar result using an adaptive thermal signature management developed in Sweden. The system consists of special panels fitted on the CV90 light tank that can be detected as different images, disguised as smaller or different vehicles (Figure 5.6) [91].

Figure (5.6): CV90 tank viewed with IR camera

Scientists at BAE Systems believe that this system can be used against infrared sensor systems, night vision goggles and heat seeking missiles. The tank is visible to naked eye however when looked at with IR camera, the picture changes completely when the tiles or large pixels on the tank rapidly change the temperature to make the vehicle disappear in the IR part of the spectrum. Also the tank is fitted with an outside camera that analyses and sends to the outer panels a signal to mimic the surrounding region and to pretend it is something harmless like a small car (Figure 5.6).

5.4.4.3 Transparent wall

Based on the same transformation principle as mentioned before, the cloaking device works at a distance from the object, it is possible to transform part of an object (wall) into a virtual space, thus rendering that part invisible while leaving the rest of the wall visible [87]. This means an observer can see through the wall and obtain information from the other side.

5.4.4.4 Carpet cloak

The carpet-type cloak was introduced by Li and Pendry [84]. With this type of cloaking case, the optical transformation is designed to convert a curved surface into a flat one and to eliminate the distortion of EM waves from that surface. In contrast, the previously discussed cylindrical or elliptical cloaks are cloaked regions compressed into a non-scattering point or line.

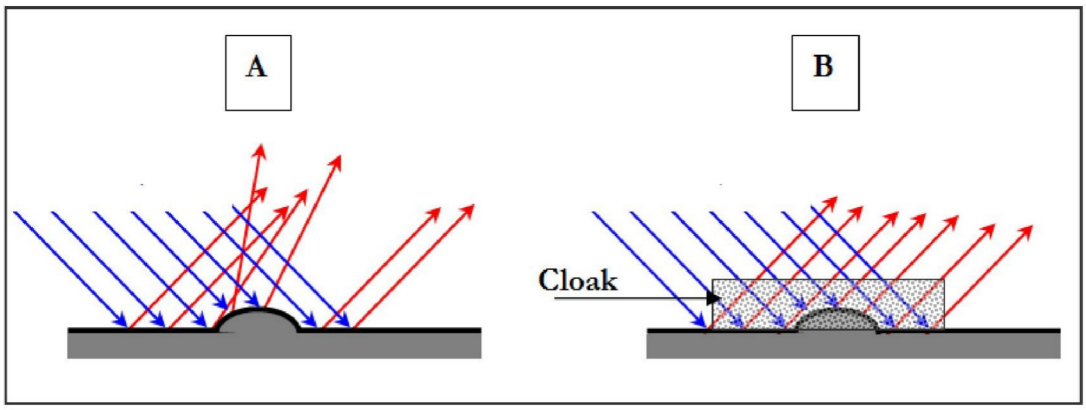

Figure (5.7): Schematic of the invisibility carpet. (A) Light scattered from a curved reflecting surface. (B) Light scattered from the same surface but shielded by an invisibility carpet. The blue and red rays represent the incident and reflected rays respectively.

This transformation cloak is schematically illustrated in Figure 5.7 above. The carpet cloak is depicted by the transparent rectangular shape. The cloaking device designed to hides the curved carpet along with any object hiding under it by making it appear as a flat reflecting surface.

5.5 Cloak Fabrication and Experimental Demonstrations

The previous sections described some fascinating cloaking options, but many leave one obvious question: how can we actually construct the electromagnetic cloaks of this research interest. From an application point of view, the construction of these

electromagnetic cloaks suggests that the required metamaterial structures must fulfil the set of parameters corresponding to these types of cloak. Taking the cylindrical cloak model investigated in reference 10 and replicating it will give a better understanding to the feasibility and repeatability of this type of cloak using laser micromachining. More importantly, it will prepare the way to the next stage of this research by employing the reduced SRR size discussed in chapter two to achieve cloaking at higher frequencies.

Research on electromagnetic metamaterials has provided novel control over the material properties; however, it is still quite challenging to exactly satisfy the material parameters based on the coordinate transformation.

The following sections (5.5.1-5.5.4) describe a construction of a replica of Schurig's microwave cloak using laser processing and with a slight difference on the base design for practicality and ease of handling. The original reported base has 6 struts to hold the SRRs strips, this was found to be fragile and not practical for the method of testing a metallic object cloaking. The proposed design has a rigid base and struts built on top.

This will be followed by testing with a microwave network analyser and results (section 5.54). The material parameters for the proposed geometry of this cylindrical cloak can be derived from the transformation explained in reference [18] and the following.

For the cloak design below, Figure 5.8, the coordinate transformation compresses a cylindrical region of $0 < r < b$ in the original coordinate system (r, θ, z) into a concentric cylindrical shell of $a < r' < b$ in the new coordinate system $(r`, \theta`, z`)$, where θ and z are the angular and vertical coordinates in the original system and θ' and z' are the angular and vertical coordinates in the transformed system. Note that z is normal to x,-y plane pointing out of the page in figure 5.8 below.

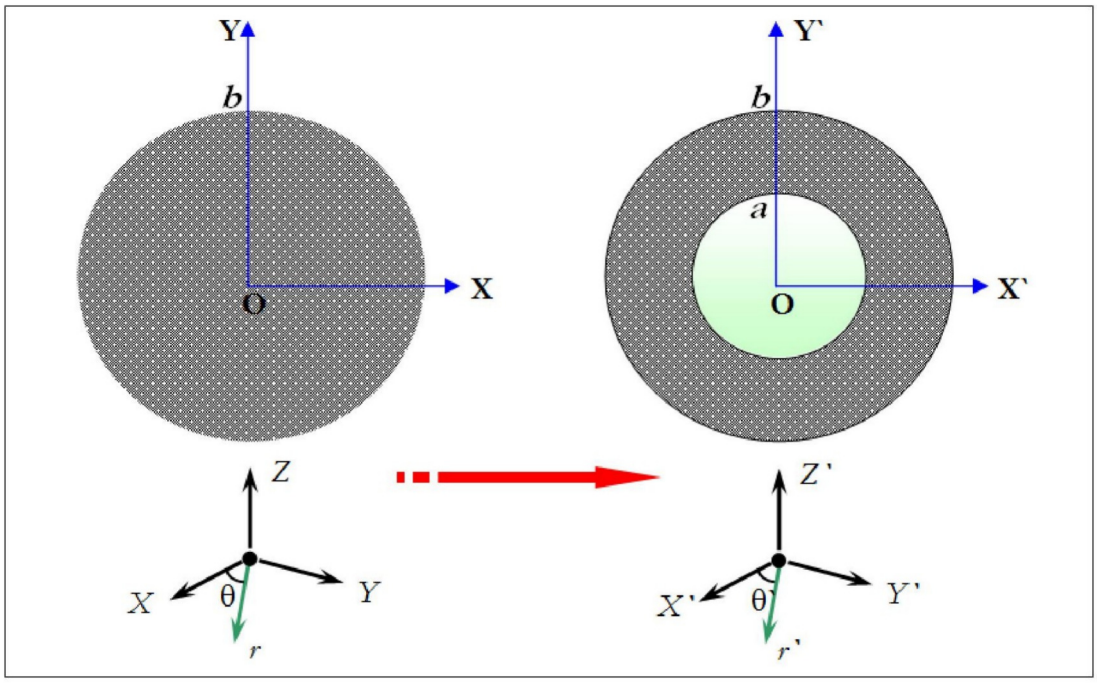

Figure (5.8): The cross section of a cylindrical cloak, the grey region is the cloaking layer and the green area is the concealed region.

In the standard incident polarizations (TE and TM) case, the requirement can be relaxed such that the TE polarization, or the electric field, is polarized parallel to the cloak cylinder axis.

Following the simplification described in [18] the constitutive material parameters for TE incident wave polarization [18] are:

$$\mu_r = \left(\frac{r-a}{r}\right)^2 ; \mu_\theta = 1 ; \varepsilon_z = \left(\frac{b}{b-a}\right)^2 \text{----------} (5.1)$$

These parameters are simplified to form reduced parameters that are more realistic for practical applications with a non-zero reflectance drawback. A detailed proof of the last equation is explained in Ref. [18] and the supporting materials therein.

Now that we have the simplified metamaterial parameters, the next step is to construct a concentric cylindrical base that will hold the metamaterial. This is followed by fabricating the metamaterial with specific dimensions and unit cells size (SRRs).

5.5.1 Frame design and prototype

The first part of the cloak is the frame that holds the SRRs strips, which were designed with Solidworks® software (Figure 5.9).

Using this software, 3D shapes can be designed and the project can be saved in stereolithography file format (.STL).

The STL file is loaded to a Dimension Elite 3D Printer (Figure 5.10) to build the part layer-by-layer from the bottom up.

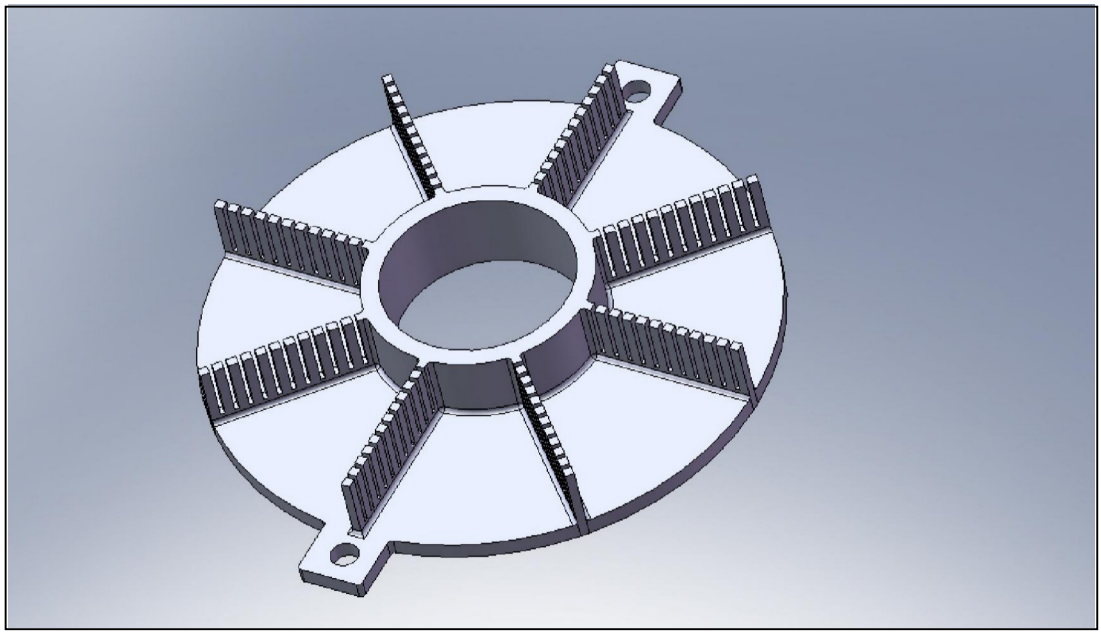

Figure (5.9): Screenshot of the cloak base from Solid Work software.

The working principle of this 3D printer is based on Fused Deposition Modelling (FDM) which is an additive manufacturing technology.

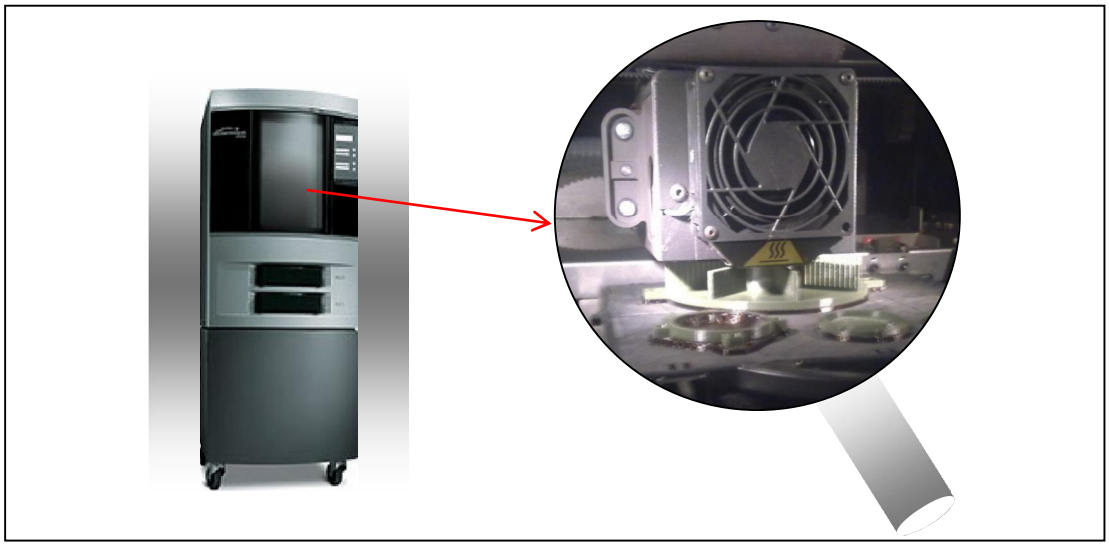

Figure (5.10): Dimension Elite 3D Printer during base fabrication process.

The working principle of this 3D printer is based on Fused Deposition Modelling (FDM) which is an additive manufacturing technology.

The printer deposits two materials; ABS plus thermoplastic for the part and the other for the support structure which is soluble material dissolves away in a water-based solution.

5.5.2 SRR Fabrication

The SRRs are fabricated upon flexible PCB material using a Quantronix Osprey pulsed (Q-switch) UV YAG laser (355nm) with average power 2W, pulse repetition frequency 20 KHz, beam diameter 0.75mm and pulse width 18ns. 85 µm flexible PCB was used in this experiment and consists of three layers: an insulating bottom layer, 35 µm middle copper layer and a polymeric photoresist layer on top.

The beam from the laser was taken via a 5x beam expander to a galvanometric scanning system (GSI Lightening Digital Scan Head).

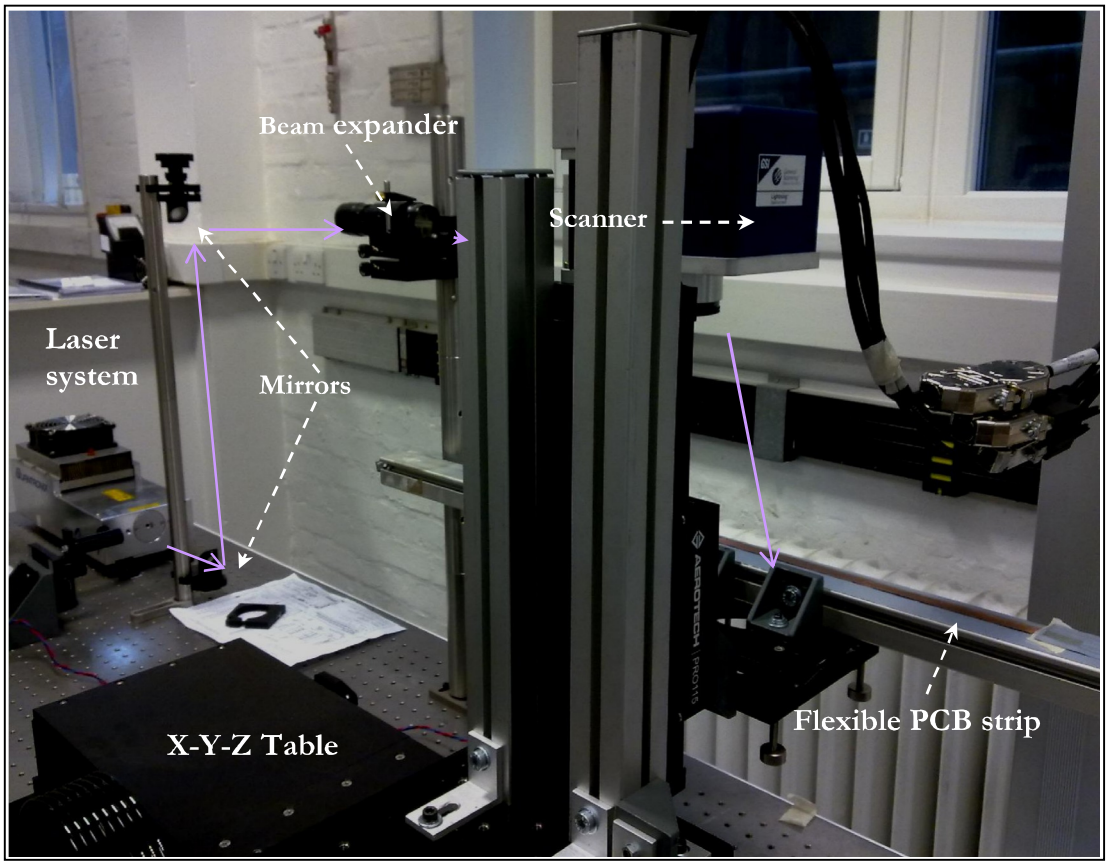

Figure (5.11): Quantronix Osprey UV laser system setup and clamping arrangement.

As illustrated in Figure 5.11, the beam is then focussed with Linos f-theta lens of 160 mm focal length to give a 10 μm spot size (see section 2.10.2 and calculation from equation 2.14).

The SRR unit cells were designed with AutoCAD software in DXF format that can be imported directly into the scanner software (SCAPS).

As discussed in chapter three the magnetic permeability μ_r can be controlled by varying the physical geometry of the SRRs. Thus the required gradient in permeability can be attained. Two geometrical parameters of SRRs are considered in this cloak model: the length of the split ***s*** and the curvature at the SRR corners ***r*** (Figure 5.12). The

permeability value can be plotted against the length of the split ***s*** and the curvature at the SRR corners ***r*** for each cylinder (figure 5.13).

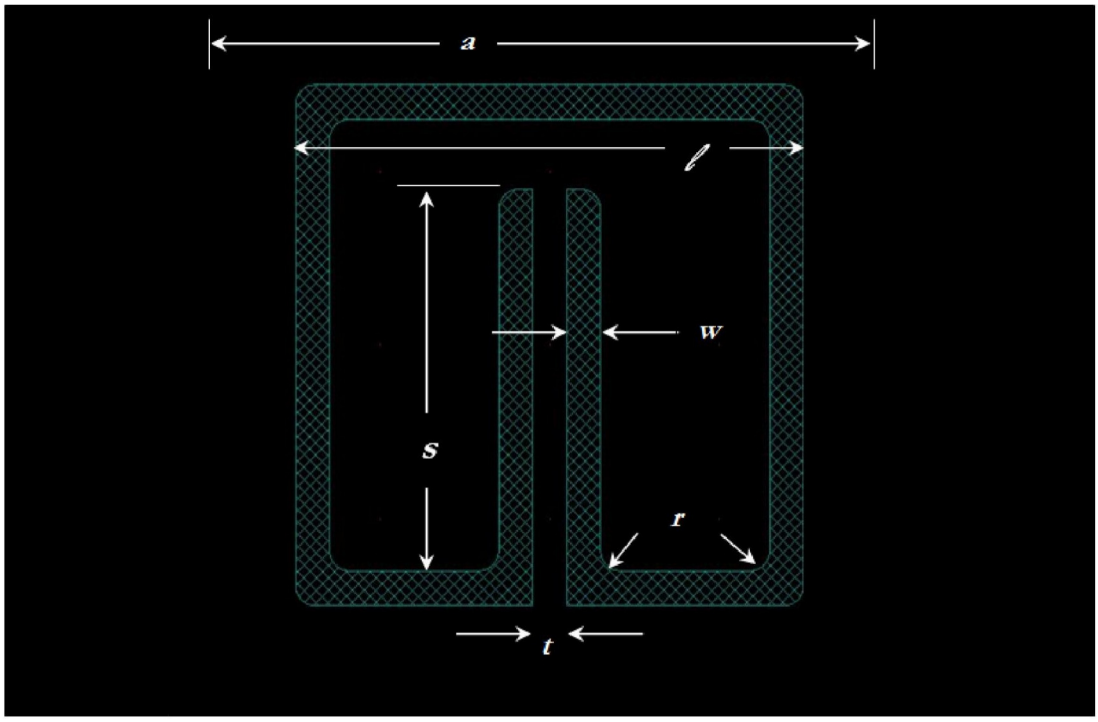

Figure (5.12): Single SRR unit cell designed with Autocad.

Such fine geometrical modifications enable tuning the value of μ_r from near zero at the inner layer to $(1-\frac{a}{b})^2$ at the outer surface of the concentric cylindrical cloak.

The expected operating frequency of this cloak is less than 8.5 GHz corresponding to 35 mm wavelength. Meanwhile the outer length of each SRR (ℓ in Figure 5.12) is 3 mm which is less than 1/10 of operating wavelength. Therefore the structure can be classified as a metamaterial device.

The SRRs unit cells are machined on flexible PCB strips which then can be bent into circles of varying diameter and slotted into the cloak frame (see next section). The fabrication of these structures was performed using the UV laser to ablate the polymeric

photoresist layer of the flexible PCB as described in chapter two for SRR micromachining.

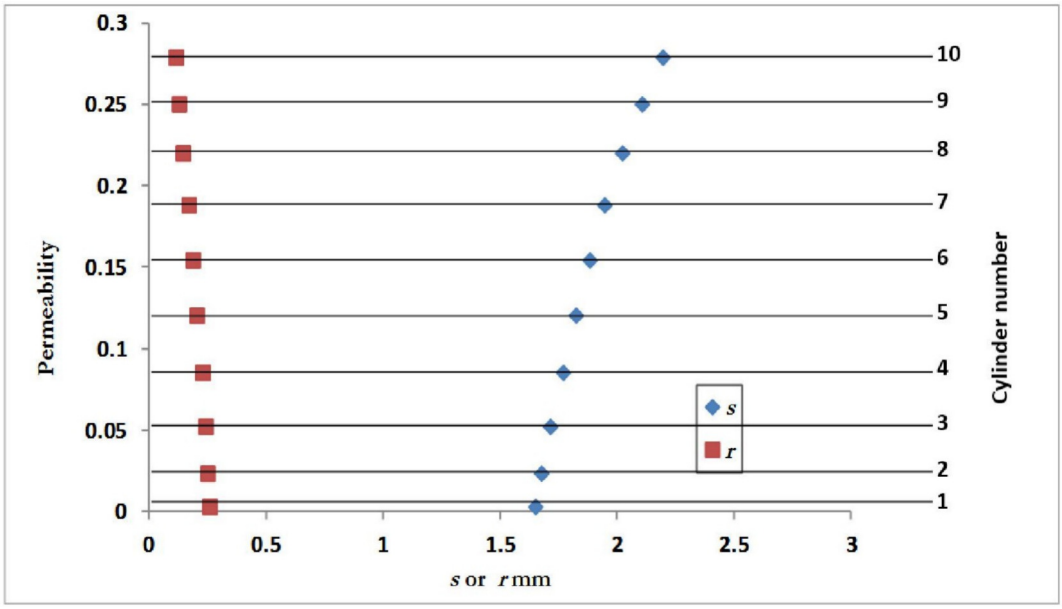

Figure (5.13): SRR fabricated on 10 strips with different split *s* and corners curvature *r* to form the cloak.

Each of the 10 SRRs strips is wide enough to contain three unit cells with each unit cell dimension 3.33 x 3.33 mm (***a*** in Figure 5.12) with SRRs dimension of 3x3 mm (Figure 5.14).

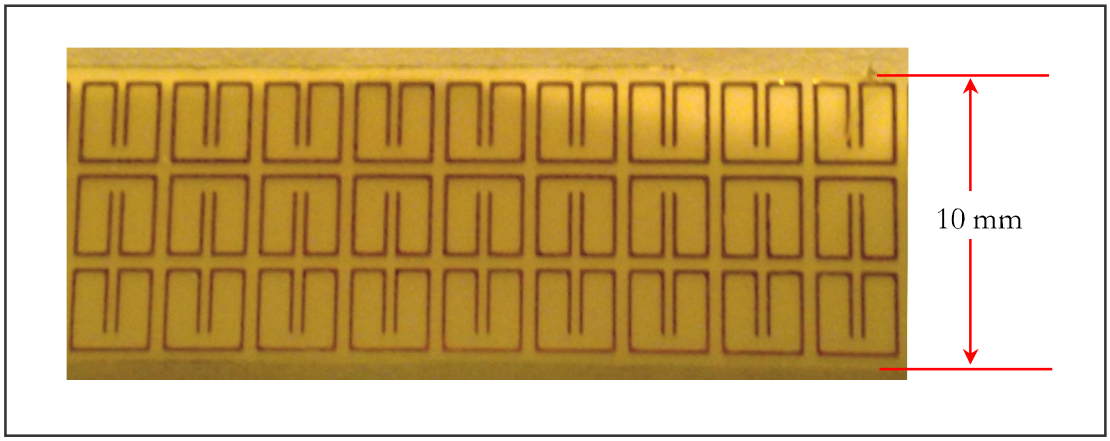

Figure (5.14): SRR machined on flexible PCB strip of 10 mm height.

A total of 10 cylindrical strips were processed in the same way (Figure 5.15) with length increasing by 20 mm and the SRR in each strip changed in shape but with same overall dimension. This unit cell design is based on Schurig's cloak [18].

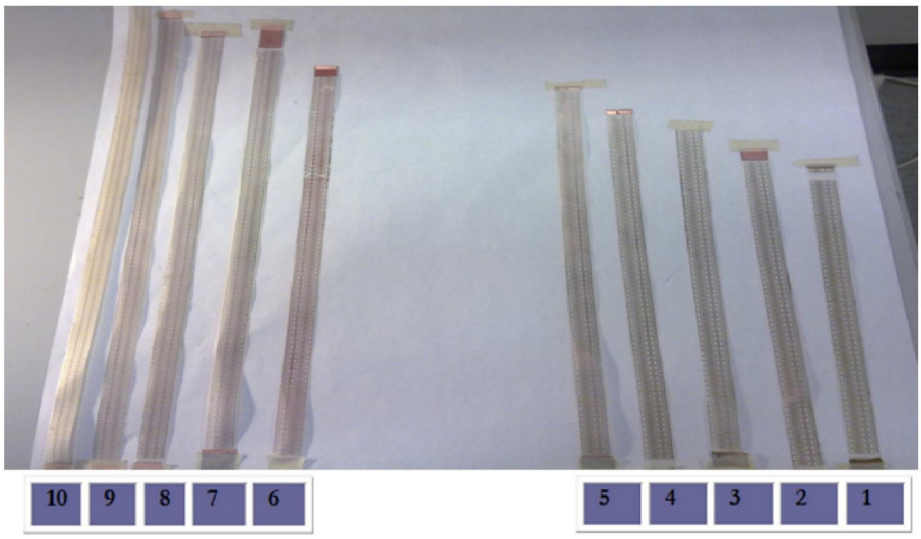

Figure (5.15): SRR fabricated on 10 strips with different length to form the cloak.

5.5.3 Cloak construction

The dielectric cylindrical base of this microwave cloak was made up of ten concentric cylinders filled with flexible PCB split-ring resonators, as shown in Figure 5.16.

Each PCB cylinder has an integral number of unit cells starting from 57 unit cells on the smallest cylinder and increasing by 6 unit cells on each subsequent cylinder.

The SRRs unit cells are placed in the θ-z plane (Figure 5.8) perpendicular to incident magnetic flux component along the radial direction.

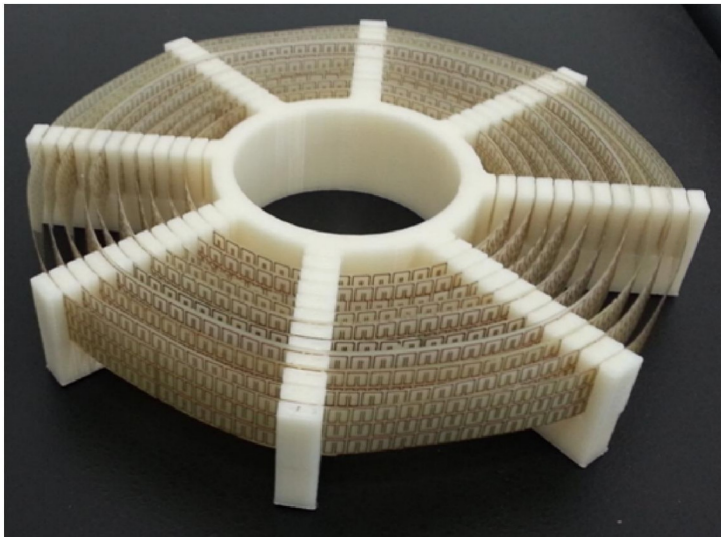

Figure (5.16): Final cloak shape fabricated in Photonics in Engineering (PiE) lab.

This will initiate magnetic resonance at the pre-designed frequency range of the cloak. The effective radial permeability value is determined by the geometry and density of the SRRs unit cells.

5.5.4 Cloaking demonstration experiment

The first ever experimental demonstration and validation of a cylindrical cloak was accomplished in 2006 by Shurig and others at Duke University achieving electromagnetic cloaking at microwave frequency range [18].

The following experiment evaluated the cylindrical cloak constructed in this project (Figure 5.16) and to understand the degree to which this cloak approaches the true cloaking property at the targeted microwave frequency. The cylindrical cloaking device is tested with an Anritsu 37397D Network Analyser, 10MHz-65GHz, and standard high gain microwave horn antennae as transmitter and receiver.

In this experiment, the scattering parameter (S21) was measured in four arrangement configurations. The frequency band considered in these set of experiments was from 6

GHz to 9 GHz. In the first case, the signal from transmitted horn is sent to the receiver horn with no devices placed in between, only a plastic support tube, thus offering minimum disturbance and so used as a calibration. In the second case, the transmission is measured through the cloak only to compare the differences in transmission with the other cases. A conducting stainless steel cylinder with 20 mm radius and 10 mm height is placed between the two horns in the third case. The transmission value is recorded in the same frequency range. Lastly, using the second configuration but now with the metal cylinder placed inside the cloaked region of the cloaking device and the scattering parameters measured again.

These configurations are illustrated in Figure (5.17) and the resulting VNA signals plotted in Figure (5.18) correspondingly. The calibration and the cloaking cases were compared against the case of a bare uncloaked metal cylinder.

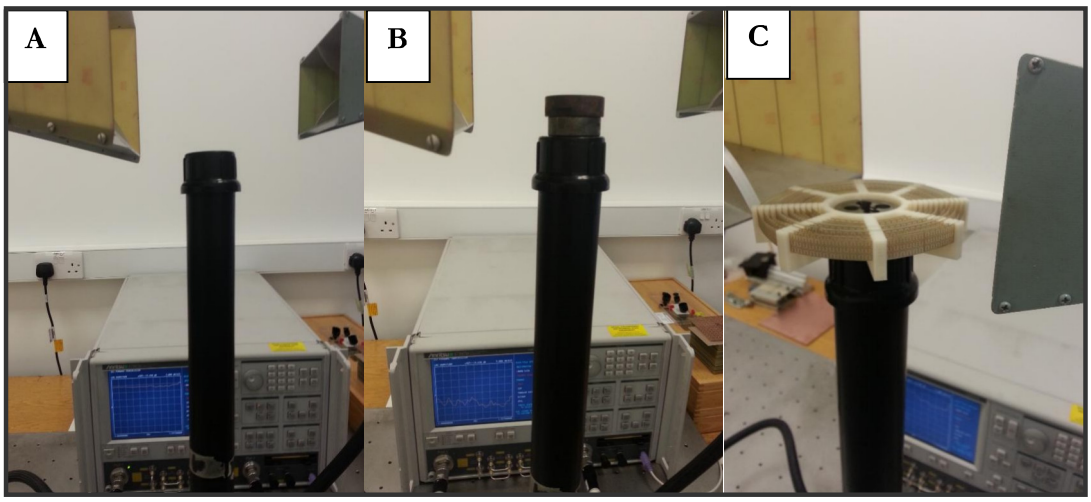

Figure (5.17): Three experimental layout for A: calibration, B: metallic object and C: cloaking device and the object.

The incident waves were dispersed with a bare metal cylinder case as seen in Figure 5.18, and the signal after the object is substantially distorted. This distortion in the signal corresponds to the shadow of the metallic object. The disturbance of the microwave

signal is reduced when the object is surrounded by the cloaking device and the transmission almost restored to the calibration case (Figure 5.18). As this cloak is designed to operate at below 8 GHz, the cloaking effect is expected to weaken. This can be seen on figure 5.18 where losses of around 5 dB appear at 8 GHz and above from reflections from the metal surface as the cloaking efficiency falls. As expected, at higher frequencies the wavelength is shorter and the unit cells are no more one tenth of the wavelength. At this point the LC resonance reduced down to the point where the frequency is too high and the resonance stop completely.

Although the result does not demonstrate perfect cloaking, it confirms the feasibility of creating a cylindrical cloaking device using Split Ring Resonator metamaterials with the transformation approach, and using laser processing to manufacture the SRR structures.

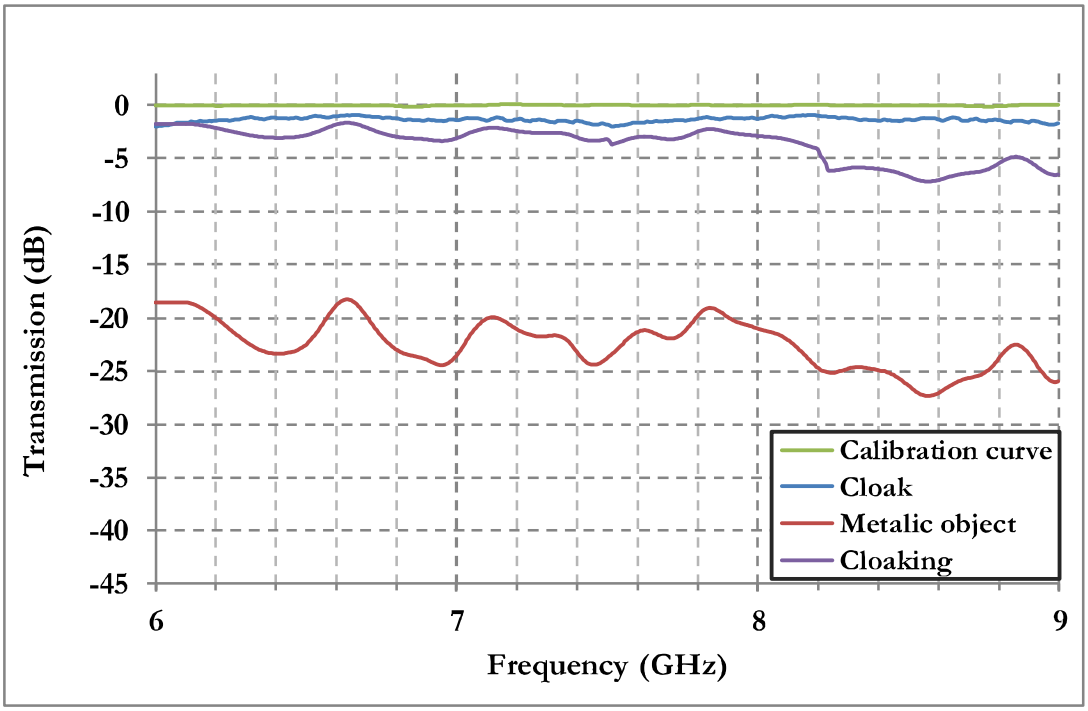

Figure (5.18): Transmission result from network analyser for four cases; A: calibration curve, B: cloak only, C metallic object and D: object surrounded by the cloaking device.

Also the device operates in both forward and backward transmission (S21 and S12) by significantly reducing the scattering of the incident waves, which is again evidence of the cloaking capability.

In addition, the device operates in both forward and backward transmission (S21 and S12) by significantly reducing the scattering of the incident waves, which is again evidence of the cloaking capability.

In this context, it verifies the bending and recovery of the microwave signal determined by the gradient in the permeability of the SRRs metamaterial.

Within the previous discussion of the realisation of a transformation-based electromagnetic cloak, the operating frequency bandwidth of the cloak is determined by the metamaterial properties that satisfy equation 5.1. Metamaterial parameters required by a given transformation can only be precisely satisfied only at a narrow frequency value [18].

The curved trajectory of the microwave within the cloak implies a refractive index less than 1 which must be dispersive to fulfil causation. This implies the phase velocity in the cloaking metamaterial is larger than the speed of light. Superluminal group velocity is forbidden under the special theory of relativity, except for the case of strong dispersion. Therefore, in this cloaking case, dispersion is necessary to avoid superluminal velocities, hence a substantial loss occurs.

5.6 Summary

The optical transformation theory and cloaking were presented at the beginning of this chapter with a brief introduction into optical transformations and conformal mapping

principles. In addition, other existing alternative to electromagnetic cloaking are discussed in "Transformation Devices". The fabrication and verification of a replica of Shurig's cloak fabrication has been presented. The cloak was fabricated from the constructed flexible PCB processed as explained in chapter two of this research. This is followed by experimental demonstrations to verify cloaking in the microwave frequency region. The cloaking verification is differing from the reference source by employing simple transmission technique tested with a vector network analyser rather than full field mapping. The feasibility and repeatability of this type of cloak using laser micromachining were proven.

Chapter Six

Conclusions and Future Work

6.1 Introduction

This final chapter summarises the main conclusions of the research conducted, highlighting both the novelty and results achieved with different strategies. In addition, the scope for future development of this research is presented in the last section of this chapter.

The research aim, to use laser processing in the fabrication of metamaterials active in the microwave frequency, has been validated through the research and resultant measurements.

The developed laser micromachining techniques, to process rigid and flexible PCBs, will be of interest to manufacturing of electronics industrial application.

6.2 Outcomes of research

A new technique to process rigid PCB with a pulsed IR fibre laser has been proven for directly micromachining rigid PCB without the need for any chemical etching, or masks, to create the required patterns. This technique is performed with high controllability and accuracy to ablate the copper cladding area leaving the required tracks. Tracks with 35 μm minimum width are shown to be possible. The benefit of this laser ablation method is that it can be employed in hard to reach areas on a PCB. The processing time is much less than conventional PCB processing technique.

The direct ablation method of micromachining rigid PCB offers advantages in the manufacturing low volume high density PCB's. More importantly it offers a method of machining tracks in populated PCB's. For instance, a process of late configuration of PCB's may be considered, where one common PCB design may carry several variant

circuits, which are selected, on demand, further down the production process, and even when the PCB is integrated in to the final product assembly. It may also be used to recover broken PCB's tracks by isolating damaged circuitry, enabling continued use of any remaining functions that can operate independently of the damaged section.

Another significant contribution of this research is a novel technique used in processing flexible PCB without the need of a photo-sensitive etch resist and also eliminating the use of masks. The technique can be used in processing the flexible PCBs (demonstrated in chapter 2 and Figure 2.23) and is unreported in the literature including patents. This technique is expected to offer a significant contribution to knowledge and industry as it can reduce the costs and save time by reducing the number of processing steps. A Q-switched DPSS UV laser was employed to directly write the designed pattern on to the top polymeric layer of flexible PCB. This is followed by chemical etching.

These new techniques were demonstrated in the application of manufacturing microwave metamaterials, these included solid PCB based materials and flexible PCB based material. All the metamaterial constructions investigated use a Split Ring Resonator (SRR) as the base unit cell of metamaterials. These were used to construct 2D and 3D left-handed media in this project. The design of these SRRs was a modified version of Pendry's model [1]. The enhancement of a single SRR was modelled with CST Microwave Studio® simulation software that can calculate the expected resonance frequencies of the SRRs. Laser based manufacture of samples were then fabricated and their microwave performance compared against the CST calculations.

One of the important outcomes of this research project is the possibility to manufacture a block of metamaterial, and machine a part of this 3D left-handed (LHM) metamaterial

and to demonstrate, for the first time, that its electromagnetic properties are almost preserved.

All the metamaterial designs encountered by looking in the literature are specifically designed and fabricated as structures. The Schurig cloak is a good example of this, with its rings of flexible PCB. Such designs are bespoke, and designed to achieve a particular outcome.

And so 3D LHM media are traditionally constructed as a fabrication of spaced 2D, or cylindrical, layers that are assembled to form a 3D LHM. In this research project the gap between these layers was filled with a dielectric material to make a rigid cube, creating a solid metamaterial block of well-defined metamaterial electromagnetic properties. The question then is this a true material that can now be machined into a form that allows its metamaterial properties to be used, in the same manner that an anisotropic RF, microwave, or indeed even optical material is shaped to perform its function.

The solid block of LHM produced in this project was cut, into two wedges with an electric bandsaw. The resultant wedges were demonstrated to have electromagnetic properties similar to the original material cube. The wedges successfully refracted a microwave beam as would be expected with the negative refractive index. This demonstration shows the potential for an end user to buy a "lump" of metamaterial and cut it or shape it as required for their needs.

The negative index of refraction of the machined wedge shaped, and the original slab shaped metamaterials has been proven by measuring the refraction angles and employing Snell's law to calculate the refractive index.

To demonstrate the use of the new laser technique for flexible PCB, a replica of Pendry and Schurig's microwave cloak [18] has been constructed and tested using a vector network analyser and employing a simplified technique to prove feasibility and repeatability of this type of cloak.

The project has demonstrated the use of lasers as a "rapid prototyping" tool for the manufacture of microwave metamaterial fabrication, by the manufacture of layered and composite structures, and introduced novel composite structures by machining solid metamaterial blocks.

6.3 Future work

This research project is principally an experimental project on electromagnetic metamaterials. Its has demonstrated that laser processing offers a valuable tool that will both enable and stimulate further practical investigation into the field of microwave metamaterials.

Several lines of further research can be identified to follow from the outcomes of this project. These include the continued of laser processing techniques that address a further decrease in the length scale of metamaterial production, for managing shorter wavelength materials, and the further development of machineable solid metamaterials.

These investigations would be in addition to working alongside metamaterial researchers, who have far greater access to design and measurement ability, to produce realistic models of their designs for testing.

It would be readily possible to manufacture metamaterial structures for longer wavelengths with laser processing. This research has demonstrated a track resolution below 35μm. It will be important to push this down further, to enable the laser

manufacture of smaller features. Recall that the size of the unit cell should be less than 0.1 of the wavelength, so to reduce the wavelength of metamaterials it must require the reduction in feature size of the laser machined material.

Such reductions might be achieved by further work on the use of shorter wavelength lasers e.g. Excimer and shorter wavelength DPSS lasers. Equally it might be possible to use ultrashort pulse lasers and use multiphoton absorption techniques to further reduce feature size.

This project has demonstrated the machining of metamaterial over areas that exceed the size of operation of a typical laser galvanometer scanning head. The manufacturing of large areas of repetitive shapes is another necessary area of research. This may involve higher power Excimer and DPSS lasers for "patterning" as employed in display screen manufacture.

An issue to consider in large scale patterning is the ability to change the pattern as the area is covered. The manufacture of the Schurig cloak illustrates how small but important changes must be made to geometry. How might this be done with efficiency? Could optical techniques such as spatial light modulators be employed?

This thesis reports on the manufacture of a solid metamaterial block that has been machined and used to demonstrate the negative refraction in a wedge shaped component machined from solid block.

The possibility for further research is to machine more complicated parts from the 3D left-handed (LHM) metamaterial and investigate their electromagnetic properties. For example, a curved shape can be machined out of the LHM cube and its possibility to create a "super-lens", a predicted capability of metamaterials, may be investigated.

More in-depth discovery of the properties of the 3D LHM metamaterial and their applications fall more within the microwave engineering study. An example would be to integrate these LHM in microwave antenna designs for mobile phone technology, or for microwave sensing technology.

Such developments would require collaboration with more experienced microwave engineering group, with the laser technology to allow fabrication of designed microwave antennae.

Initially further investigation on individual SRR's, which is easier and quicker than assembled metamaterials, should be undertaken to measure their resonance frequency which is a very important factor for a given SRR geometry and size. From this, new LHM design can be explored with double sided PCB with SRRs on one side and thin wires on the other instead of using two single sided PCBs for this propose.

As well as the design element of microwave metamaterial that would require collaboration with experienced microwave designers, the investigation of laser manufactured structures would need improved access to diagnostic techniques.

An example of such a technique for the microwave cloak characterisation, some necessary equipment will be needed to achieve this. To obtain field maps, a planar waveguide chamber consisting of upper and lower aluminium plates need to be assembled. Aluminium frame can be designed to hold the upper plate whereas the lower plate is attached to X-Y linear stages. The metamaterial sample and the microwave source will be fixed to the lower plate. The upper plate will hold a coaxial antenna which connected to the network analyser.

The microwave radiation, by this method, can be confined and reduced to two X-Y dimensions so that the electromagnetic fields do not vary along the axis between the plates (z-axis). This will allow performing a map of the field just above the metamaterials sample as it would be difficult to insert a probe antenna inside the sample. LabView software can be used to make a program that coordinates the scan motion with the data acquisition of the network analyser.

6.4 Conclusion

This research project has successfully demonstrated the use of laser processing to enable the manufacture a range of metamaterials for the microwave wavelength. In doing so it has demonstrated new techniques for the laser processing of printed circuit boards, rigid and flexible.

It has also, for the first reported time, assisted the manufacture of a solid metamaterial block that has been cut to a wedge and exhibited negative refraction behaviour.

The project opens the possibility of further use of laser processing in the manufacture of metamaterials for the microwave wavelength, and identifies further laser process development to grow this application of laser.

Applications would include antennae, but also laboratory samples and cloaks for examination.

The manufacture of "solid" metamaterial is worth future work to optimise its performance and develop the machining of this material to manufacture metamaterial components.

References

1 Pendry, J. B., Holden, A. J., Robbins, D. J., & Stewart, W. J. (1999). *Magnetism from conductors and enhanced nonlinear phenomena.* Microwave Theory and Techniques, IEEE Transactions on, 47(11), 2075-2084.

2 G. Russakof, (1970). *A Derivation of Macroscopic Maxwell Equations.* Am. J. Phys. 38, 1188.

3 Veselago, V. G. (1968). *The electrodynamics of substances with simultaneously negative values of ϵ and μ.* Physics-Uspekhi, 10(4), 509-514.

4 Ready, J. F. (1997). *Industrial applications of lasers.* (Second Edition). Academic press. Ch3.

5 Smith, D. R., Padilla, W. J., Vier, D. C., Nemat-Nasser, S. C., & Schultz, S. (2000). *Composite medium with simultaneously negative permeability and permittivity.* Physical review letters, 84(18), 4184.

6 Kumar, A., & Kumar, M. (2014). *Gain Enhancement in Microstrip Patch Antennas Using Metallic Rings.* AJER 3(7), pp -117-124

7 Pendry, J. B. (2000). *Negative refraction makes a perfect lens.* Physical review letters, 85(18), 3966.

8 Leonhardt, U. (2007). *Optical metamaterials: Invisibility cup.* Nature Photonics, 1(4), 207-208.

9 Freestone, I., Meeks, N., Sax, M., & Higgitt, C. (2007). *The Lycurgus cup-a roman nanotechnology.* Gold Bulletin, 40(4), 270-277.

10 Schuster, A. (1904). *An introduction to the theory of optics.* E. Arnold.

11 Mandelshtam, L. I. (1947). *Complete Collected Works.* Akad. Moscow: Nauk SSSR.

12 Kock, W. E. (1948). *Metallic delay lenses.* Bell System Technical Journal, 27(1), 58-82.

13 Sivukhin, D. V. (1957). *The energy of electromagnetic waves in dispersive media.* Opt. Spektrosk, 3(308-31), 2.

14 Shalaev, V. M. (2007). *Optical negative-index metamaterials.* Nature photonics, 1(1), 41-48.

15 Zhou, J., Koschny, T., Zhang, L., Tuttle, G., & Soukoulis, C. M. (2006). *Experimental demonstration of negative index of refraction.* Applied Physics Letters, 88(22), 221103.

16 Toal, B., McMillen, M., Murphy, A., Hendren, W., Atkinson, R., & Pollard, R. (2014). *Tuneable magneto-optical metamaterials based on photonic resonances in nickel nanorod arrays.* Materials Research Express, 1(1), 015801.

17 Jain, A., Tassin, P., Koschny, T., & Soukoulis, C. M. (2014). *Large quality factor in sheet metamaterials made from dark dielectric meta-atoms.* Physical review letters, 112(11), 117403.

18 Schurig, D., Mock, J. J., Justice, B. J., Cummer, S. A., Pendry, J. B., Starr, A. F., & Smith, D. R. (2006). *Metamaterial electromagnetic cloak at microwave frequencies.* Science, 314(5801), 977-980.

19 Zhigilei, L. V., & Garrison, B. J. (2000). *Microscopic mechanisms of laser ablation of organic solids in the thermal and stress confinement irradiation regimes.* Journal of Applied Physics, 88(3), 1281-1298.

20 Schäfer, C., Urbassek, H. M., & Zhigilei, L. V. (2002). *Metal ablation by picosecond laser pulses: A hybrid simulation.* Physical review B, 66(11), 115404.

21 Steen, W. M. & Mazumder, J., (2010). *Laser material processing.* London: Springer.

22 Von ALLMEN, M., & Blatter, A. (1995). *Laser beam interactions with materials: physical principles and applications.* Springer series in materials science. Springer, Berlin.

23 Welch, A. J., & Martin J.C. van Gemert. (2011). *Optical-Thermal Response of Laser-Irradiated Tissue*. Second Edition. Springer Science+Business Media B.V..

24 Ready, J. F. (1997). *Industrial applications of lasers*. (Second Edition). Academic Press Ltd. Ch12, 315-334

25 Unpublished internal data: Powerlase Photonics Ltd., Crawley, UK

26 Dahotre, N. B., & Harimkar, S. (2008). *Laser fabrication and machining of materials*. (Vol. 51) Ch 3. New York: Springer.

27 http://www.powerlase-photonics.com/products/

28 Ready, J. F. (1997). *Industrial applications of lasers*. (Second Edition). Academic press. Ch2. 31-65

29 Schaaf, P. (2010). *Laser processing of materials*. Springer Series in Materials Science, 139, 243.Ch 8, 160-185.

30 Thompson, K. P., Ren, Q. S., & Parel, J. M. (1992). *Therapeutic and diagnostic application of lasers in ophthalmology*. Proceedings of the IEEE, 80(6), 838-860.

31 Ready, J. F. (2001). *LIA Handbook of Laser Materials Processing* (1st Ed). Ch5 167-204

32 Bado, P., Clark, W. & Said, A. (2011).*Ultrafast Laser Micromachining Handbook*, http://www.cmxr.com/Education/Introduction.html

33 Meijer, J., Du, K., Gillner, A., Hoffmann, D., Kovalenko, V. S., Masuzawa, T., & Schulz, W. (2002). *Laser machining by short and ultrashort pulses, state of the art and new opportunities in the age of the photons*. CIRP Annals-Manufacturing Technology, 51(2), 531-550.

34 Bäuerle, D. W. (2011). *Laser processing and chemistry* (4th Ed). Springer. Ch12

35 Bäuerle, D. W. (2011). *Laser processing and chemistry* (4th Ed). Springer. Ch2

36 Gower, M. C. (1993). *Excimer lasers: current and future applications in industry and medicine*. In Laser Processing in Manufacturing (pp. 189-271). Springer Netherlands.

37 Vogel, A., & Venugopalan, V. (2003). *Mechanisms of pulsed laser ablation of biological tissues*. Chemical reviews, 103(2), 577-644.

38 Furusawa, K., Takahashi, K., Kumagai, H., Midorikawa, K., & Obara, M. (1999). *Ablation characteristics of Au, Ag, and Cu metals using a femtosecond Ti: sapphire laser*. Applied Physics A, 69(1), S359-S366.

39 Rizvi, N. H., & Apte, P. (2002). *Developments in laser micro-machining techniques*. Journal of Materials Processing Technology, 127(2), 206-210.

40 Alwaidh, A., Sharp, M., & French, P. (2014). *Laser processing of rigid and flexible PCBs*. Optics and Lasers in Engineering, 58, 109-113.

41 Smith, H. I., Menon, R., Patel, A., Chao, D., Walsh, M., & Barbastathis, G. (2006). *Zone-plate-array lithography: a low-cost complement or competitor to scanning-electron-beam lithography*. Microelectronic engineering, 83(4), 956-961.

42 Deladurantaye, P., Gay, D., Cournoyer, A., Roy, V., Labranche, B., Levesque, M., & Taillon, Y. (2009). *Material micromachining using a pulsed fiber laser platform with fine temporal nanosecond pulse shaping capability*. In SPIE LASE: Lasers and Applications in Science and Engineering (pp. 71951S-71951S). International Society for Optics and Photonics.

43 Huske, M. (2006). *Burr and stress-free cutting of flexible printed circuits*. OnBoard Technology, 6, 18-21.

44 Varteresian, J. (2002). *Fabricating printed circuit boards*. Newnes. Ch5 69–83

45 Varteresian, J. (2002). *Fabricating printed circuit boards*. Newnes. Ch2 11–25

46 Chen, X., Grzegorczyk, T. M., Wu, B. I., Pacheco Jr, J., & Kong, J. A. (2004). *Robust method to retrieve the constitutive effective parameters of metamaterials*. Physical Review E, 70(1), 016608.

47 García-García, J., Martín, F., Baena, J. D., Marques, R., & Jelinek, L. (2005). *On the resonances and polarizabilities of split ring resonators*. Journal of Applied Physics, 98(3), 033103.

48 Gay-Balmaz, P., & Martin, O. J. (2002). *Electromagnetic resonances in individual and coupled split ring resonators*. Journal of applied physics, 92(5), 2929-2936.

49 Markoš, P., & Soukoulis, C. M. (2002). *Numerical studies of left handed materials and arrays of split ring resonators*. Physical Review E, 65(3), 036622.

50 Radkovskaya, A., Shamonin, M., Stevens, C. J., Faulkner, G., Edwards, D. J., Shamonina, E., & Solymar, L.(2005). *Resonant frequencies of a combination of split rings: Experimental, analytical and numerical study*. Microwave and optical technology letters, 46(5), 473-476.

51 Sauviac, B., Simovski, C. R., & Tretyakov, S. A. (2004). *Double split ring resonators: Analytical modelling and numerical simulations*. Electromagnetics 24,317-338.

52 Shamonin, M., Shamonina, E., Kalinin, V., & Solymar, L. (2004). *Properties of a metamaterial element: Analytical solutions and numerical simulations for a singly split double ring*. Journal of Applied Physics, 95(7), 3778-3784.

53 Zhou, J., Koschny, T., & Soukoulis, C. M. (2007). *Magnetic and electric excitations in split ring resonators*. Optics express, 15(26), 17881-17890.

54 Baena, J. D., Marques, R., Medina, F., & Martel, J. (2004). *Artificial magnetic metamaterial design by using spiral resonators*. Physical review B, 69(1), 014402.

55 Linden, S., Enkrich, C., Wegener, M., Zhou, J., Koschny, T., & Soukoulis, C. M. (2004). *Magnetic response of metamaterials at 100 terahertz*. Science, 306(5700), 1351-1353.

56 Katsarakis, N., Koschny, T., Kafesaki, M., Economou, E. N., & Soukoulis, C. M. (2004), "*Electric coupling to the magnetic resonance of split ring resonators*", Applied Physics Letters, Vol.84, No.15.

57 Shelby, R. A., Smith, D. R., Nemat-Nasser, S. C., & Schultz, S. (2001). *Microwave transmission through a two-dimensional, isotropic, left-handed metamaterial.* Applied Physics Letters, 78(4), 489-491.

58 Shelby, R. A., Smith, D. R., & Schultz, S. (2001). *Experimental verification of a negative index of refraction.* Science, 292(5514), 77-79.

59 Houck, A. A., Brock, J. B., & Chuang, I. L. (2003). *Experimental observations of a left-handed material that obeys Snell's law.* Physical Review Letters, 90(13), 137401.

60 Parazzoli, C. G., Greegor, R. B., Li, K., Koltenbah, B. E. C., & Tanielian, M. (2003). *Experimental verification and simulation of negative index of refraction using Snell's law.* Physical Review Letters, 90(10), 107401.

61 Dresselhaus, M. S. (2005). *Solid State Physics Part II-Optical Properties of Solids.* CH2 pp 8-15.

62 Ziolkowski, R. W., & Heyman, E. (2001*). Wave propagation in media having negative permittivity and permeability*. Physical review E, 64(5), 056625.

63 Enghetal, N., Erentok, A., & Ziolkowski, R. W. (2006). *Single-negative, double-negative, and low-index metamaterials and their electromagnetic applications.* Radio Science Bulletin, (319), 6-19.

64 Pendry, J. B., Holden, A. J., Stewart, W. J., & Youngs, I. (1996). *Extremely low frequency plasmons in metallic mesostructures.* Physical review letters, 76(25), 4773.

65 Ishikawa, A., & Tanaka, T. (2006). *Negative magnetic permeability of split ring resonators in the visible light region.* Optics communications, 258(2), 300-305.

66 K.A.Bakshi A.V.Bakshi U.A.Bakshi 2009 Antennas And Wave Propagation ch 6 pp1-20

67 Application note. (2011). *PCB Dielectric Material Selection and Fiber Weave Effect on High-Speed Channel Routing*, Altera Corporation, AN-528-1.1.

68 Data sheet, *photo resist copper clad board*, Farnell Electronic Components.

69. Pendry, J. B., Schurig, D., & Smith, D. R. (2006). *Controlling electromagnetic fields*. Science, 312(5781), 1780-1782.

70. Shalaev, V. M. (2008). *Transforming light*. Birck and NCN Publications, 101.

71. Dolin, L. S. (1961). *On a possibility of comparing three-dimensional electromagnetic systems with inhomogeneous filling*. Izv. Vyssh. Uchebn. Zaved. Radiofiz, 4, 964-967.

72. Leonhardt, U. (2006). *Optical conformal mapping*. Science, 312(5781), 1777-1780.

73. Leonhardt, U., & Philbin, T. G. (2006). *General relativity in electrical engineering*. New Journal of Physics, 8(10), 247.

74. Pendry, J. B. (2008). *Time reversal and negative refraction*. Science, 322(5898), 71-73.

75. Luo, Yuan, Baile Zhang, Tiancheng Han, Zhi Chen, Yubo Duan, Chia-Wei Chu, George Barbastathis, & Qiu, C. W. (2013). *Phase-preserved optical elevator*. Optics express, 21(6), 6650-6657.

76. Leonhardt, U. (2006). *Notes on conformal invisibility devices*. New Journal of Physics, 8(7), 118.

77. Born, M., & Wolf, E. (1999). *Principles of optics: electromagnetic theory of propagation, interference and diffraction of light*. Cambridge university press.

78. © 2009 Marie-Lan Nguyen / Wikimedia Commons, Accessed on 14th December 2014 at http://commons.wikimedia.org/wiki/File:Perseus_Canova_Pio-Clementino_Inv969.jpg

79. Tachi, S. (2003, May). *Telexistence and retro-reflective projection technology (RPT).* In Proceedings of the 5th Virtual Reality International Conference (VRIC2003) pp (Vol. 69, pp. 1-69).

80. Borden, B. (2002). *Mathematical problems in radar inverse scattering.* Inverse Problems, 18(1), R1

81. Zikidis, K., Skondras, A., & Tokas, C. (2014). *Low Observable Principles, Stealth Aircraft and Anti-Stealth Technologies.* Journal of Computations & Modelling, 4(1), 129-165.

82. © 2007 Staff Sgt. Bennie J. Davis III 1./Wikimedia Commons Accessed on 9th March 2015 at http://en.wikipedia.org/wiki/File:B-2_Spirit_original.jpg

83. Jiang, W. X., Cui, T. J., Yang, X. M., Cheng, Q., Liu, R., & Smith, D. R. (2008). *Invisibility cloak without singularity.* Applied Physics Letters, 93(19), 194102.

84. Li, J., & Pendry, J. B. (2008). *Hiding under the carpet: a new strategy for cloaking.* Physical Review Letters, 101(20), 203901.

85. Chen, H., Hou, B., Chen, S., Ao, X., Wen, W., & Chan, C. T. (2009). *Design and experimental realization of a broadband transformation media field rotator at microwave frequencies.* Physical review letters, 102(18), 183903.

86. Cai, W., Chettiar, U. K., Kildishev, A. V., Shalaev, V. M., & Milton, G. W. (2007). *Nonmagnetic cloak with minimized scattering.* Applied Physics Letters, 91(11), 111105.

87. Greenleaf, A., Kurylev, Y., Lassas, M., & Uhlmann, G. (2007). *Electromagnetic wormholes and virtual magnetic monopoles from metamaterials.* Physical Review Letters, 99(18), 183901.

88. Ma, H., Qu, S., Xu, Z., & Wang, J. (2009). *The open cloak.* Applied Physics Letters, 94(10), 103501.

89. Lai, Y., Chen, H., Zhang, Z. Q., & Chan, C. T. (2009). *Complementary media invisibility cloak that cloaks objects at a distance outside the cloaking shell.* Physical review letters, 102(9), 093901.

90. Zheng, G., Heng, X., & Yang, C. (2009). *A phase conjugate mirror inspired approach for building cloaking structures with left-handed materials.* New journal of physics, 11(3), 033010.

91. CV90 Brochure - BAE Systems